Efficient Three-Dimensional Global Models for Climate Studies: Models I and II

J. HANSEN, G. RUSSELL, D. RIND, P. STONE[1], A. LACIS, S. LEBEDEFF[2], R. RUEDY[2] AND L. TRAVIS

NASA/Goddard Space Flight Center, Institute for Space Studies, New York, NY 10025

(Manuscript received 11 May 1982, in final form 4 January 1983)

ABSTRACT

A global atmospheric model is developed with a computational efficiency which allows long-range climate experiments. The model solves the simultaneous equations for conservation of mass, energy and momentum, and the equation of state on a grid. Differencing schemes for the dynamics are based on work of Arakawa; the schemes do not need any viscosity for numerical stability, and can thus yield good results with coarse resolution. Radiation is computed with a semi-implicit spectral integration, including all significant atmospheric gases, aerosols and cloud particles. Cloud cover and vertical distribution are computed. Convection mixes moisture, heat and momentum, with buoyant air allowed to penetrate to a height determined by its buoyancy. Ground temperature calculations include diurnal variation and seasonal heat storage. Ground hydrology incorporates a water-holding capacity appropriate for the root zone of local vegetation. Snow depth is computed. Snow albedo includes effects of snow age and masking by vegetation. Surface fluxes are obtained from a drag-law formulation and parameterization of the Monin-Obukhov similarity relations.

The initial Model I is used for 60 climate sensitivity experiments with integration times from 3 months to 5 years. These experiments determine the dependence of model simulation on various physical assumptions and model parameters. Several modifications are incorporated to produce Model II, the greatest changes arising from more realistic parameterization of the effect of boundary layer stratification on surface fluxes and the addition of friction in the top stratospheric layer to minimize effects of wave reflection from the rigid model top. The model's climate simulations are compared to observations and a brief study is made of effects of horizontal resolution. It is verified that the major features of global climate can be realistically simulated with a resolution as coarse as 1000 km, which requires an order of magnitude less computation time than used by most general circulation models.

1. Introduction

There is great incentive for climate modeling based on numerical solution of the fundamental equations for atmospheric structure and motion, i.e., the conservation equations for mass, energy and momentum, and the equation of state. This approach allows explicit modeling of physical processes in the climate system and natural treatment of interactions and feedbacks among parts of the system.

The main obstruction to this approach is computer needs. The requirements specified by the GARP study conference on climate modeling (JOC, 1975) would restrict such modeling to researchers with access to super-computers. However, the computer time varies nearly in proportion to the third power of horizontal resolution, so careful examination of resolution requirements is desirable.

Observations with horizontal resolution of 1000 km are adequate to define the main features of the general circulation. Some studies indicate that much finer resolution is required in general circulation models (Manabe *et al.*, 1970; Wellck *et al.*, 1971), but that conclusion must be model-dependent. In particular, the horizontal viscosity employed in the models used for those studies tends to damp out not only the numerical instabilities at which it is aimed, but also real atmospheric motions when the resolution is coarse (Merilees, 1975).

We have developed a grid-point model[3] which is programmed so that both horizontal and vertical resolutions can easily be changed. In this paper we describe Model I, perform sensitivity experiments by varying parameters and approximation in this model, define an improved Model II, and examine the dependence of climate simulation on resolution with Model II. The sensitivity experiments, only briefly described, are aimed at exposing the model's basic characteristics and helping to determine areas where model development will be most profitable. Some of these sensitivities will be explored further in future papers.

[1] Department of Meteorology and Physical Oceanography, Massachusetts Institute of Technology, Cambridge, MA 12139.

[2] MA/COM Sigma Data, Inc., New York, NY 10025.

[3] This model is distinct from the GISS model of Somerville *et al.* (1974), all physics in Models I and II being developed *ab initio* for climate studies.

We have not modeled several components of the climate system, such as ocean temperature and sea-ice concentration, nor attempted to parameterize atmospheric horizontal transports by subgrid-scale eddies, despite the clear incentive for this in a coarse-resolution model. Our rationale is that we must first establish the capabilities and resolution dependence of the bare atmospheric model.

2. Model description

The model structure is summarized in Section 2a, the fundamental equations in 2b and numerical techniques of solution in 2c. Our main task is computation of local sources and sinks for the conservation equations: friction in the momentum equation and heating in the energy equation. This includes radiative heating (2d), transfer of energy, momentum and mass between atmospheric layers by subgrid scale convection (2e), large-scale cloud processes (2f), ground processes (2g), and interactions between the ground and atmosphere through the surface air layer (2h).

a. Model structure

The model is global in horizontal extent. Resolutions (latitude × longitude) usually employed are 12° × 15°, 8° × 10° (Fig. 1) and 4° × 5°.

Vertical resolution is also variable. We use σ as the vertical coordinate (Phillips, 1957), so the ground is a coordinate surface. The top of the dynamical atmosphere is at fixed pressure p_t, usually 10 mb. The atmosphere above p_t is radiatively interactive with lower levels, with its temperature profile determined by radiation alone. We commonly employ 7-layers and 9-layers with the distribution of layers being (1, 5, 1) and (2, 5, 2) in the boundary layer, and remainder of the troposphere and stratosphere, respectively (Fig. 2).

The model structure at a gridbox is schematically shown in Fig. 3. Each gridbox has appropriate fractions of land and ocean (Fig. 4) based on the (1° resolution) Scripps topography (Gates and Nelson, 1975). Part of the ocean fraction may be covered by ocean ice. Ocean ice cover and surface temperature are specified climatologically (Section 2g) based on

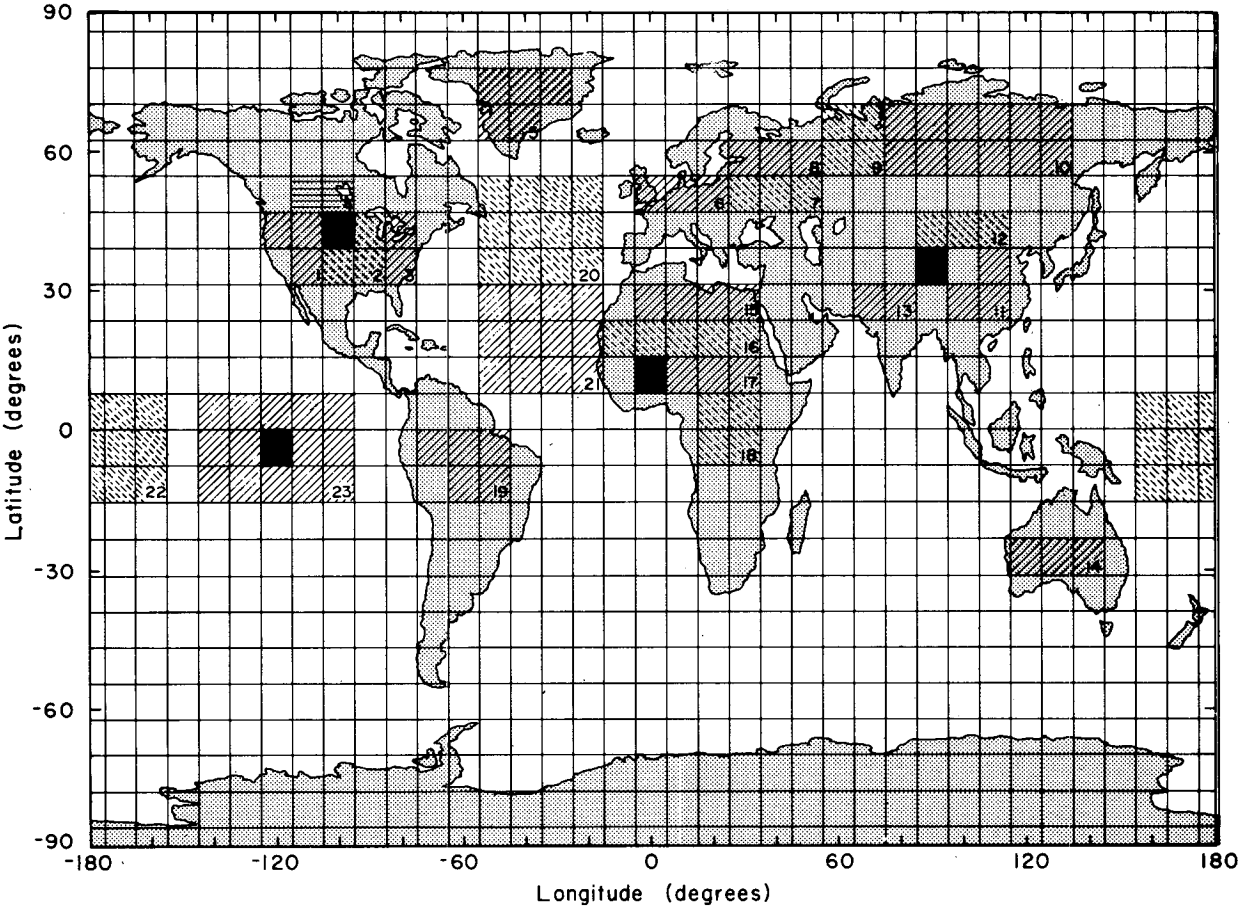

FIG. 1. Grid spacing for 8° × 10° model. Shadings indicate one choice of regions for special monthly diagnostics. The four black regions are a particular choice of gridboxes for hourly diagnostics.

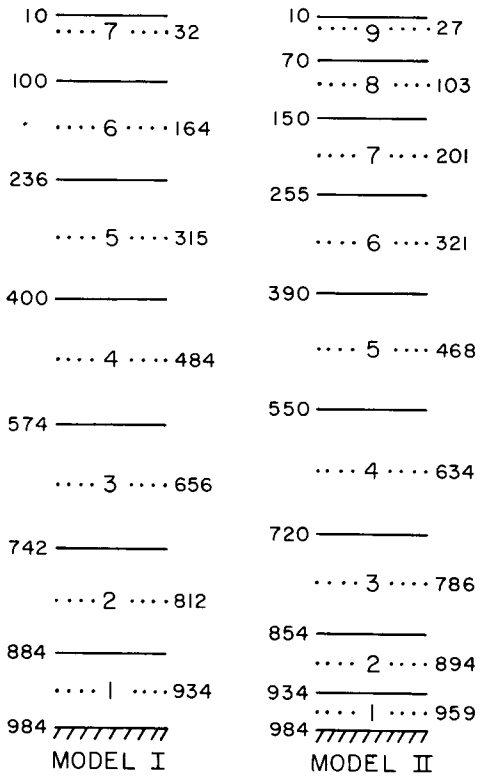

FIG. 2. Global-mean pressure levels (mb) for 7-layer Model I and 9-layer Model II. Layer edges are solid lines, and interior levels are dotted.

monthly-mean values, which are used for the middle of each month and interpolated linearly once per day. Antarctica, Greenland and some Arctic islands are assumed to be covered by ice sheets. Snow may occur

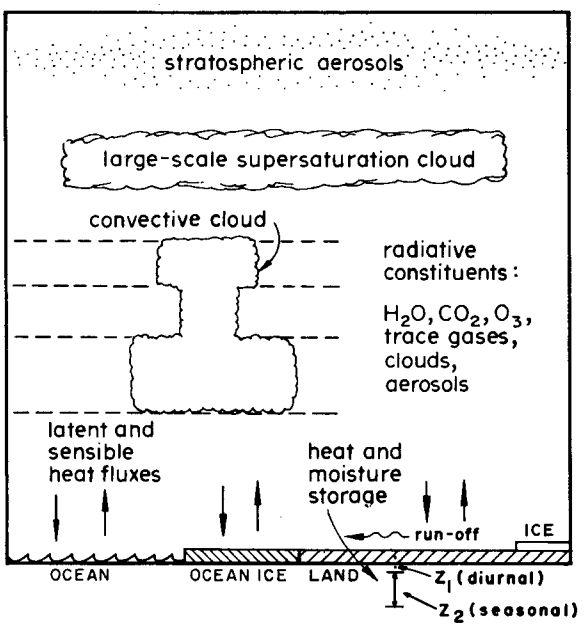

FIG. 3. Schematic illustration of model structure at a single gridbox.

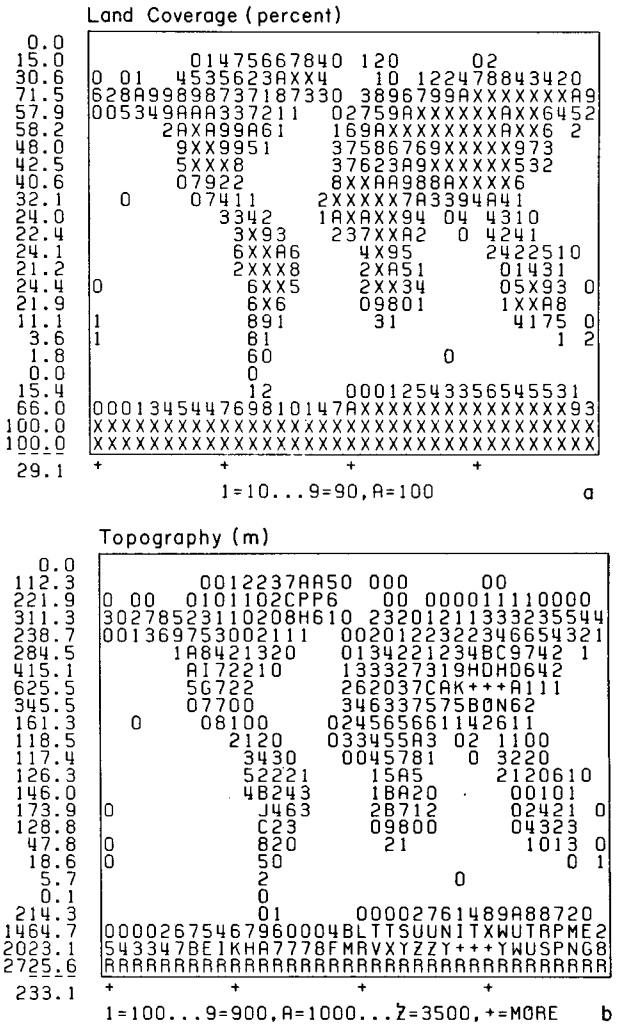

FIG. 4. Digital maps of land coverage and topography for 8° × 10° model. A blank on either map is identically zero. For land coverage 0 is 0–5%, 1 is 5–15%, A is 95–100% and X is exactly 100%. For topography 0 is 0–50 m, 1 is 50–150 m and + is more than 3550 m. Longitudinal averages are on the left, above the area-weighted global average.

on land, land ice and ocean ice, as determined by the model. Interactions between surface and atmosphere are computed separately for each surface type. The area-weighted mean of the 1° Scripps topography is used to specify a topographic height of each gridbox for dynamical calculations (Fig. 4).

The model produces on-line diagnostics, including global maps and zonal means of surface and atmospheric quantities, zonal and longitudinal cross-sections, and spectral analysis of atmospheric energetics and energy transfers. Special areas (Fig. 1) are selected for regional analysis of mean quantities for arbitrary intervals, usually monthly. Several gridpoints are selected for diagnostic output every simulated hour.

Computing time for the 9-layer 8° × 10° Model II is 5 min per simulated day or 30 h per year on

TABLE 1. Fundamental equations.

Conservation of momentum: (Newton's second law of motion)	$\frac{d\mathbf{V}}{dt} = -2\boldsymbol{\Omega} \times \mathbf{V} - \rho^{-1}\nabla p + \mathbf{g} + \mathbf{F}$	(T1)
Conservation of mass: (continuity equation)	$\frac{d\rho}{dt} = -\rho\nabla\cdot\mathbf{V} + C - D$	(T2)
Conservation of energy: (first law of thermodynamics)	$\frac{dI}{dt} = -p\frac{d\rho^{-1}}{dt} + Q$	(T3)
Ideal gas law: (approximate equation of state)	$p = \rho RT$	(T4)

Notation

$\mathbf{V}$	velocity relative to rotating earth
t	time
$\frac{d}{dt}$	total time derivative $\left[=\frac{\partial}{\partial t} + \mathbf{V}\cdot\nabla\right]$
$\boldsymbol{\Omega}$	planet's angular rotation vector
ρ	atmospheric density
$\mathbf{g}$	apparent gravity [=true gravity $-\ \boldsymbol{\Omega} \times (\boldsymbol{\Omega} \times \mathbf{r})$]
$\mathbf{r}$	position relative to planet's center
$\mathbf{F}$	force per unit mass
C	rate of creation of (gaseous) atmosphere
D	rate of destruction of atmosphere
I	internal energy per unit mass $[=c_vT]$
Q	heating rate per unit mass
R	gas content
c_v	specific heat at constant volume.

either the IBM 360/95, a general purpose computer of 1966 vintage, or the Amdahl V-6. The dependence on resolution is

$$\text{time} \propto n_z[0.4(n_xn_y)^{3/2} + 0.6n_xn_y], \qquad (1)$$

where n_x, n_y and n_z are the number of latitudes, longitudes and layers relative to the number for 8° × 10° resolution. The two terms in (1) represent the computations of dynamics and other physics, the dynamics requiring 40% of the computer time for 8° × 10° resolution.

b. Fundamental equations

Table 1 lists the fundamental equations describing the state of the atmosphere, which are discussed in meteorological texts such as Holton (1979). We note here that the equation of motion (T1) is written for a frame of reference rotating with angular velocity Ω; the second term in (T1) is the pressure gradient force. The two terms in the thermodynamic equation (T3) are the work done upon a unit mass in compressing it and the heating rate of all other processes.

Eqs. (T1)–(T4) are transformed for numerical computations as follows: the planet, except for topography, is treated as being a sphere with the atmosphere thin relative to the planetary radius and with $\mathbf{g}$ perpendicular to a radial surface and independent of height. The vertical component of the equation of motion is replaced with the hydrostatic assumption

$$\frac{\partial p}{\partial z} = -g\rho. \qquad (2)$$

This filters out vertical sound waves, permitting longer time steps, and changes the vertical velocity w from a prognostic variable to a diagnostic quantity.

TABLE 2. Approximate form of fundamental equations employed in computations.

	Dependent variable	Equation
$\frac{\partial\pi\mathbf{U}}{\partial t} = -\nabla\cdot\pi\mathbf{U}\mathbf{U} - \frac{\partial\pi\dot{\sigma}\mathbf{U}}{\partial\sigma} - \left(f + \frac{\tan\phi}{a}u\right)\mathbf{k}\times\pi\mathbf{U} - \pi\nabla\Phi - \frac{\sigma\pi}{\rho}\nabla\pi + \pi\mathbf{F}_a$	$\mathbf{U}$	(T5)
$\frac{\partial\pi}{\partial t} = -\nabla\cdot\pi\mathbf{U} - \frac{\partial\pi\dot{\sigma}}{\partial\sigma}$	π, $\dot{\sigma}$	(T6)
$\frac{\partial\pi\Theta}{\partial t} = -\nabla\cdot\pi\mathbf{U}\Theta - \frac{\partial\pi\dot{\sigma}\Theta}{\partial\sigma} + \frac{\pi\Theta}{c_pT}Q$	Θ	(T7)
$\frac{\partial\pi q}{\partial t} = -\nabla\cdot\pi\mathbf{U}q - \frac{\partial\pi\dot{\sigma}q}{\partial\sigma} + \pi(E - C)$	q	(T8)
$\frac{\partial\Phi}{\partial\sigma} = -\frac{\pi}{\rho}$	Φ	(T9)
$p = \rho RT$	ρ	(T4)

Additional notation

$\mathbf{U}$	horizontal velocity in σ coordinates, with components (u, v)
$\nabla\cdot\pi\mathbf{U}\mathbf{U}$	vector with components $[\nabla\cdot(\pi\mathbf{U}u), \nabla\cdot(\pi\mathbf{U}v)]$
$\nabla\cdot A\mathbf{U}$	horizontal divergence $\left[=\frac{1}{a\cos\phi}\left(\frac{\partial Au}{\partial\lambda} + \frac{\partial Av\cos\phi}{\partial\phi}\right)\right]$
∇A	horizontal gradient $\left[=\frac{1}{a}\left(\frac{1}{\cos\phi}\frac{\partial A}{\partial\lambda}, \frac{\partial A}{\partial\phi}\right)\right]$
a	mean planetary radius
ϕ	latitude in radians
λ	longitude in radians
σ	vertical coordinate $[=(p - p_t)/\pi]$
E	rate of evaporation
$\dot{\sigma}$	$d\sigma/dt$
π	$p_s - p_t$, where p_s is the surface pressure and p_t the constant pressure at the model's upper boundary
Θ	potential temperature $[=T(p_{00}/p)^\kappa$, where $\kappa = R/c_p$ and p_{00} = 1000 mb]
Φ	geopotential $[=gz$, where z is height above sea level]
f	Coriolis parameter $[=2\Omega\sin\phi]$
c_p	specific heat at constant pressure
F_a	horizontal frictional force
q	water vapor mixing ratio
C	rate of condensation.

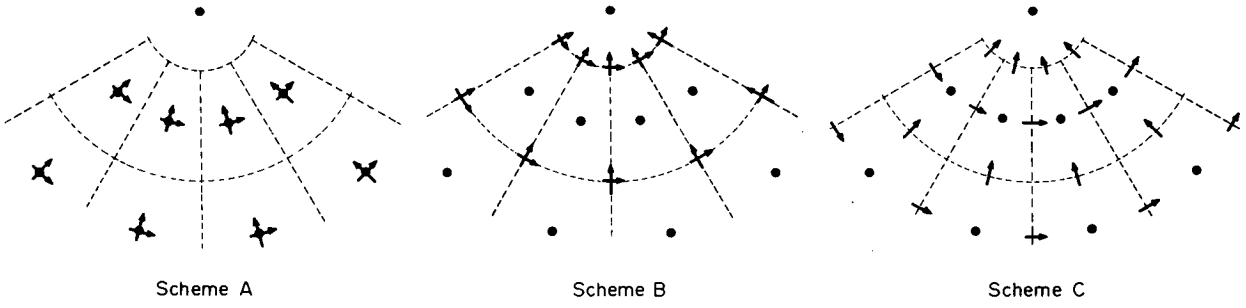

FIG. 5. Horizontal grid schemes A, B and C. Dots are primary gridpoints where pressures and temperatures are computed. Arrows are secondary gridpoints where horizontal winds are computed.

The water vapor distribution is computed from the equation for conservation of water substance, and condensation heating is included in the total heating rate. The smaller impact of water vapor changes on the gas constant R and on surface pressure is neglected. After introducing the vertical coordinate σ and potential temperature Θ, the fundamental equations take the form in Table 2. This is the complete system of equations employed in computations except for definition of constants, source terms and boundary conditions. Note that both σ and π are obtained from (T6), π by integrating the equation with respect to σ from 0 to 1 and assuming the boundary condition $\dot{\sigma} = 0$ at $\sigma = 0$ and at $\sigma = 1$, as discussed below.

c. Numerics

In this section we specify numerical procedures used in Model I, tests to study model sensitivity to the formulations, and changes incorporated into Model II. Approximations in representing physical processes are discussed in Sections 2d–2h.

1) SPATIAL DIFFERENCING

Several horizontal gridding schemes, each with certain advantages are shown in Fig. 5. Grid A, used in the GFDL (Manabe *et al.*, 1965, 1975) and NCAR (Kasahara and Washington, 1967; Washington and Williamson, 1977) models, is perhaps the simplest. However, all centered differences must be computed over $2\Delta x$, where Δx is the grid spacing, while on grids B and C the pressure gradient and velocity divergence are computed over Δx, resulting in more accurate representation of geostrophic adjustment (Arakawa, 1972).

We employ grid B in run 1 of Model I (run I–1), which is the control case for most of our sensitivity studies. In run I–2 (Table 3) we tried grid C. With $8° \times 10°$ resolution, grid C produces excessive kinetic energy at large wavenumber n, the kinetic energy spectrum being flat at $n > 6$ (Fig. 6a). This arises from the calculation of kinetic energy generation by the horizontal pressure gradient force in the momentum equation (T5), given in σ coordinates by

$$-\pi \mathbf{U} \cdot \left(\nabla_\sigma \Phi + \frac{\sigma}{\rho} \nabla \pi \right), \tag{3}$$

the dot product of the wind vector and pressure gradient. This term is calculated directly from model-generated quantities on grid C, but on grid B it is necessary to average the horizontal pressure gradient force to obtain its value at the points where the winds are calculated. This implicit smoothing on grid B reduces high-frequency noise. In run I–3 we arbitrarily introduced the same smoothing on grid C. This caused the kinetic energy spectrum to be similar to that for run I–1, i.e., the high-frequency noise disappeared. Run I–4 employed $4° \times 5°$ resolution with grid C. This caused the noise in the kinetic energy to move to higher wavenumbers, i.e., the spectrum became flat for $n > 12$.

Arakawa and Lamb's (1981) potential enstrophy conserving differencing method was tested in run I–5. Since this method uses the C grid, it also produces a great amount of noise in the kinetic energy spectrum (Fig. 6). Both of the sensitivity experiments which used the C grid, $8° \times 10°$ horizontal resolution, and no arbitrary smoothing (runs I–2 and I–5) caused the eddy kinetic energy and northward transports of latent and sensible heat to increase $\sim 50\%$ (7σ)[4] and yielded unrealistic temperature and wind fields.

We use the B grid spatial differencing of Arakawa (1972) for the control runs of both Models I and II, with the following exceptions. Potential temperature, rather than temperature, is used as a prognostic variable in both Models I and II, thus avoiding the need for a computationally inefficient conversion factor in the energy equation. The Coriolis force and metric term (spherical geometric factor) are included at the

[4] We specify the number of standard deviations by which a quantity changed in a typical month of the sensitivity experiment. Only changes occurring in all relevant months (at least three) are mentioned, so a change of 2σ is highly significant. Standard deviations are from the 5-year run I–1.

TABLE 3. Sensitivity experiments. Run I-1 is the control unless otherwise indicated.

Model run	Simulated months	Experiment description
I-1	60	Control run for most experiments, 8° × 10° resolution, 7 layers
I-2	9	C grid
I-3	3	C grid with smoothing of the horizontal pressure gradient force
I-4	3	C grid, 4° × 5° resolution
I-5	9	C grid, potential enstrophy conservation
I-6	9	Coriolis and metric terms included at poles
I-7	12	Momentum drag in top model layer
I-8	12	Model I with surface physics and radiation of Model II
I-9	3	I-8 with drag in stratosphere, $C_{DN} = 10^{-5}$
I-10	3	I-8 with drag in stratosphere, $C_{DN} = 10^{-4}(5 + 0.5U)$
I-11	3	I-8 with drag in stratosphere, $C_{DN} = 10^{-3}$
I-12	3	I-8 with model top at 0.01 mb, 21 layers, no drag in stratosphere
I-13	18	10-layer model, 3 layers added in upper troposphere and stratosphere
I-14	18	12-layers; 2 layers added in planetary boundary layer to Run I-13
I-15	3	Matsuno TASU time stepping
I-16	3	No smoothing toward poles, 2 min time step
I-17	3	No sea level pressure filter
I-18	3	GFDL horizontal diffusion
I-19	3	NCAR horizontal diffusion
I-20	3	25% limit on horizontal advection of water vapor
I-21	3	Vertical advection of H_2O vapor uses arithmetic mean at layer edges
I-22	3	No friction, i.e., no surface drag or momentum mixing by convection
I-23	3	Aerosols omitted
I-24	9	IR radiation of Model II (single k-distribution for each gas)
I-25	9	Realistic IR emissivities for deserts, snow and ice
I-26	9	Radiation computed at all gridpoints; run I-1 uses 2-point mean
I-27	9	Complete radiation calculation every hour
I-28	3	Daily average solar insolation, i.e., no diurnal cycle
I-29	9	No subgrid-scale temperature variance for moist convection
I-30	9	Moist adiabatic adjustment
I-31	9	Moist convection cloud constant (γ) tripled
I-32	3	Radiation computed separately in cloudy/noncloudy areas of gridbox
I-33	9	No mixing of momentum by convection
I-34	9	Moist convection can start below the condensation level
I-35	9	No subgrid-scale temperature variance for supersaturation clouds
I-36	3	Large-scale rainfall calculated every 5 h
I-37	9	Fixed annually averaged clouds
I-38	3	Fixed annually averaged and longitudinally averaged clouds
I-39	3	Local temperature 0°C criterion for saturation over water or ice
I-40	3	Local temperature −40°C criterion for saturation over water or ice
I-41	3	Local temperature −65°C criterion for saturation over water or ice
I-42	12	Optical thickness of cirrus clouds reduced to $\tau = \frac{1}{3}$
I-43	12	Optical thickness of other non-convective clouds reformulated
I-44	21	Snow density decreased from 0.25 to 0.1 g cm^{-3}
I-45	9	Modified thermal conductivity in deserts and vegetated areas
I-46	9	Increased field capacity based on vegetation type; I-8 is control
I-47	9	Instant upward water diffusion from root zone; I-46 is control
I-48	9	No runoff until first ground layer is saturated; I-47 is control
I-49	11	Intermediate runoff formulation; I-47 is control
I-50	9	Increased masking depths based on vegetation type
I-51	9	Modified ground albedo based on vegetation type
I-52	3	Ocean ice coverage based on Walsh and Johnson (1979)
I-53	24	No fractional grid for land/water
I-54	12	Ocean surface temperature based on Robinson and Bauer (1981)
I-55	9	Lower limit for surface roughness based on vegetation
I-56	3	Surface layer height of 30 m used over the ocean
I-57	9	Ekman surface wind formulation with specified α_0
I-58	9	First layer wind employed for Ekman wind calculation
I-59	3	Varying boundary layer height for Ekman wind calculation
I-60	3	Geostrophic wind used for Ekman wind calculation
I-61	9	Modified cross-isobar angle calculation; I-59 is control

pole grid points in Model II, but not in Model I or in Arakawa's (1972) description of the spatial differencing. Run I-6 showed that the primary effect of adding these terms was to introduce a noticeable direct polar cell in the mean meridional circulation. This change is an improvement of the model's sim-

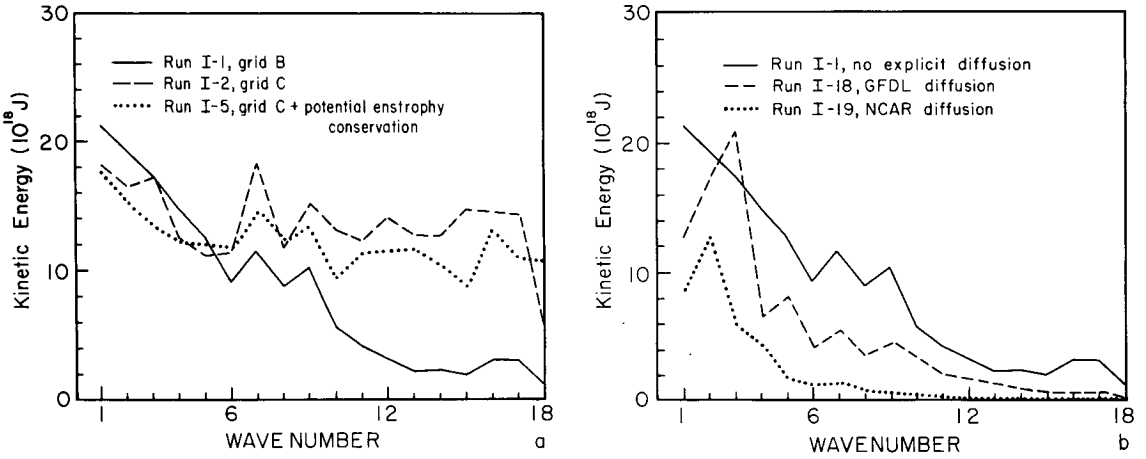

FIG. 6. Kinetic energy spectrum of the Northern Hemisphere troposphere in January. Fig. 6a compares grid C results with grid B. Fig. 6b compares different diffusion formulations. Run I-1 results are the mean for the five Januarys of a 5-year run.

ulation of observed high-latitude circulation (Section 3).

The vertical differencing scheme employs the σ coordinate system; σ is a linear function of pressure at each horizontal gridpoint, varying from $\sigma = 1$ at the ground to $\sigma = 0$ at $p = p_t$, the upper boundary of the atmospheric region for which the dynamics is computed. The atmosphere is divided into a fixed number of layers which are thus compressed in regions of high topography. Variation of layer thickness with height is chosen to be smooth to minimize computational error (Kálnay de Rivas, 1972). Potential temperature and winds are computed at interior points of each layer, with fluxes computed at layer edges.

The σ coordinates simplify the lower boundary condition, correctly given by

$$\dot{\sigma} = 0 \quad \text{at} \quad \sigma = 1. \tag{4}$$

A similar upper boundary condition is used,

$$\dot{\sigma} = 0 \quad \text{at} \quad \sigma = 0, \tag{5}$$

which in effect places a rigid lid at p_t. This rigid lid can (unrealistically) reflect wave energy propagating from below, thus distorting the solutions at all levels, especially in the upper layers. Introduction of a "sponge" layer to damp out reflections has yielded only mixed success (Arakawa and Lamb, 1977). A more natural approach is to place the model top high enough that unwanted waves are radiatively damped, but that requires a large number of model layers.

We introduced a momentum drag in the top model layer to minimize distortions due to the rigid model top, the form of the drag in run I-7 being

$$\tau = -\rho C_{DN} U \mathbf{U}, \tag{6}$$

where C_{DN} is the neutral drag coefficient over ocean (Garratt, 1977; Section 2h), representing a value far from topographical effects. Breaking gravity waves may provide such a drag in the mesosphere (Holton and Wehrbein, 1980), and thus dissipate and isolate the stratospheric jet stream. Although the drag must be introduced at an unrealistically low altitude in the 7-layer Model I (top layer is ~100–10 mb), it serves to remove kinetic energy which would otherwise build up in the top layer. This improves the simulation of stratospheric winds and temperatures at high latitudes and yields a realistic tropopause.

The influence of stratospheric drag was studied with a modified version of Model I as control, run I-8, which included the surface layer formulation of Model II (cf. Section 2h). Run I-8 has more realistic tropospheric eddy energy than I-1 and thus it is warmer at high latitudes in winter, but it still has no clear tropopause at high latitudes; the static stability is 20% less than observed at high latitudes in winter and the mean surface pressure is too low (Table 4). Run I-9 employed a small drag ($C_{DN} = 10^{-5}$) and runs I-10 and I-11 a larger value (10^{-3}). The drag reduced the wind shear in the stratosphere and thus reduced the latitudinal temperature gradient there. The warmer lower stratosphere increased the tropospheric static stability and sea level pressure. The results were not very sensitive to the value of the drag, provided it was large enough to prevent stratospheric kinetic energy from growing.

In run I-12 we raised the model top out of the stratosphere (to 0.01 mb or ~75 km), used approximately 2 layers per pressure scale height, and omitted the drag in the stratosphere. The effects on temperature structure and winds in the lower stratosphere were generally similar to those in run I-10, providing some justification for inclusion of stratospheric drag. Although it would be preferable to remove energy by radiative damping as in I-12, it is impractical to employ a high model top and many layers in most long climate experiments. Thus we included drag in the top layer in Model II using the form of run I-10.

TABLE 4. Influence of stratospheric drag, January simulation.

Run	C_{DN} (U in m s^{-1})	Stratospheric kinetic energy dissipation (percent per time step)	59°N Temperature (K) 200 mb	59°N Temperature (K) 100 mb	Tropospheric static stability (K km^{-1})	Sea level pressure (mb)
8	0	0	−67	−72	5.6	1009
9	10^{-5}	6.5	−65	−65	5.8	1011
10	$10^{-4}(5 + 0.5U)$	9.4	−63	−58	6.5	1018
11	10^{-3}	10	−64	−60	6.3	1016
Observations	—	—	−58	−57	7.1	1015

The effect of vertical resolution was tested in several sensitivity experiments with Model I. Run I–1 has seven layers with one layer clearly in the stratosphere and one layer in the lowest 100 mb (Fig. 2). In run I–13 the resolution in the stratosphere and upper troposphere was increased by adding three layers there. Principal effects were an improved definition of the jet stream, a 15% (2σ) increase in the jet stream velocity, and about a 25% (2σ) increase in northward transports of energy and momentum by eddies, with the latter increases mainly in the upper troposphere. The vertical resolution in the planetary boundary layer was increased in run I–14 by adding two layers there, with run I–13 serving as the control. This resulted in a 25% (3σ) increase of tropospheric eddy kinetic energy, the increase being primarily in waves of 3–7 day period and apparently arising from improved resolution of the regions where baroclinic activity and long waves are generated. Northward transport of energy also increased and raised the zonal mean atmospheric temperature by about 5°C (2σ) at latitudes 50–90°N. The definition of the Aleutian High in the stratosphere was much improved in run I–14.

A compromise between high vertical resolution and computational speed was chosen for the control run of Model II (run II–1). Nine layers were employed, with one layer added in the stratosphere and one in the planetary boundary layer, compared to the 7-layer run I–1. This was sufficient to obtain most of the benefit of improved vertical resolution found for runs I–13 and I–14.

2) TIME DIFFERENCING

Source terms ("physics," consisting of friction, heating and evaporation/condensation) for the prognostic equations in Table 2 are integrated explicitly each hour. Non-source terms ("dynamics") are integrated using a leap-frog scheme initiated each hour with an Euler-backward step:

$$
\begin{aligned}
U^{*} &= U^{0} + \tfrac{2}{3}\Delta t f(U^{0}) \\
U^{1} &= U^{0} + \Delta t f(U^{*}) && \text{Euler-backward} \\
U^{2} &= U^{0} + 2\Delta t f(U^{1}) && \text{leap-frog} \\
&\vdots && \vdots \\
U^{n-1} &= U^{n-3} + 2\Delta t f(U^{n-2}) && \text{leap-frog} \\
U^{n'} &= U^{n-2} + 2\Delta t f(U^{n-1}) && \text{leap-frog} \\
U^{n} &= U^{n'} + \Delta t_s g(U^{n'}) && \text{source term integration}
\end{aligned}
\qquad (7)
$$

Fig. 7 shows this time differencing procedure. Δt is 15 min for 8° × 10° resolution, 7.5 min for 4° × 5° and 20 min for 12° × 15°. Δt_s is always 60 min. However, several steps may be used during the source term integration, depending on the thickness of the lowest atmospheric layer: Model I uses a single 60 min step, but Model II uses two successive 30 min steps.

Other time differencing schemes were tried. Run I–15, for example, employed the Matsuno (1966) TASU (time alternating space uncentered) time step. This decreased the atmospheric eddy kinetic energy by 40% (4σ), a result of the diffusive character of the Matsuno TASU scheme. Such diffusion is especially detrimental in a coarse resolution model.

3) SMOOTHING

Little smoothing is employed in our computations. In Models I and II it consists of 1) longitudinal averaging near the poles of selected terms in the prognostic equations, and 2) a weak sea-level pressure filter.

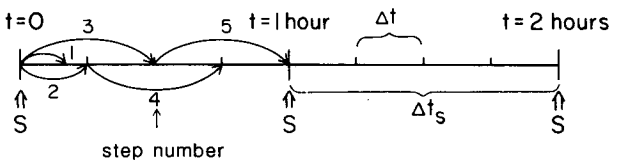

FIG. 7. Schematic representation of the time differencing for 8° × 10° resolution [cf. Eq. (6)]. S indicates when the source terms are integrated.

Smoothing near the poles permits use of a longer finite difference time step than would otherwise be possible. It is applied to only the terms which would cause computational instability as a result of the poleward convergence of meridians, i.e., the longitudinal pressure gradient force in the momentum equation and the longitudinal divergence in the energy, mass and momentum equations. The smoothing is performed with a Fourier filter, which reduces longitudinal variations for scales smaller than the latitudinal grid spacing, $a\Delta\phi$ (Arakawa and Lamb, 1977, p. 248). Run I–16 employed a 2-min time step which allowed the smoothing toward the poles to be omitted. There was no large change in the model-generated climate, the largest effects being an increase of several percent in the poleward transport of angular momentum and a poleward shift of the interpolated jet stream location by as much as ~3° in some months.

A longitudinal eighth-order Shapiro (1970) filter is applied to the sea level pressure every 2 h to reduce a checkerboard pattern of small-amplitude noise which occurs in the grid B finite-differencing procedure. Run I–17, which excluded the filter, verified that it does not affect the general circulation. The main impact of the filter is removal of 2-gridpoint noise in the geopotential height field in the lower troposphere, which is especially noticeable at low latitudes where gradients are weak. The 2-gridpoint noise remains visible in stratospheric temperature and faintly visible in precipitation.

We also introduced diffusion into the horizontal momentum equation to help analyze the conclusions of Manabe *et al.* (1970) and Wellck *et al.* (1971) about coarse resolution models. Run I–18 employed the GFDL formulation for diffusion (Manabe *et al.*, 1970) and run I–19 the NCAR formulation (Wellck *et al.*, 1971). The vertically integrated eddy kinetic energy is reduced more than a factor of 2 in both cases (Fig. 6). Although the fractional reduction is greatest at large wavenumbers, a large decrease extends through synoptic scales. Reduced poleward transports of energy accompany the decreased eddy activity, and high-latitude temperatures are as much as 10°C (5σ) colder in winter.

4) TRANSPORT OF TRACERS AND WATER VAPOR

The model has an option for carrying tracers, which are moved by horizontal and vertical advection and by convection and are radiatively and chemically inert. The tracers have their own arbitrary initial distributions, and thus can serve as a useful model diagnostic. Time differencing for tracers and water vapor is as for other quantities [Eq. (7)], except the Euler-backward steps are replaced by a single forward step. This minimizes storage and computation requirements without major loss of accuracy.

Horizontal advection of tracers and water vapor is computed in the same way as for potential temperature, except that a condition is imposed that no more than half of the substance can move out of a gridbox in either direction in one time step. This condition assures that negative mixing ratios do not occur. A more stringent limit of 25% was imposed in run I–20, with no noticeable effects.

Vertical differencing of tracers and water vapor is as described by Arakawa and Lamb (1977) for ozone, except specification of substance amount at layer edges. For tracers we use the arithmetic mean of tracer amount in the two adjoining layers. However, for water vapor, which usually decreases rapidly with increasing altitude we use the harmonic mean. Run I–21 tested this interpolation procedure by using the arithmetic mean of water vapor in adjoining layers. The primary effect was an increase of stratospheric water vapor by about a factor of 2 (5σ). There was no significant change in the general circulation or temperature, but if the ocean surface temperature were not fixed, the atmospheric and surface temperatures probably would have increased by about 1°C (Wang *et al.*, 1976). The stratospheric water vapor computed with the harmonic mean was closer to observations (Harries *et al.*, 1976), and thus this interpolation was retained for water vapor in Model II.

5) CONSERVATION OF INTEGRAL PROPERTIES

It is desirable that the finite differencing conserve fundamental integral properties known to be invariant during the physical process being simulated. We employ differencing schemes of Arakawa which approximately conserve the following globally integrated properties in time: advection conserves mass (<0.0001) and potential temperature (0.003), where the parenthetical number is the error (percent per day); advection conserves kinetic energy (0.004); the Coriolis force does not change kinetic energy (<0.0001); advection and the Coriolis force conserve total angular momentum (0.0005); and the dynamics does not change total energy (0.003). Numerical truncation of temperature causes more than 90% of the deviation from conservation of total energy. In an experiment with no topography, the vertically and zonally integrated pressure gradient force on total angular momentum was conserved at each latitude (<0.0001); thus the integrated pressure gradient force conserves angular momentum except for the effect of the surface on the atmosphere.

The conservation properties of Arakawa's differencing schemes permit stable integration of the fundamental equations with little artificial diffusion or smoothing. As a test of this concept, run I-22 employed no kinetic energy loss mechanisms; the surface drag was set to zero and mixing of momentum by convection was omitted. Thus radiation was the only loss mechanism for the energy received from the sun. The model ran without difficulty, reaching a stable climate with eddy kinetic energy about three times larger than in the control run and northward transport of energy and momentum increased by about a factor of 2. The slope of the kinetic energy spectrum was similar to that of the control run.

We conclude that Arakawa's differencing schemes with grid B permit the use of coarse resolution without numerical diffusion and the loss of eddy energy which that would entail. In Section 3 we show that the climatology produced with coarse resolution is realistic.

d. Radiation

The radiation heating term in the energy equation [(T3), (T7)] includes heating by absorption of solar radiation and cooling (or heating) by absorption and emission of terrestrial radiation. This term should be accurate throughout the troposphere and stratosphere and properly responsive to climate changes in the temperature-pressure profile, cloud distribution or atmospheric composition. The major difficulties are 1) accurately integrating over complex and overlapping absorption bands which greatly change characteristics with height, and 2) accurately including effects of multiple scattering.

Our correlated k-distribution method is a generalization of the approach of Lacis and Hansen (1974). Vertical inhomogeneity of the atmosphere is accounted for by assuming a simple correlation of k-distributions at all temperatures and pressures; by means of "line-by-line" calculations we show below that the method is accurate even for the notoriously difficult 9.6 μm ozone band.

All radiatively significant atmospheric constituents are included. Realistic spectral properties of clouds and aerosols are used, based on Mie computations (Hansen and Travis, 1974). Thus the treatments in the solar and thermal regions are consistent and crude assumptions such as black or "half-black" clouds are avoided. The diurnal cycle is explicitly included.

1) CORRELATED K-DISTRIBUTION METHOD

The k-distribution $f(k)$ is the probability density function such that $f(k)dk$ is the fraction of a specified frequency interval with absorption coefficient between k and $k + dk$. Grouping of gaseous spectra according to absorption coefficient goes back at least to work of Ambartsumian (1936) on stellar atmospheres. Lacis and Hansen (1974) used k-distributions to include effects of multiple scattering, deriving a mean k-distribution for water vapor and scaling the gas amount as a function of pressure and temperature to crudely account for atmospheric inhomogeneity.

Our generalization of this method (Fig. 8) more accurately treats atmospheric inhomogeneity. It is based on the assumption that k-distributions at all altitudes are correlated in frequency space, e.g., the strongest absorption occurs at the same frequency at all altitudes. Maintenance of the rank of absorption coefficients throughout the atmosphere is rigorously correct for a single spectral line with fixed center or a uniform Elsasser (1942) band model.

The k-distribution is formally related to the transmission function Γ by

$$\Gamma(\zeta) = \frac{1}{\Delta\nu}\int_{\Delta\nu} e^{-k_\nu \zeta} d\nu = \int_0^\infty f(k) e^{-k\zeta} dk, \qquad (8)$$

where ζ is the gas amount. Because of its convenient mathematical properties, we choose the Malkmus (1967) model to represent $\Gamma(\zeta)$, i.e.,

$$\Gamma(\zeta) = \exp\{-\tfrac{1}{2}\pi B[(1 + 4S\zeta/\pi B)^{1/2} - 1]\}, \qquad (9)$$

where S and B are the effective line strength and line width. Since $f(k)$ is the Laplace transform of $\Gamma(\zeta)$ we obtain the k-distribution directly as

$$f(k) = \tfrac{1}{2}k^{-3/2}(SB)^{1/2} \times \exp[\tfrac{1}{4}\pi B(2 - kS^{-1} - Sk^{-1})]. \qquad (10)$$

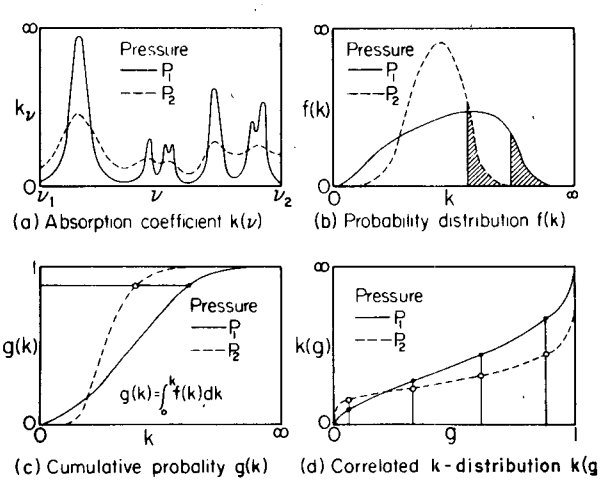

FIG. 8. Correlated k-distribution method. Fig. 8a is a schematic absorption line spectrum at two pressures, 8b the probability density of absorption coefficients. The broadened spectrum has a narrower k-distribution. The shaded areas depict the strongest absorption for both pressures and are assumed to refer to the same spectral interval. Fig. 8c is the cumulative probability density, 8d the correlated k-distribution. Integration over g replaces integration over ν.

This can be integrated analytically to yield the cumulative probability

$$g(k) = \int_0^k f(k')dk'. \quad (11)$$

We obtain the k-distribution for a given gas and frequency interval by using line coefficients tabulated by McClatchey *et al.* (1973) and Rothman (1981) to compute line-by-line absorption at a range of pressures and temperatures. We obtain a table of S and B parameters by least-square fitting the Malkmus model to the line-by-line results. This yields band model parameters which fit the line-by-line data within ~1% from the ground to ~70 km. Change of line shape with altitude is accounted for by using the Voigt line profile.

The error in this method is illustrated in Fig. 9 for thermal cooling by the 9.6 μm ozone band. The solid curve was obtained from line-by-line computations for 2×10^5 frequencies and the dashed curve from the correlated k-distribution approach with five values of k which vary with pressure and temperature. Computing times differ by a factor of 4×10^4. This test suggests that blurring of the assumed correlation with height, due to overlapping of lines with differing strength and temperature dependence, is small.

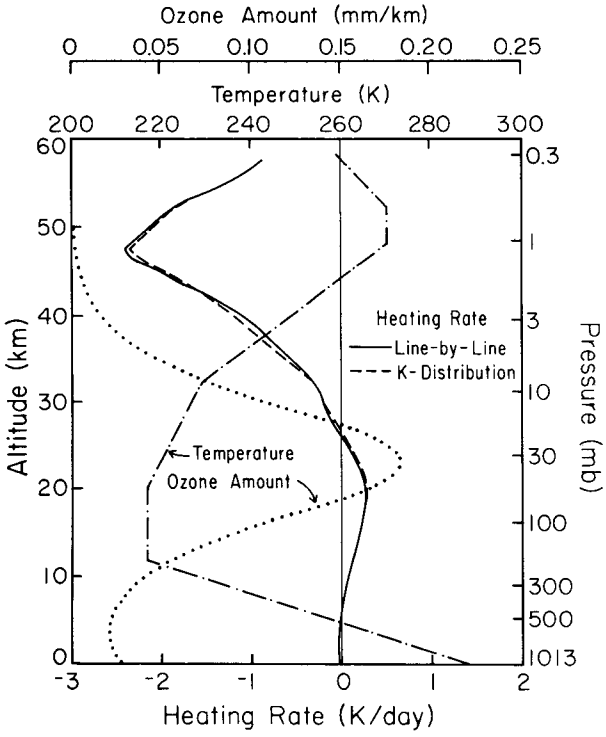

FIG. 9. Atmospheric cooling by the 9.6 μm ozone band for the indicated temperature distribution and ozone concentration. The solid line is from line-by-line integration and the dashed line from the correlated k-distribution method.

2) SOLAR RADIATION

We modify the solar radiation treatment of Lacis and Hansen (1974) to obtain accurate results at all solar zenith angles (θ_0) and all layer optical thicknesses (τ). We introduce a "single Gauss point" (SGP) adaptation of the doubling and adding equations in which integrations over zenith angle θ are handled with one Gauss point, $\bar{\mu} = \cos^{-1}\bar{\theta} = 0.5$, and θ_0 is treated as an "extra" angle (Lacis and Hansen, 1974). The doubling equations are used to obtain the reflection and transmission of each homogeneous atmospheric layer, with the calculations initialized by analytic expressions accurate for $\tau \leq 0.03$. Single-scattering phase function information is included in the form of downward and upward fractions of the scattered radiation, tabulated as a function of θ_0. The adding equations are used to compute the upward and downward fluxes at layer boundaries and thus heating rates (Lacis and Hansen). Comparison with results based on precise angle integration indicates errors usually <10%. The SGP method is well-suited for computations in a many-layered atmosphere because the computing time varies only linearly with the number of layers.

Gaseous absorbers included in the solar radiation are H_2O, CO_2, O_3, O_2 and NO_2. Multiple scattering computations are made for 12 k profiles: 5 for H_2O, 3 for CO_2, 3 for O_2 and 1 for NO_2. Strong (line center) absorption is not included in the 12 k profiles; instead it is computed separately for H_2O, CO_2 and O_2 as exponential absorption of the direct solar beam. The k-distributions for H_2O, CO_2 and O_2 are based on line-by-line calculations weighted by the solar spectrum. NO_2 absorption is included in a single interval as a mean absorption coefficient based on measurements by Hall and Blacet (1952). The analytic expression of Lacis and Hansen is used for O_3 absorption. Absorption and scattering by aerosols is included using aerosol radiative properties obtained from Mie calculations for the global aerosol climatology of Toon and Pollack (1976). We use six intervals for the spectral dependence of Mie parameters for clouds, aerosols and Rayleigh scattering. The six spectral intervals are superimposed with the 12 k profiles where appropriate to account for overlapping absorption.

The effect of aerosols on the model's climatology is tested in Run I–23 by removing the aerosols. The planetary albedo decreased by about 0.01 (3% of its value). This did not significantly affect the atmospheric circulation or temperatures, no doubt a consequence of the fixed ocean surface temperature.

Ocean albedo is a specified function of surface wind speed and solar zenith angle:

$$A = 0.021 + 0.0421x^2 + 0.1283x^3 - 0.04x^4 + \frac{3.12x^5}{5.68 + V_s} + \frac{0.074x^6}{1 + 3V_s}, \quad (12)$$

where V_s is in m s^{-1} and x is $1 - \mu_0$. This parameterization is based on calculations of Fresnel reflection from wave surface distributions as a function of V_s as specified by Cox and Munk (1956).

The albedo of land is taken from Posey and Clapp (1964) for Model I. In Model II the land albedo is a function of vegetation type including seasonal variations and separate albedos for the visible and near-infrared regions (Section 3). Surface albedo is modified by snow cover, as described in Section 2g.

The solar irradiance is taken as 1367 W m^{-2} (Willson, 1978).

3) THERMAL RADIATION

Model I uses the correlated k-distribution method and a parameterized two-stream approximation to compute thermal cooling. Similarity relations (Hansen, 1969) are used to scale the optical thickness (τ) and single scattering albedo (ω) of aerosols and clouds to values appropriate for isotropic scattering. For convenience, the Planck function is taken as varying linearly with optical thickness through each layer.

The two-stream method of Model I is accurate for a single layer, but loses accuracy when optically thin scattering layers are combined via the adding method. Thus scattering effects are included in Model II in a less direct way. Thermal radiation fluxes are computed formally without scattering ($\omega = 0$), but scattering effects are included parametrically via emissivity of clouds (from off-line computations) and ground. Model II uses three quadrature points to define the angular distribution of radiation. This improves the accuracy in adding layers and eliminates the need for exponential integrals, thus yielding greater speed.

The thermal radiation calculations include the major absorption bands of H_2O, CO_2 and O_3, as well as weaker bands of CO_2, O_3, N_2O and CH_4 which are important for certain applications (Wang *et al.*, 1976). The k-distributions are specified in Model I by between 2 and 9 probability intervals in each of six spectral bands with edges at 0, 400, 650, 850, 1200, 1500 and 2500 cm^{-1}. Infrared continuum absorption by water vapor is incorporated including pressure, vapor pressure and temperature dependence based on expressions given by Roberts *et al.* (1976).

In Model II one k-distribution is defined for each gas for the entire thermal region, with 11 k intervals for H_2O, 10 for CO_2 and 4 for O_3. A large table of absorption coefficients (spectrally weighted by the Planck function) as a function of temperature, pressure and absorber amount is used. Run I–24 tested this spectral integration technique. The computation time for radiation was reduced 30%, compared to run I–1. Accuracy also improved, as shown by comparison with calculations in a one-dimensional model including a high density of spectral intervals.

Ocean emissivity is parameterized in Models I and II as

$$\epsilon = 1.008 - 0.029(1 + V_s)^{-1} + 0.015(1 + V_s)^{-2} - (1.017 - 0.008V_s)A_2(\nu), \quad (13)$$

where $A_2(\nu)$ is the ocean albedo for wind speed $V_s = 2$ m s^{-1}, based on calculations of Fresnel reflection for the wave surface distribution of Cox and Munk (1956). Land emissivity is defined as unity in Model I. Spectral dependence of emissivities of deserts (Hovis and Callahan, 1966) and snow and ice (Wiscombe and Warren, 1980) is included in Model II. Run I–25 showed that, for fixed ocean temperature, this had little effect on the general circulation or atmospheric temperatures.

Computation time can be reduced by performing the radiation computations at only every nth gridpoint, interpolating to other points and rotating the computation grid to minimize systematic error. In runs I–1 and II–1 we use 2-point averaging, calculating the radiation at alternate longitudes and all latitudes. Run I–26 verifies that effects on mean monthly climate are small.

Complete radiation calculations are performed once every 5 h in Models I and II. Change of solar heating in the 5 h is approximated by taking the albedo and heating rate per unit irradiance as constant, but exactly including temporal variation of solar irradiance at the top of the atmosphere. Calculation of thermal emission in the 5 h includes change of ground temperature, which varies rapidly, but not change of atmospheric temperature. Run I–27 tests these approximations by means of complete radiation calculations every hour. The general circulation is not noticeably affected. Some distortion of the diurnal cycle occurs for quantities such as temperature and evaporation for a given gridpoint and day. However, the monthly-mean diurnal cycle is not affected much.

In run I–28 the diurnal cycle for solar radiation was suppressed. Although daily mean insolation was unchanged, the mean surface air temperature increased 5–10°C over most land areas. Constant insolation made the atmosphere less stable at "night" than in run I–1, and thus the surface layer was in an unstable region all day. With the diurnal cycle included, stable conditions isolate the surface layer at night and allow it to cool, yielding a lower daily mean temperature.

e. Convection

Convection is a key subgrid-scale process causing vertical transport of moisture, sensible heat and momentum in addition to determining precipitation and clouds, which couple dynamical and radiative processes in the atmosphere. The simplest convective parameterization is adiabatic adjustment (Manabe *et*

al., 1965): adjacent layers found to be superadiabatic are assumed to exchange heat and moisture to achieve a moist adiabatic lapse rate; momentum is not transported. This cools the lower layer, warms the upper layer and leaves both layers just saturated, excess moisture being rained out. However, while it is reasonable to assume that a rising parcel follows a moist adiabat, the area associated with typical convective activity is much smaller than a climate model's grid size; compensatory subsidence must occur in other parts of the gridbox, warming and drying the air, thus leaving the mean gridbox unsaturated.

Model I incorporates effects of subgrid-scale convection by employing a subgrid variation of temperature, specified as follows: Let T be temperature along a latitude circle at unlimited spatial resolution. Denoting the mean temperature for gridpoint i by T_i and the zonal mean by $[T]$, we define three temperature deviations: 1) over the entire latitude circle, $T^* = T - [T]$, 2) within the gridbox i, $T_i^* = T - T_i$, and 3) the model-resolved deviation, $T_i - [T]$. We define a distribution function $f(T_i^*)$ such that $f(T_i^*)dT^*$ is the probability that a randomly selected unit mass within the gridbox i has a temperature deviation between T_i^* and $T_i^* + dT^*$. We employ a Gaussian form,

$$f(T_i^*) = \frac{1}{\sigma\sqrt{2\pi}} \exp(-T_i^{*2}/2\sigma^2), \tag{14}$$

and obtain σ by extrapolating temperature variance from model-resolved scales.

We assume an inverse power law spectrum for large wavenumbers, i.e.,

$$[T^{*2}] = \sum_{n=1}^{\infty} A(n), \tag{15}$$

where

$$A(n) \simeq A(N)N^{\alpha}/n^{\alpha}, \tag{16}$$

The wavenumber n and N are integers, and α is the slope. This assumption is suggested by the fact that eddy potential energy, which is proportional to T^{*2}, exhibits such a behavior (Charney, 1971). Based on observed potential energy spectra, the large wavenumber requirement is $N > 5$ for the Earth's atmosphere. For a Gaussian distribution of temperature variation within each gridbox

$$[T^{*2}] = \sigma^2 + [(T_i - [T])^2]. \tag{17}$$

Since $(T_i - [T])^2$ is the model-resolved portion of $[T^{*2}]$,

$$\sigma^2 = \sum_{n=1/2I+1}^{\infty} A(n) = \frac{N^{\alpha}A(N)}{(\alpha - 1)(\tfrac{1}{2}I + 1)^{\alpha-1}}, \tag{18}$$

where I (usually 36) is the number of longitude gridpoints. The slope α is obtained by least squares fit to $A(n)$ for $7 \leq n \leq I/2$ using model temperatures on the latitude circle. $N^{\alpha}A(N)$ is taken as the mean of $n^{\alpha}A(n)$ for $7 \leq n \leq I/2$.

Calculation of convection in Model I proceeds as follows. The fraction of the lowest model layer which can rise to layer l is determined by finding the critical temperature deviation, T_l^*, which yields a moist static energy equal to that in layer l, starting with the top layer. This parcel is allowed to rise until it encounters a layer with respect to which it is stable. Rising parcels remain distinct during ascent, with no entrainment. Moist static energy is conserved by the parcels, with precipitation if saturation occurs. After determination of the mass penetrating to all higher layers, mixing with the environment is performed starting at the highest layer and working downward; precipitation reevaporates to the extent that lower layers are unsaturated. The procedure is repeated with the second layer as the source of rising parcels, mixing with the environment, repetition with the third layer as source, etc.

The incentive for using subgrid-scale temperature variance is that it permits convection without the gridbox being unstable in the mean, a realistic characteristic. The intention is to account for variations of moist static energy occurring on scales just smaller than the grid spacing. Horizontal scales of the order of the grid spacing are probably a substantial source of friction affecting the large-scale dynamics (Holton, 1979). Although moist convection occurs on horizontal scales much smaller than the grid spacing, we have not attempted to model details occurring on the convective scale.

Run I–29 omitted subgrid-scale temperature variance, so the gridbox had to be unstable in the mean for convection to occur. This caused moist convection to be less penetrative than in Run I–1; upper levels cooled while lower layers warmed (Fig. 10a). The decreased penetration reduced destruction of kinetic energy by momentum mixing; thus eddy kinetic energy at high levels increased as much as 60% (8σ). The decreased moisture penetration and lowered temperature reduced specific humidity above 400 mb by 20% (20σ). The reduced penetration and change in heating pattern yielded an 8° narrower Hadley cell, consistent with the analysis of Held and Hou (1980). The subgrid variance thus had notable effects, but neither choice yielded clearly more realistic results. For the sake of simplicity and minimization of computing time, we did not include subgrid-scale temperature variance in Model II.

Run I–30 tested the moist adiabatic adjustment scheme. The direct impact of this scheme, as discussed above and shown in Fig. 10b, is to cool the lower atmosphere. However, since it leaves the atmosphere saturated, large-scale precipitation and associated heating increase, leading to a net warming of lower layers (Fig. 10c). This heating distribution intensified the Hadley circulation by 15% (2σ) and

increased total cloud cover by 75% (250σ). These results show both the sensitivity of the climate model to the convection scheme and how feedbacks can alter the immediate impact in a sensitivity experiment.

The cumulus cloud cover C is specified to be proportional to M, the mass of saturated moist air rising through the lower edge of a given layer,

$$C = \gamma M, \tag{19}$$

where γ is taken as 2.5 m^2 s kg^{-1}. This simple specification yields a cumulus cloud cover relatively independent of the number of model layers, with C typically 5–10%; γ was multiplied by 3 for Run I-31 to test its effect. The convective cloud cover increased by about that factor, but total cloud cover increased by only 9% (30σ) because of substantial coincidence with large-scale clouds. Other quantities were not affected much, because of a balancing of solar and thermal radiation effects and the fixed ocean temperature.

The radiative relaxation time of the atmosphere is long compared to the 1 h physics time step in the model. Thus we save computing time by replacing partial cumulus and cloud cover by full cloud cover an appropriate percent of the time for radiative calculations. At each gridpoint and time step a random number between 0 and 1 is generated and compared to the cloud fraction of each layer. Full cloud cover is assigned if the cloud fraction is larger than the random number, or no cloud if it is smaller. Run I-32 verified that no substantial change occurs when the radiative calculations are done separately for the cloud and cloudless fractions of each gridbox.

Horizontal momentum is mixed by moist convection in the model on the simple assumption that exchanged air parcels carry with them the momentum of the layer of origin. After mixing with the environment, this smooths the wind field in the vertical and reduces kinetic energy. Indeed, since the model contains no explicit diffusion, convection and surface friction are the only processes for removal of kinetic energy in the troposphere, and between 40°N and 40°S convection is the larger loss process. In run I-33 the momentum mixing was omitted. This increased eddy kinetic energy at low latitudes by a factor of 3 and weakened the Hadley cell mass flux by 40% (6σ), making the model substantially less realistic than Model I-1. Although the process of momentum mixing by moist convection is not well understood, the simple assumption in Model I-1 seems better than no momentum mixing and was retained in Model II.

Moist convection was not allowed to begin below the condensation level in Model I-1. However, it can be assumed that the lower troposphere has sufficient mechanical turbulence to lift air to the condensation level. Thus the restriction on the level of initiation of moist convection was removed in run I-34. The major effect of the increased convection from low

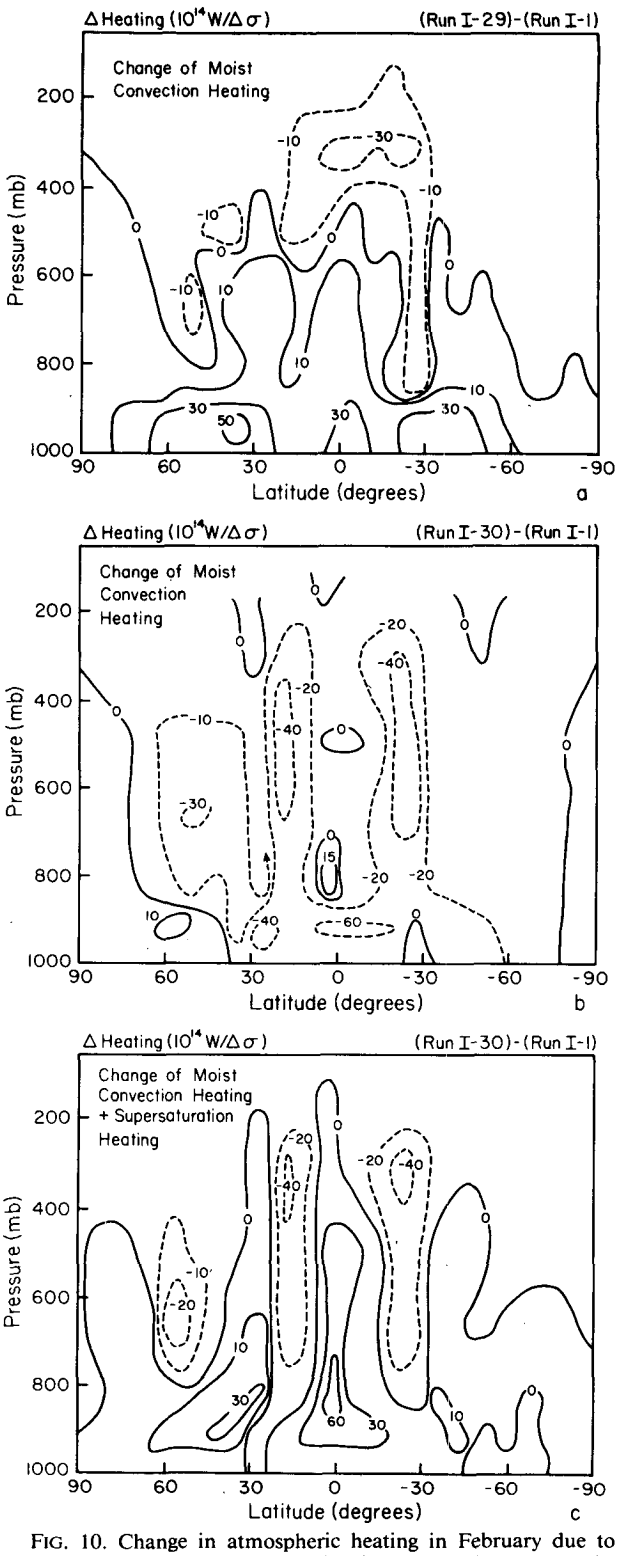

FIG. 10. Change in atmospheric heating in February due to modifications of the moist convection formulation in Model I. Fig. 10a is the change in moist convection heating when the subgrid-scale temperature is eliminated. Figs. 10b and 10c are the change in moist convection heating (10b) and moist convection heating plus supersaturation heating (10c) due to the use of moist adiabatic adjustment instead of the moist convection model in Run I-1.

levels was the introduction of a stronger, more realistic inversion in the zonal mean temperature profile at high latitudes in winter (Stone and Carlson, 1979). Thus the restriction on level of origin of moist convection was omitted in Model II.

The model results depend noticeably on details of the moist convection calculation, such as the level of condensation and evaporation. This is not surprising, since cumulus convection is the dominant vertical transport process at low latitudes. We plan to separately document an extensive set of moist convection sensitivity experiments, which may aid construction of improved models.

f. Large-scale clouds

Large-scale clouds account for about 80% of global cloud cover generated by the model. In both Models I and II the large-scale cloud cover is taken as the saturated fraction of the gridbox under the assumption that the absolute humidity is uniform through the gridbox and temperature has the subgrid-scale variation specified above. Partial spatial cloud cover is replaced by fractional temporal coverage for radiative calculations, as described above for convective clouds. Large-scale precipitation occurs as required to reduce the humidity of a layer to 100%, with evaporation in any lower layer that is unsaturated.

Run I–35 omitted the subgrid temperature variance in the calculation of large-scale cloud cover, assigning full cloud cover when a layer was saturated. This yielded an unrealistically large low-level cloud cover over the oceans, especially in the subtropical summer hemisphere. Since large-scale cloud variations are observed on scales near the gridsize, use of the extrapolated subgrid temperature can be rationalized and was thus retained in Model II.

Run I–36 increased the time step for calculating large-scale precipitation and cloud cover to 5 h (the radiation time step), compared to 1 h (the time step for other physics) in run I–1. This change increased global cloud cover from about 40% to 45%; cloud cover in subpolar latitudes increased from about 60% to 70%. The increase is due to the tendency for more supersaturation to build up in the longer interval between rain-out. Because the increased cloud cover is more realistic and because it is desirable for the radiation to use the computed cloud cover, the 5 h time step is used in Model II.

Run I–37 used the annual mean cloud cover produced by run I–1 to test the effect of computed clouds. The clouds in I–37 varied with latitude, longitude and height, and thus differed from those in I–1 only in the absence of time variability. Significant changes occurred even though the ocean temperature was fixed. For example, in the Aleutian region, which normally has more clouds in winter than in summer, use of annual mean clouds weakened the intensity of the Aleutian low in winter, the effect on sea level pressure (Table 5) exceeded 2σ. This is an example of synoptic scale effects which clouds can have.

Run I–38 tested the effect of specified zonal mean clouds by averaging over longitude and time the clouds produced by run I–1. The major effect was to reduce eddy kinetic energy in the low-latitude troposphere by 25% (5σ). The uniform clouds reduced longitudinal heating differences, leading to a decrease in conversion of available potential energy to kinetic energy. This is an example of global-scale effects which can occur with fixed clouds. The results are consistent with satellite data showing longitudinal variations in radiative flux as great as latitudinal variations (Stephens and Webster, 1977), and with the more extreme fixed-cloud experiment of Shukla and Sud (1981) in which each gridbox had either no clouds or 100% (permanent) clouds.

Runs I–39, I–40 and I–41 tested an aspect of cloud physics, specifically the choice of temperature below which condensation occurs relative to ice rather than to water. In run I–1 condensation was computed relative to ice at all layers if the lowest layer was below 0°C or relative to water if the lowest layer was above 0°C, thus avoiding effects of phase change during descent of precipitation. Runs I–39, I–40 and I–41 used the local layer temperatures to determine phase, with condensation to ice at temperatures below 0, −40 and −65°C, respectively. Condensation is easier relative to ice, i.e., it occurs at a lower vapor pressure. Thus run I–39 has a large amount of high clouds at low latitudes, relative to run I–1 (Fig. 11). Run I–40 introduces a substantial region of supercooling, thus decreasing high clouds relative to run I–39. Run I–41 extends the cloud reduction to high latitudes. We take −40°C as the critical temperature in Model II, the value for homogeneous nucleation (Wallace and Hobbs, 1977). This is used for unseeded conditions; with ice falling into a layer from above, the 0°C criterion is used.

Cloud radiative properties are based on cloud type, altitude and thickness. In Models I and II convective

TABLE 5. Change of cloud cover and sea level pressure in region of Aleutian low (47–63°N, 155°E–135°W) due to use of fixed annual mean clouds (run I–37) instead of computed clouds of run I–1.

Month	Change in cloud cover (%)	Change in sea level pressure (mb)	Standard deviation of sea level pressure (mb)
Jan	−9.2	+5.4	3.2
Feb	−5.4	+12.7	4.2
Mar	−3.9	+8.6	3.8
Apr	+3.4	−7.4	2.0
May	+4.6	+1.0	1.8
Jun	+7.7	+1.3	0.7
Jul	+6.1	+1.8	0.8
Aug	+11.6	−1.5	1.5

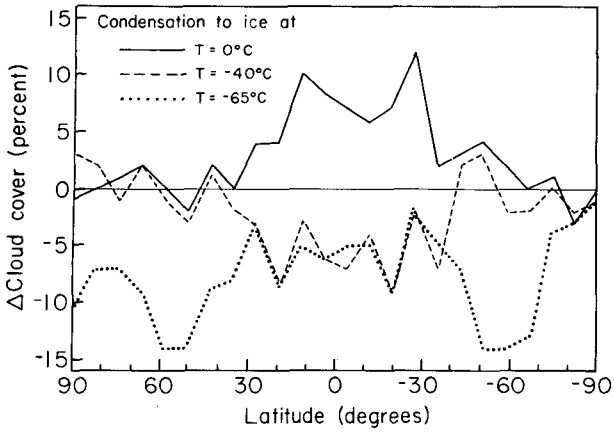

FIG. 11. Change of January cloud cover at 300 mb if condensation to ice occurs at the indicated local temperature. Run I-1 is the control.

clouds have $\tau = 8$ per 100 mb of thickness. This yields realistic albedos with calculations for plane-parallel clouds, similar to that expected for finite clouds of greater optical thickness, a visual albedo ~80% for penetrating cumulus of 500 mb depth and ~50% for shallow cumulus of 100 mb depth. Large-scale clouds in Model I are assigned

$$\tau = 100\left[\frac{p - 100\text{ mb}}{900\text{ mb}}\right]\left[\frac{\min(\Delta p, 100\text{ mb})}{1000\text{ mb}}\right], \quad (20)$$

with no clouds above 100 mb. Here Δp is the pressure thickness of the layer. Thus a low-level cloud 100 mb thick has $\tau \sim 10$, while a cloud in the region 100–400 mb has $\tau \sim 1$–3. These values yield cloud albedos and transmissions in the range of some observations (Haurwitz, 1948; Robinson, 1958).

Data of Platt (1975) indicate that cirrus clouds typically have $\tau \sim 0.25$–0.5. Thus run I-42 used $\tau = \frac{1}{3}$ for large-scale clouds at $T < 258$ K. Run I-43 simplified the τ specification of all large-scale clouds to

$$\left.\begin{aligned} T > 258\text{ K:}&\quad \tau = 0.0133[p\,(\text{mb}) - 100]\\ T < 258\text{ K:}&\quad \tau = \tfrac{1}{3}\end{aligned}\right\}, \quad (21)$$

with no clouds above the $p = 100$ mb level. The main effects of the changes in I-42 and I-43 were reductions by 5–10 W m^{-2} of the annual-mean net radiation gain at the top of the atmosphere and the net energy gain at the ground. Model II-1 used (21), which largely accounted for reducing the annual net energy gain of the ground from 19 W m^{-2} in Model I-1 to 5 W m^{-2} in Model II-1.

Cloud particle phase function and single-scattering albedo, functions of spectral interval, are based on Mie computations for particles with effective radius 10 μm for water clouds (Squires, 1958) and 25 μm for ice clouds (Hansen and Pollack, 1970). Absorption of radiation by cloud particles and by water vapor internal to the cloud is thus realistically included. Also the cloud radiative properties have realistic wavelength dependence.

g. Ground physics

1) GROUND TEMPERATURE

Diurnal variations of ground temperature are important because of the highly nonlinear dependence of latent and sensible heat fluxes on temperature. Seasonal storage and release of heat can amount to several watts per square meter and significantly influence ground temperature (Taylor, 1976).

The basic problem is to solve the one-dimensional heat conduction equation

$$\frac{\partial T}{\partial t} = \frac{\lambda}{c_g}\frac{\partial^2 T}{\partial z^2} = K_g\frac{\partial^2 T}{\partial z^2}, \quad (22)$$

where c_g is the heat capacity per unit volume, λ the thermal conductivity and K_g the thermal diffusivity, subject to the heat flux at the upper boundary

$$F(0) = F_{sw} - F_{lw} - F_h - F_q + F_p. \quad (23)$$

Here F_{sw} is the absorbed solar radiation, F_{lw} the net thermal radiation, F_h and F_q the sensible and latent heat fluxes, and F_p the heat flux carried by precipitation.

We use a small number of ground layers, solving for the mean temperature of each layer. The upper layer should be thin enough to simulate diurnal surface temperature change, but thick enough to allow long time steps. At least one deep lower layer is also needed for seasonal heat storage. We assume that the heat capacity and conductivity are uniform in each layer, the temperature in each layer is a quadratic function of depth, and no heat crosses the lower edge of the bottom layer. The resulting two-layer equations are

$$z_1 c_1\frac{d\bar{T}_1}{dt} = F(0) - F(-z_1), \quad (24)$$

$$z_2 c_2\frac{d\bar{T}_2}{dt} = F(-z_1), \quad (25)$$

where the heat flux crossing the interface between the two layers is

$$F(-z_1) = \frac{3\bar{T}_1 - 3\bar{T}_2 - (1/2)F(0)z_1/\lambda_1}{z_1/\lambda_1 + z_2/\lambda_2}. \quad (26)$$

We use a similar formulation for ocean ice with the boundary condition

$$T(-z_1 - z_2) = T_{fo}, \quad (27)$$

where T_{fo}, the freezing point for ocean, is 271.6 K. The heat flux at $z = -z_1$ is

$$F(-z_1) = \frac{12\bar{T}_1 - 18\bar{T}_2 + 6T_{fo} - 2F(0)z_1/\lambda_1}{4z_1/\lambda_1 + 3z_2/\lambda_2}. \quad (28)$$

The heat flux at the ice-ocean interface is

$$F(-z_1 - z_2) = 3\lambda_2 \frac{\bar{T}_2 - T_{fo}}{z_2} - \tfrac{1}{2}F(-z_1). \quad (29)$$

Resulting equations for the two-layer ocean ice model are

$$z_1 c_1 \frac{d\bar{T}_1}{dt} = F(0) - F(-z_1), \quad (30)$$

$$z_2 c_2 \frac{d\bar{T}_2}{dt} = F(-z_1) - F(-z_1 - z_2). \quad (31)$$

Equations for a three-layer model were determined in a similar way. Layer thicknesses are based on comparison with an accurate 21-layer solution for the case $K_g = 4 \times 10^{-7}$ m^2 s^{-1} with no atmosphere. z_1 was picked to minimize the rms error in the diurnal amplitude of T_1, and z_2 was used to minimize the error in annual amplitude of daily mean T_1. The third parameter in the 3-layer model was used to reduce the diurnal phase error in T_1. Optimum depths are $z_1 \sim 10$ cm, $z_2 \sim 4$ m for two layers, and $z_1 \sim 5$ cm, $z_2 \sim 25$ cm, $z_3 \sim 4$ m for three layers. These depths scale as $(K_g)^{1/2}$. Note that 10 cm and 4 m are approximately the $1/e$ damping depths for the diurnal and annual thermal waves (Sellers, 1965). The accuracy of the 2-layer and 3-layer models is examined in Fig. 12.

Model I uses 2 layers with a dry ground heat capacity of 1.13×10^6 J m^{-3} K^{-1} and thermal conductivity of 0.42 W m^{-1} K^{-1}. Snowfall modifies the conductivity as

$$z_1/\lambda_1 = z_s/\lambda_s + z_g/\lambda_g, \quad (32)$$

where z_s is the snow thickness (four times the water-equivalent thickness), z_g (10 cm) the thickness of the upper layer of earth, and λ_s (0.35 W m^{-1} K^{-1}) the thermal conductivity of snow. The conductivity and heat capacity vary with snow cover, ground moisture and moisture phase in Models I and II, but do not depend on vegetation in Model I. Changes in temperature and thermal properties conserve energy.

The lower ground layer in Run I-1 tended to be too cold at 50–60°N in winter and to stay frozen in summer even though the upper layer was warmer than observed (Chang, 1958). Thus we tested two possible improvements in runs I-44 and I-45. Snow depth was increased to 10 times the water equivalent depth in I-44, a value typical of new snow and appropriate for the mean age of 1–2 days of the top layer of snow in the model. This provided better insulation of the ground, increasing high-latitude ground temperatures a few degrees in winter. In I-45 the thermal conductivity was increased to ~3 W m^{-1} K^{-1} in deserts (Sellers, 1965), but decreased by a factor of 4 in vegetated areas at 30–90°N during October–March (April–September at 30–90°S) to simulate the effect of dead grass and leaves. This decreased the summer temperature difference between the first and second layers from 25°C to a more realistic 10–15°C at 50–60°N. The changes tested in I-44 and I-45 were included in Model II. As a result, permafrost is generally confined to latitudes poleward of 60° in Model II.

2) GROUND MOISTURE

We use a two-layer model, the water content of the upper layer responding immediately to evaporation and precipitation and the lower layer acting as a reservoir. The rate of change of moisture in the upper layer is

$$\frac{\partial W_1}{\partial t} = \frac{P_r - E - R}{f_1} + \frac{W_2 - W_1}{\tau}, \quad (33)$$

where the wetness of the ith layer, W_i, is the ratio of available water to field capacity (available water at saturation). P_r, E and R are the rainfall, evaporation and run-off rates, and τ the time constant for diffusion of moisture between layers. The wetness of lower layer is given by

$$\frac{\partial W_2}{\partial t} = \frac{f_1}{f_2}\frac{W_1 - W_2}{\tau}. \quad (34)$$

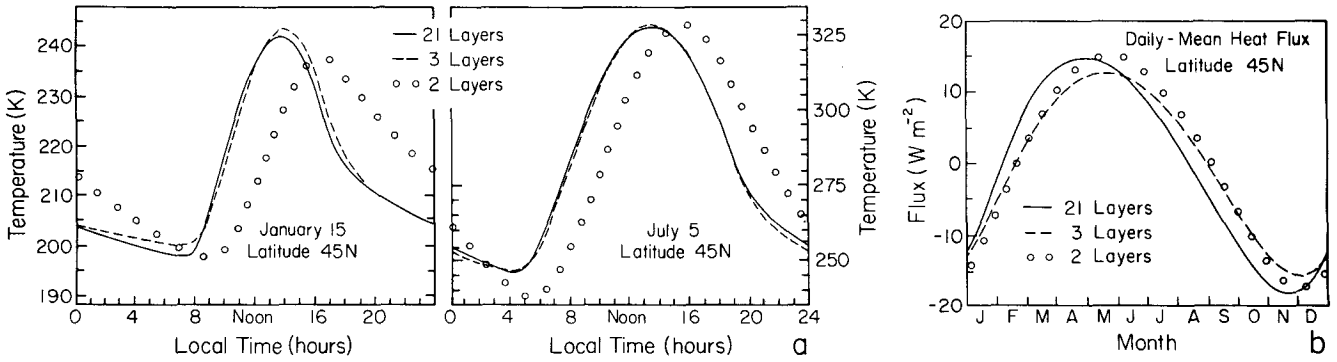

FIG. 12. Diurnal surface temperature variation (a) and diurnal-mean heat flux into the ground (b) for the case of no atmosphere ($F_h = F_q = F_p = 0$) and thermal diffusivity $K_g = 4 \times 10^{-7}$ m^2 s^{-1}.

In run I–1 the diffusion time constant is independent of direction.

Field capacity depends on soil type and vegetation (Sellers, 1965; Strahler, 1969). Available depth in deserts is typically ~20 cm and water holding capacity 5–10% of soil volume. Typical values in vegetated areas are 50–100 cm and 20–25%. Also, rainforests have 10–20 cm of water stored in surface biomass. We let the upper layer be 10 cm to coincide with ground temperature calculations. In Model I–1 f_1 = 6 mm, f_2 = 3 cm for desert, f_1 = 6 cm, f_2 = 30 cm for rainforest, and f_1 = 2.4 cm, f_2 = 12 cm for other land areas, with the global distribution of surface types from Plate 4 of Strahler (1969). Thus in Model I–1 the field capacities (Fig. 13) are independent of season. The diffusion time constant is τ = 2 days in Model I–1, based on the relationship $\tau \sim d^2/D$, depth of diffusion d = 10 cm, and diffusivities D = 1 to 10^4 cm^2 day^{-1} (Hillel, 1971).

Evaporation is computed as the product

$$E = \beta E_p, \tag{35}$$

where E_p is the potential evaporation of a wet surface ($2h$) and β is an efficiency factor. β should depend on ground wetness, soil type and plant wilting point (Baier *et al.*, 1972; Hillel, 1971), and be an appropriate gridbox mean. We take

$$\beta = W_1. \tag{36}$$

Run-off should depend on ground wetness, precipitation rate, soil type and vegetation, and also be an appropriate mean for the gridbox. In Model I–1

$$R = W_1 P_r. \tag{37}$$

with additional run-off when necessary to keep $W_1 \leqslant 1$. Note that (36) and (37) are consistent with the fraction W_1 of the gridbox being saturated, $1 - W_1$ being dry and the precipitation divided between these parts of the gridbox in proportion to area. All ground hydrology calculations conserve water and energy, except run-off which disappears, in effect becoming part of the (infinite) ocean.

In Model I–1 continental areas are too hot and dry in summer, which could be due to low evaporative cooling and thus to the hydrological formulation. Runs I–46 through I–49 were aimed at evaluating model sensitivity to hydrology. Run I–8 is the primary control, because Run I–1 is too cold in mid-latitudes during winter and early spring, which thus tends to keep groundwater unrealistically frozen in spring. Run I–8, with increased eddy energy, has realistic winter and spring temperatures, and thus fully exposes the problem of early groundwater loss.

Runs I–46 and I–47 tested effects of vegetation on evaporation. Run I–46 used field capacities based on vegetation type (Table 6) for the global vegetation distribution of Matthews (1983). This yielded larger field capacities (Fig. 13), which increased the amplitude of seasonal water storage but hardly affected the phase (Fig. 14a). I–47 let water in both layers 1 and 2 be instantly available for evaporation in vegetated areas during the growing season, by defining the upward diffusion coefficient as infinite. Outside the growing season (defined as May–August at 30–90°N, November–February at 30–90°S and all year elsewhere) upward diffusion was zero. Deserts were assumed to have no plants and thus no upward diffusion from the lower layer. The downward diffusion time constant was decreased from 2 days to 1 day. These changes delayed loss of groundwater about 2 months (Fig. 14a). The large effects indicate the importance and difficulty of realistically including vegetation effects in the hydrology; e.g., the depth to which water can be extracted probably increases during the growing season. In the absence of a more realistic hydrology we included the changes tested in I–46 and I–47 in Model II.

Runs I–48 and I–49 tested the run-off scheme, with I–47 as control. I–48 had no run-off except when the upper ground layer was saturated. The result was a global annual mean run-off of 18 cm year^{-1}, compared to estimated actual run-off of 29 cm year^{-1} (L'vovich, 1980); also the continents were too cold and wet in summer. I–47, with run-off specified by (37), had run-off of 31 cm year^{-1} but summer continental temperatures about 5°C too warm. I–49 used an intermediate run-off

$$R = \tfrac{1}{2} W_1 P_r, \tag{38}$$

which yielded 24 cm year^{-1} global run-off and summer continental temperatures about 2–3°C cooler than observed. This intermediate run-off is used in Model II, primarily for its effect on summer temperatures. The run-off specification altered the amplitude but not the phase of seasonal water storage (Fig. 14b).

3) SNOW AND ICE

Snow depth is computed as the balance of snowfall, melting and sublimation. When the first layer air temperature is <0°C, precipitation falls as snow. If the upper layer ground temperature T_g is ≤0°C, the snow depth increases; otherwise the snow melts, decreasing T_g. Net heating of a snow surface raises T_g as high as 0°C; additional heat causes snow melting. Snowmelt goes into run-off or ground moisture with the same prescription as for rainfall.

The albedo of snow-covered ground in the model depends on snow depth and age, vegetation cover, and the albedo of underlying ground:

$$A = A_g + (A_s - A_g)[1 - \exp(-d_s/d_s^*)], \tag{39}$$

where A_g is the snow-free ground albedo, A_s the snow albedo for infinite depth, and d_s and d_s^* are the snow depth and masking depth in equivalent thickness of

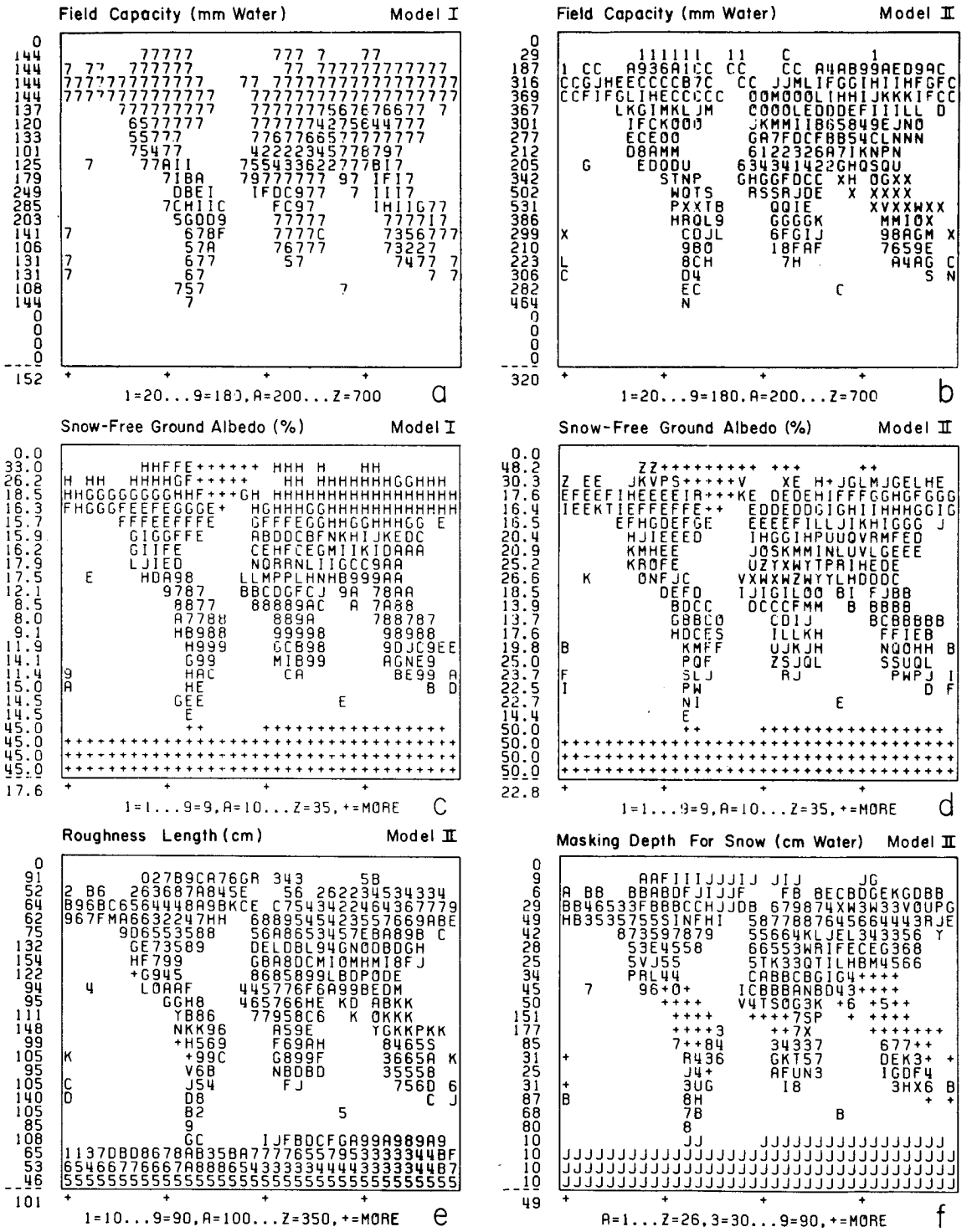

FIG. 13. Geographical distribution of (a) total field capacity, (b) roughness length, (c) snow-free ground albedo and (d) masking depth for snow. Model I is on the left and Model II on the right. The masking depth for Model I was 5 cm water everywhere except over ice, where it was 1 cm water.

liquid water. In Model I–1 we use $d_s^* = 50$ cm for vegetated areas and $d_s^* = 1$ cm otherwise, to roughly account for small-scale surface irregularities and non-uniform snow accumulation over the gridbox. A_s is a function of snow age

$$A_s = 0.5 + 0.35 \exp(-a_s/5), \qquad (40)$$

where a_s is the age of the upper snow layer in days,

TABLE 6. Vegetation characteristics in Model II.

		Desert*	Tundra	Grass	Shrub	Woodland	Deciduous	Evergreen	Rainforest
Visual albedo	Winter	0.35	0.07	0.09	0.09	0.08	0.10	0.07	0.06
	Spring	0.35	0.06	0.10	0.10	0.07	0.05	0.07	0.06
	Summer	0.35	0.08	0.09	0.14	0.08	0.06	0.08	0.06
	Autumn	0.35	0.08	0.09	0.11	0.06	0.05	0.06	0.06
Near-IR albedo	Winter	0.35	0.20	0.27	0.27	0.23	0.30	0.20	0.18
	Spring	0.35	0.21	0.35	0.30	0.24	0.22	0.20	0.18
	Summer	0.35	0.30	0.36	0.42	0.30	0.29	0.25	0.18
	Autumn	0.35	0.25	0.31	0.33	0.20	0.22	0.18	0.18
Field capacity ($g\ m^{-1}$)	Layer 1	10	30	30	30	30	30	30	200
	Layer 2	10	200	200	300	300	450	450	450
Masking depth (m)		0.1	0.2	0.2	0.5	2	5	10	25
Roughness length (m)		0.005	0.01	0.01	0.018	0.32	1	1	2

* Desert albedo is reduced by ground wetness by the factor $(1 - 0.5\ W_1)$.

computed from

$$a_s(t + \Delta t) = \{a_s(t) + [1 - a_s(t)/a_\infty]\Delta t\} \exp(-\Delta d_s/d_c). \quad (41)$$

Here Δd_s is the snowfall in time Δt; d_c, taken as 0.2 cm, is the depth required to refresh the snow albedo; and a_∞ is an old age limit taken as 50 days. Thus fresh snow has an albedo 0.85 and old snow 0.50, similar to some measurements (U.S. Army Corps of Engineers, 1956).

The snow-free albedo of ocean ice and land ice in Model I is 0.45 (Posey and Clapp, 1964) independent of wavelength. Ocean ice albedo in Model II is 0.55 in the visible (defined as 60% of solar irradiance, corresponding to wavelengths < 0.7 μm) and 0.3 in the near infrared, leading to a spectrally weighted ocean ice albedo of 0.45. Land-ice albedo in Model II is the same as for aged snow: 0.6 in the visible, 0.35 in the near IR and 0.5 spectrally weighted.

Snow which falls on ocean ice accumulates as snow until the snow depth reaches 10 cm (equivalent water). At that time 1 cm of it is added to the lower layer as ice, thus keeping the upper layer thin enough to simulate diurnal temperature change.

The surface albedo produced by Model I–1 was too large in some snow-covered areas, e.g., reaching 60–70% in forested parts of southern Canada and Siberia where observations suggest 35–55% (Kukla and Robinson, personal communication, 1981). The high values were possible because of the small masking depths in Model I–1. In run I–50 realistic masking depths (Fig. 13) were assigned for each of eight vegetation types (Table 6). The resulting surface albedos are generally within the range suggested by observations. This change is included in Model II.

Run I–51 tested the vegetation albedos of Table

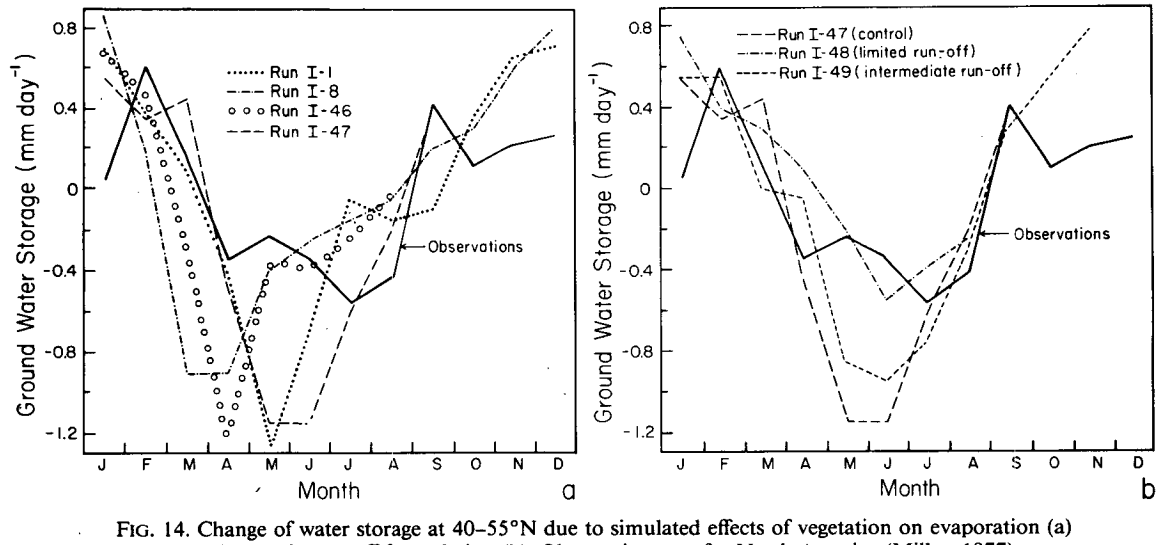

FIG. 14. Change of water storage at 40–55°N due to simulated effects of vegetation on evaporation (a) and changes in run-off formulation (b). Observations are for North America (Miller, 1977).

6 and Fig. 13, including seasonal variations and separate albedos for the visible and near IR. The main effect was higher summer surface albedo, as much as 0.10 higher in the subtropics. The planetary albedo increased as much as 0.03 over land in the subtropics. The seasonal and spectral albedo variations are included in Model II.

Ocean ice thickness is specified in Model I-1 to vary linearly from 1 m at the edge of the ice to 5 m at the pole. Fractional open water in Model I-1 is based on a climatological data set, but additionally restricted by

$$f_0 \geq 0.1/z_{\text{ice}}, \tag{42}$$

where z_{ice} is the ice thickness in meters. The minimum for f_0 in (42) is intended to represent leads. These values for z_{ice} and f_0 are representative of current conditions (Orvig, 1970).

Run I-52 tested minor changes of the ocean ice. The monthly ice coverage of Alexander and Mobley (1974) was replaced in the northern hemisphere by data of Walsh and Johnson (1979) for mean 1953-77 conditions, the main change being a decrease of winter ice around the Eurasian continent. The ice thickness was calculated from the fractional ice coverage $(1 - f_0)$ as

$$z_{\text{ice}}\,(\text{m}) = 1 + (1 - f_0)z_{\max}. \tag{43}$$

Here $z_{\max}$ is $n^{1/2}$, where n is the number of months with at least some ice in the gridbox, except $z_{\max} = 4$ if $n = 12$. The primary effect of these changes was an increase of sensible and latent heat fluxes into the atmosphere at the gridboxes with reduced sea ice, and an increase of surface air temperature at those points by as much as 5 K (2σ) in winter. These changes are included in Model II, because they represent a smoother more realistic month-to-month variation in ice cover.

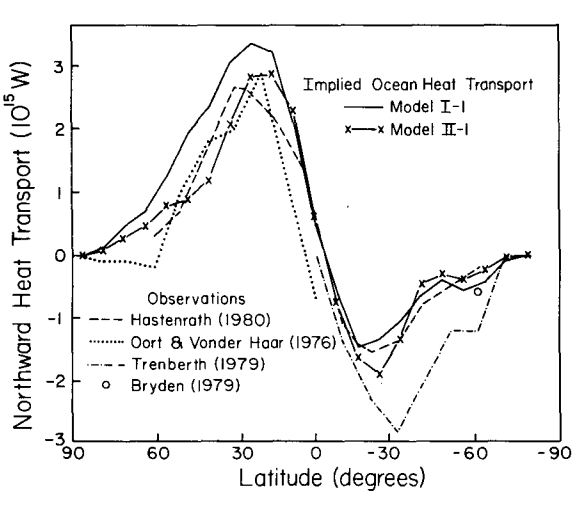

FIG. 15. Implied annual ocean heat transport in Models I and II, and observed values.

4) OCEAN

The ocean surface has specified seasonally varying temperature in Run I-1. Thus the ocean is a potentially unlimited source or sink of heat and water vapor, and the degree to which fluxes from the ocean are consistent with observed data provides a good model test. The implied meridional ocean heat transport, required for the ocean temperature to be the same each year, is shown in Fig. 15. Model I-1 requires large northward transport of energy by the ocean, a symptom of the cold winter atmosphere which draws excessive energy from the ocean. The implied transport in Model II-1 is consistent with observations, though data in the Southern Hemisphere are especially uncertain. The improvement in Model II is due to the more realistic atmospheric transports (Section 3).

Run I-53 tested the fractional grid, by assigning each gridbox to be 100% water or 100% land. Some substantial water bodies, e.g., the Great Lakes, and islands thus disappeared. Ocean points were still divided fractionally into ice and open water. The primary effect was to increase the continentality of interior land areas. Temperature changes as great as 5 K (2σ) occurred, due to decreased latent heat fluxes. The Tibetan low and the heat low in the United States Southwest deepened by 5-10 mb. Most continental interiors were drier, while increased rain fell on the windward side of elevated coasts. On sum, the fractional grid was more realistic and was thus retained for Model II-1.

Run I-54 used the ocean data set of Robinson and Bauer (1981) for sea surface temperature, in place of the data of Alexander and Mobley (1974). No major impact on the atmosphere occurred. The Robinson and Bauer data are used in Model II.

h. Surface air

We compute the fluxes of momentum, heat and water vapor from the ground into the lowest model layer using a drag law parameterization (Deardorff, 1967):

$$\left.\begin{aligned} \boldsymbol{\tau} &= -\rho C_D V_s \mathbf{V}_s \\ F_h &= c_p \rho C_h V_s (T_g - T_s) \\ F_q &= \beta \rho C_q V_s (q_g - q_s) \end{aligned}\right\}, \tag{44}$$

where the subscripts s and g stand for surface air and ground. We assume that

$$C_h = C_q, \tag{45}$$

where C_h and C_q are the heat and humidity transfer coefficients. We express the drag coefficient as the product (Businger *et al.*, 1971)

$$C_D = C_{DN} D_M, \tag{46}$$

where C_{DN}, the drag coefficient for neutral stability, is

$$C_{DN} = \frac{k^2}{\ln^2(z_s/z_0)} \tag{47}$$

over land, with the von Kármán constant $k = 0.35$; z_0 is the surface roughness and z_s the height of the surface layer. Over the ocean we take (Garratt, 1977)

$$C_{DN} = 10^{-3}[0.75 + 0.067V_s\,(\text{m s}^{-1})]. \tag{48}$$

D_M, which gives the variation of drag coefficient in conditions of non-neutral stability, and the analogous C_h/C_D are obtained from the Monin-Obukhov similarity relations (Deardorff, 1968) via analytic approximations

$$\left.\begin{aligned} D_M &= C_D/C_{DN} \\ &= \left[\frac{(1 - a\,\text{Ri}_s)(1 - b\,\text{Ri}_s)}{1 - c\,\text{Ri}_s}\right]^{1/2} \\ C_h/C_D &= 1.35\left[\frac{(1 - d\,\text{Ri}_s)}{(1 - f\,\text{Ri}_s)}\right]^{1/2} \end{aligned}\right\} \tag{49}$$

for the unstable case ($\text{Ri}_s < 0$), and

$$\left.\begin{aligned} D_M &= C_D/C_{DN} \\ &= [1 + (11.2 + 90\,\text{Ri}_s)\,\text{Ri}_s]^{-1} \\ C_h/C_D &= 1.35/(1 + 1.93\,\text{Ri}_s) \end{aligned}\right\} \tag{50}$$

for the stable case ($\text{Ri}_s > 0$). The coefficients in (49) are given in Table 7; Ri_s is the bulk Richardson number for the surface layer, i.e.,

$$\text{Ri}_s = \frac{z_s g(T_s - T_g)}{T_g V_s^2}. \tag{51}$$

These parameterizations depend on V_s, T_s and q_s explicitly and through C_{DN} and Ri_s. V_s is obtained in Model I-1 by linear extrapolation in σ of the u and v wind components in the two lowest model layers. T_s and q_s are obtained from empirical relations for the fluxes from the surface layer into the first layer

$$\left.\begin{aligned} F_h &= c_p\rho K\left(\frac{T_1 - T_s}{z_1 - z_s}\right) \\ F_q &= \rho K\left(\frac{q_1 - q_s}{z_1 - z_s}\right) \end{aligned}\right\}, \tag{52}$$

where T_1 is the potential temperature of the first layer relative to the surface pressure and K is an empirical eddy diffusion coefficient (Deardorff, 1967):

$$\left.\begin{aligned} K &= \frac{60 - 1.156 \times 10^7 \Delta T/\Delta z}{1 - 1.752 \times 10^4 \Delta T/\Delta z}, && \frac{\Delta T}{\Delta z} < 0 \\ K &= \frac{60}{1 + 50\,\text{Ri}_1}, && \frac{\Delta T}{\Delta z} > 0 \\ \text{Ri}_1 &= \frac{g\Delta T \Delta z}{T_1[(\Delta u)^2 + (\Delta v)^2]} \end{aligned}\right\}. \tag{53}$$

TABLE 7. Coefficients for Eq. (49) as a function of $\log_{10}(z_s/z_0)$.

$\log_{10}(z_s/z_0)$	a	b	c	d	f
1	16.60	3.25	5.11	1.24	0.13
2	10.40	8.45×10^{-1}	1.68	0.81	0.14
3	5.24	1.83×10^{-1}	0.56	0.66	0.24
4	3.13	4.62×10^{-2}	0.33	0.80	0.44
5	2.32	1.25×10^{-2}	0.30	0.99	0.66
6	1.98	3.20×10^{-3}	0.33	1.18	0.87
7	1.83	7.28×10^{-4}	0.39	1.35	1.05
8	1.76	1.47×10^{-4}	0.45	1.50	1.22
9	1.71	2.71×10^{-5}	0.51	1.65	1.37
10	1.69	4.60×10^{-6}	0.56	1.78	1.52

Here Δ indicates a difference between the surface and first layer, e.g., $\Delta T = T_1 - T_s$; K was obtained from measurements near the top of the planetary boundary layer, and thus may be most appropriate if the lowest model layer is about as thick as the boundary layer; and T_s and q_s follow by assuming the surface layer is in equilibrium, i.e., by equating the fluxes from the ground to those into the first layer, e.g.,

$$c_p\rho C_h V_s(T_s - T_g) = c_p\rho K\frac{(T_1 - T_s)}{z_1 - z_s}. \tag{54}$$

1) Surface roughness

Effective surface roughness depends on both large-scale topography and small-scale surface texture. Fiedler and Panofsky (1972) measured turbulence at 75 and 225 m to obtain the effective roughness for several terrain types, shown in Fig. 16 as a function of σ, the standard deviation of large-scale surface topography. We define σ on a $1° \times 1°$ grid area using the topography of Gates and Nelson (1975) to compute σ from the nine altitudes of the surrounding $3° \times 3°$ area. For land areas we use the analytic fit (Fig. 16),

$$z_0\,(\text{m}) = 0.041\sigma^{0.71}, \tag{55}$$

to estimate z_0. The result is then taken as the maximum of this and the local vegetation z_0, the latter based on Garratt (1977) for Model I-1; the lower limit on z_0 due to vegetation is effective mainly in rainforest areas of South America and Africa. The effective log z_0 for each gridbox is obtained as the average of log z_0 for each $1° \times 1°$ area in the gridbox. For sea-ice we use (Doronin, 1969)

$$z_0\,(\text{m}) = 0.43 \times 10^{-3}, \tag{56}$$

and for ocean (Garratt, 1977)

$$z_0\,(\text{m}) = 7.48 \times 10^{-7}V_s^{2.46}, \tag{57}$$

where V_s is in m s^{-1}.

In Run I-55 the vegetation z_0 was based on the global vegetation file of Matthews (1982), rather than on Garratt (1977). This caused some moderate in-

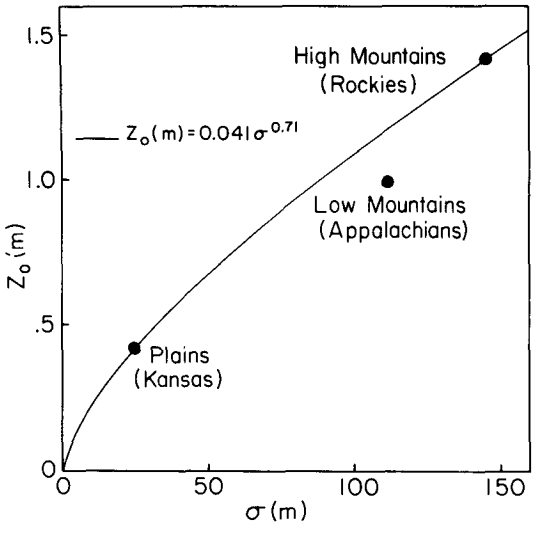

FIG. 16. Effective roughness versus standard deviation of topography.

creases in z_0 and thus in the neutral drag coefficient, but no substantial change in atmospheric circulation. The modified vegetation roughness is consistent with estimates of Baumgartner *et al.* (1977), and explicit dependence of z_0 on vegetation type permits a useful model feedback; thus it is included in Model II. Fig. 13 shows z_0 for Model II-1 at 8° × 10° resolution.

We specify z_s as 10 m over ocean or sea ice and 30 m over land in Models I and II. Run I-56 employed z_s = 30 m everywhere. This decreased the neutral drag coefficient over oceans and warmed the surface air over the oceans by 1-2°C indicating that the climate in the model is not sensitively dependent on z_s.

2) SURFACE WIND

Model I specifies V_s by linear extrapolation from the lowest model layers, which does not depict the spiral (Ekman) turning of the wind in the boundary layer. Thus we tested the modified Ekman formulation of Taylor (1916), which includes a spiral layer above a surface layer, with continuity of the wind direction and eddy stress across the interface between these layers. With these conditions and the x axis along the isobars, the surface wind is

$$u_s = V_g + \sqrt{2}V_g \sin\alpha_0 \cos(\alpha_0 + 3\pi/4), \quad (58)$$

$$v_s = \sqrt{2}V_g \sin\alpha_0 \sin(\alpha_0 + 3\pi/4), \quad (59)$$

where V_g is the geostrophic wind and α_0 the cross-isobar angle in the surface layer.

In run I-57 α_0 was fixed as a function of latitude based on observations (Haltiner and Martin, 1957, p. 235). This decreased surface wind speeds ~15% and reduced destruction of eddy kinetic energy by surface friction 50% (5σ), due to the decreased wind and drag coefficient. At middle and high latitudes, where surface friction is the major loss mechanism, eddy kinetic energy increased by a factor of 2 in winter. The increase was smaller in summer and at low latitudes, where destruction of kinetic energy by moist convection increased. Eddy energy increased on all scales (Fig. 17). Northward transport of energy by eddies increased; the peak value in winter by a factor of 2. Temperatures warmed as much as 15 K (6σ) north of 50°N in winter. The increased turning of the wind in the lowest layers, and thus convergence in low pressure regions, sharpened the ITCZ and strengthened the Hadley cell 27% (4σ).

The cross-isobar angle α_0 should actually be interactive with the surface friction, i.e., the model should compute α_0 such that the surface friction and surface wind are consistent. The requirement that the shear stress be continuous between the spiral layer and surface layer yields the relationship

$$\tau = \rho V_g \sin\alpha_0 \sqrt{2fK}, \quad (60)$$

which specifies α_0, given the geostrophic wind V_g and eddy diffusion coefficient K. Runs I-58, I-59 and I-60 used this formulation with different choices for V_g: the wind in layer 1 (run I-58); the wind at the top of the boundary layer, i.e., in the layer just above the height to which dry convection mixed at the previous time step (run I-59); the actual geostrophic wind at this height, computed from the pressure gradient force (run I-60). In each case the α_0 used in (60) was its mass-weighted value for the intervening layers. T_s and V_s were solved simultaneously by iteration, thus avoiding oscillations in their values and providing consistent drag and eddy diffusion coefficients. The choice of V_g in I-59 is used for Model II,

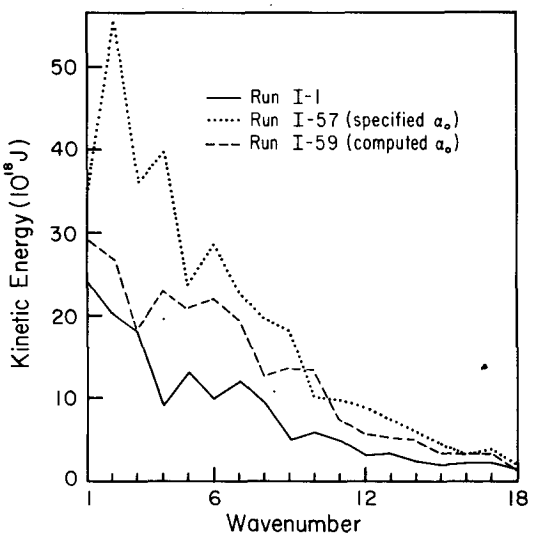

FIG. 17. Kinetic energy of the Northern Hemisphere troposphere in January.

because the formulation (60) relates the surface wind to the wind above the layer of frictional influence, and use of the actual geostrophic wind (I–60) made little difference. Fig. 18 shows the diurnal variation of the height of frictional influence in the model, as defined by dry convection, for several regions. Models I and II are similar in this regard. The model and observations have peak boundary layer height in late afternoon over land areas.

Runs I–58, I–59 and I–60 all produce kinetic energy ~50% greater than in run I–1, with the largest increase in synoptic scales (Fig. 17). Eddy energy is not as great as in I–57, which had smaller surface drag. Apparently baroclinic waves of short vertical wavelength, generated in the low troposphere, are damped by the surface friction formulation of run I–1. Winter temperatures at high latitudes are as much as 10 K warmer than in run I–1, and northward transports of energy are greater by about a factor of 3 at low levels. The large effects on the Hadley circulation and ITCZ noted in run I–57 did not occur, probably because the cross-isobar angles produced at low latitudes are much smaller than observed (Fig. 19).

The inability of surface drag to produce the large observed turning of the wind at low latitudes is a well known difficulty in the Ekman formulation. One solution is to take into account baroclinic advection within the boundary layer, in effect correcting for altitude variation of K not included in the Ekman formulation. Clarke and Hess (1975) proposed such a correction for α_0, based on use of the thermal wind to estimate advection. This correction was applied in run I–61, with run I–58 as control. The resulting

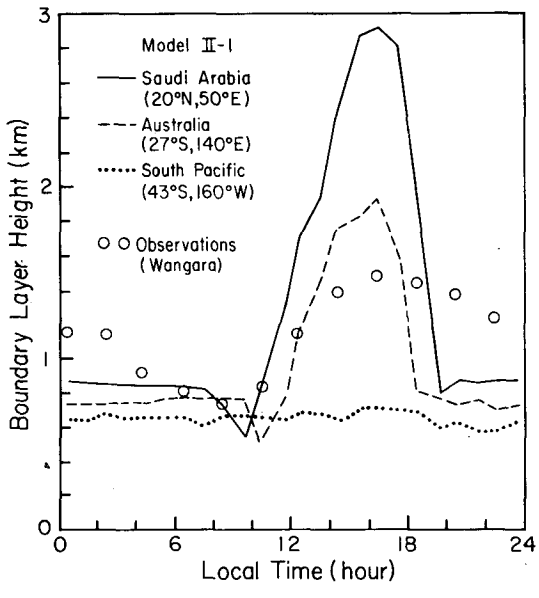

FIG. 18. Diurnal variation of boundary layer height computed in the model (Run II–1) for August and observed during days 33–35 (August) of the Wangara experiment in Australia (Clarke *et al.*, 1971).

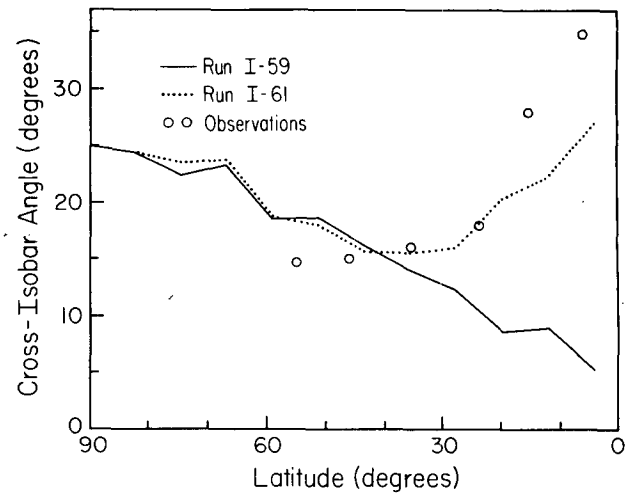

FIG. 19. Cross-isobar angle in the Northern Hemisphere during January. Observations are from Gordon (1952).

cross-isobar angle was in much better agreement with observations (Fig. 19). The primary effect on the model climate was intensification of the ITCZ, with narrowed regions of precipitation. Rainfall in the southern Sahara decreased 50% (2σ). The Hadley cell mass flux increased 40% in July. These changes are similar to those in run I–57 which specified α_0. The modified Ekman formulation of run I–61 was adopted for Model II.

The changes of model physics incorporated to produce Model II from Model I are summarized in Table 8. Simulations with both models are presented below.

3. Model simulations

Climate simulations obtained by five-year runs of Models I and II at 8° × 10° resolution are compared here with observations; additional 8° × 10° results are given in Section 4 in comparison with 4° × 5° and 12° × 15° runs. Most of the Southern Hemisphere observations were added to our graphs after Model II was selected. Thus the Southern Hemisphere provides an essentially independent model test, though observations are less accurate there.

a. Temperature

1) ZONAL MEAN

The zonal mean temperature in Model II agrees well with observations (Fig. 20). The tropospheric temperature in winter poleward of 30° latitude is generally 5–10 K warmer in Model II than in Model I. This warming was caused by the Ekman formulation for computing the surface wind (I–58) which led to increased poleward transport of energy.

The vertical temperature profile also improved in Model II, the main changes being the introduction of a realistic tropopause at all latitudes and a realistic

TABLE 8. Changes of model physics from Model I to Model II.

Test run	Physics change	Major effect
I–6	Coriolis/metric terms at pole	Strengthened polar cell
I–10	Drag in top model layer	Reduced stratospheric winds; realistic tropopause at high latitudes
I–13, 14	9 layers in vertical	Improved definition of jet stream and tropopause; more longwave generation
I–24	1 k-distribution for each gas	Faster computation; higher accuracy
I–25	Realistic surface emissivities	No large effect
I–29	No subgrid-scale temperature variation for moist convection	Increased EKE; reduced upper level humidity and temperature; narrowed Hadley cell
I–34	Moist convection can start below condensation level	Stronger high-latitude winter temperature inversion at low levels
I–36	Large-scale rain every 5 h	Increased large-scale cloud cover
I–40	Local $T = -40°C$ for saturation over ice	Less cirrus clouds at low latitudes
I–42, 43	Cloud optical thickness modified	Reduced net heat into ground
I–44	Snow density decreased	Warmer ground in winter
I–45	Ground thermal conductivity changed	Reduced vertical temperature gradient in ground
I–46, 47, 49	Altered hydrology based on vegetation; intermediate run-off formulation	Early summer moisture increased and temperature decreased
I–50	Realistic vegetation masking depths	Reduced albedo in snow-covered areas
I–51	Ground albedo based on vegetation	Small albedo increase in subtropics
I–52	Modified ocean ice coverage	Local effects on T and evaporation
I–54	Modified ocean temperatures	No large effect
I–55	New lower limit for surface roughness	No large effect
I–59	Ekman surface wind formulation	Increased EKE and eddy transports
I–61	Modified cross-isobar angle	Sharpened ITCZ

inversion at high latitudes in winter. The 10 K cooling of the tropical tropopause was mainly caused by the added vertical resolution in Model II; smaller contributions were due to the use of a −40°C criterion for specifying supersaturation over ice (I–40, which reduced cirrus cloud cover) and the elimination of subgrid-scale temperature variance in the moist convection parameterization (I–29, which reduced penetrating convection and the associated vertical heat transport). A tropopause was introduced at high latitudes, i.e., the temperature decline with height became small above 200 mb, as a result of the addition of drag in the top model layer (I–10); a similar result was obtained by lifting the model top out of the stratosphere (I–12). The winter high-latitude inversion near the surface strengthened to a realistic magnitude when moist convection activity was allowed to initiate below the condensation level (I–34).

The primary deficiency of the zonal mean temperature in Model II is in the top model layer near the summer pole, where it is ~10 K too cold. Also, Northern Hemisphere polar surface temperatures are several degrees too cold in summer.

2) GLOBAL DISTRIBUTION

Surface air temperature in January and the January–July temperature change are shown in Fig. 21. Continental areas in Model I were up to 10 K too cold in winter and 5–10 K too hot in summer. Changes in Model II were brought about especially by the Ekman formulation for computing the surface wind, which warmed high-latitude regions in winter. Also, the adopted vegetation/ground hydrology changes (I–46, I–47, I–49) caused summer continental areas to be moister and cooler, reducing the seasonal temperature amplitude. Remaining deficiencies in Model II are especially notable in summer; e.g., the surface temperature is up to 5 K too cool in the Midwest during summer.

3) INTERANNUAL VARIABILITY

Interannual standard deviation of 850 mb temperature is given in Fig. 22 for a 15-year observational period and a 5-year run of Model II. Observed values in winter are as great as 5 K in Canada, Alaska and northeast Asia, and 2–3 K over the United States and

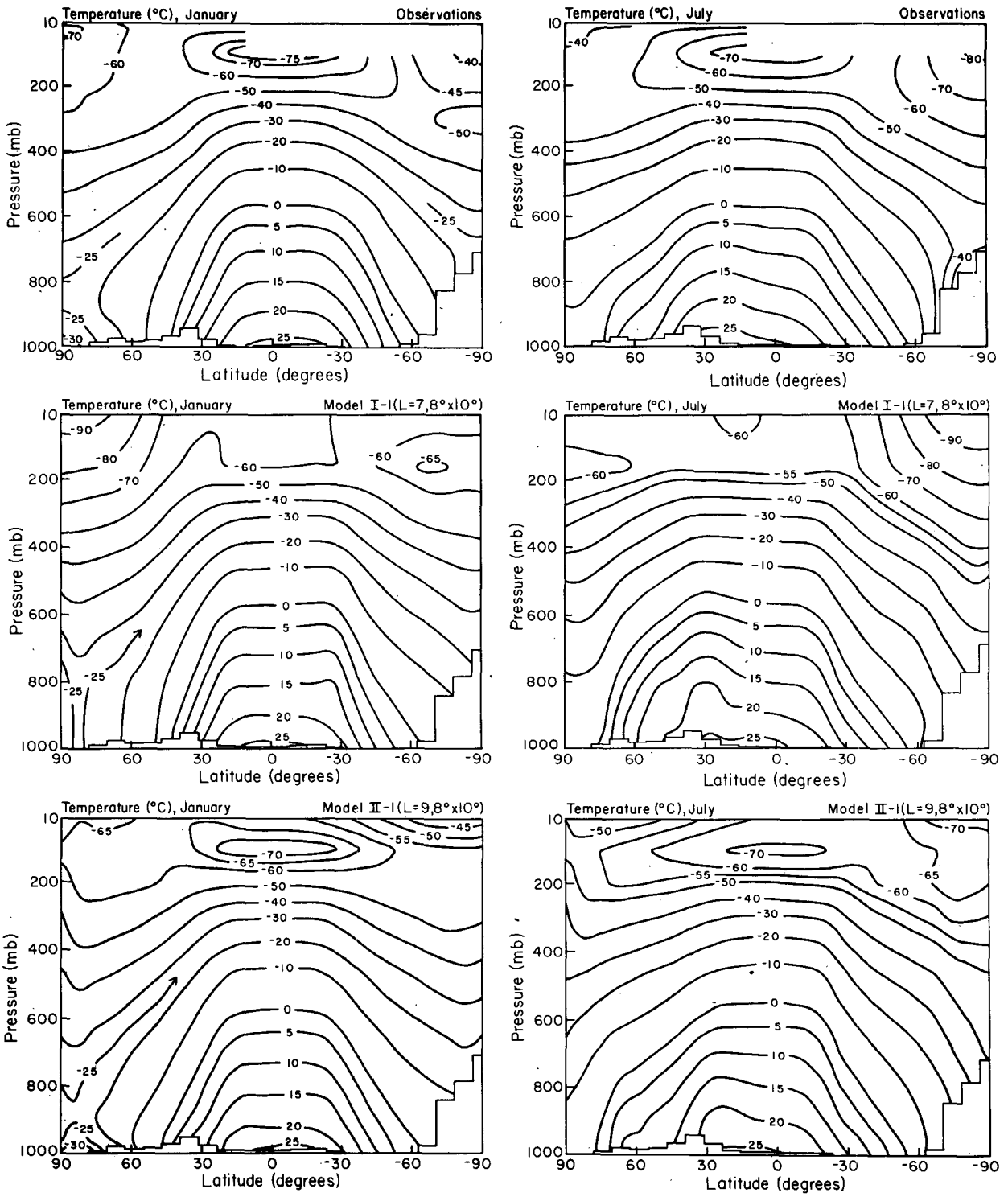

FIG. 20. Zonal-mean temperature for January (left) and July (right). Observations are from Crutcher and Meserve (1970) and Taljaard *et al.* (1969). Model results in Figs. 20–40 are 5-year means unless indicated otherwise.

Europe. Model I has spuriously large variability at a few points, associated with the extreme continentality of the model, and a variability several times too small over the oceans. Model II has realistic amplitude and geographical distribution of atmospheric temperature variability over the continents. Over the oceans the variability remains smaller than observed, apparently a result of the ocean temperature being specified

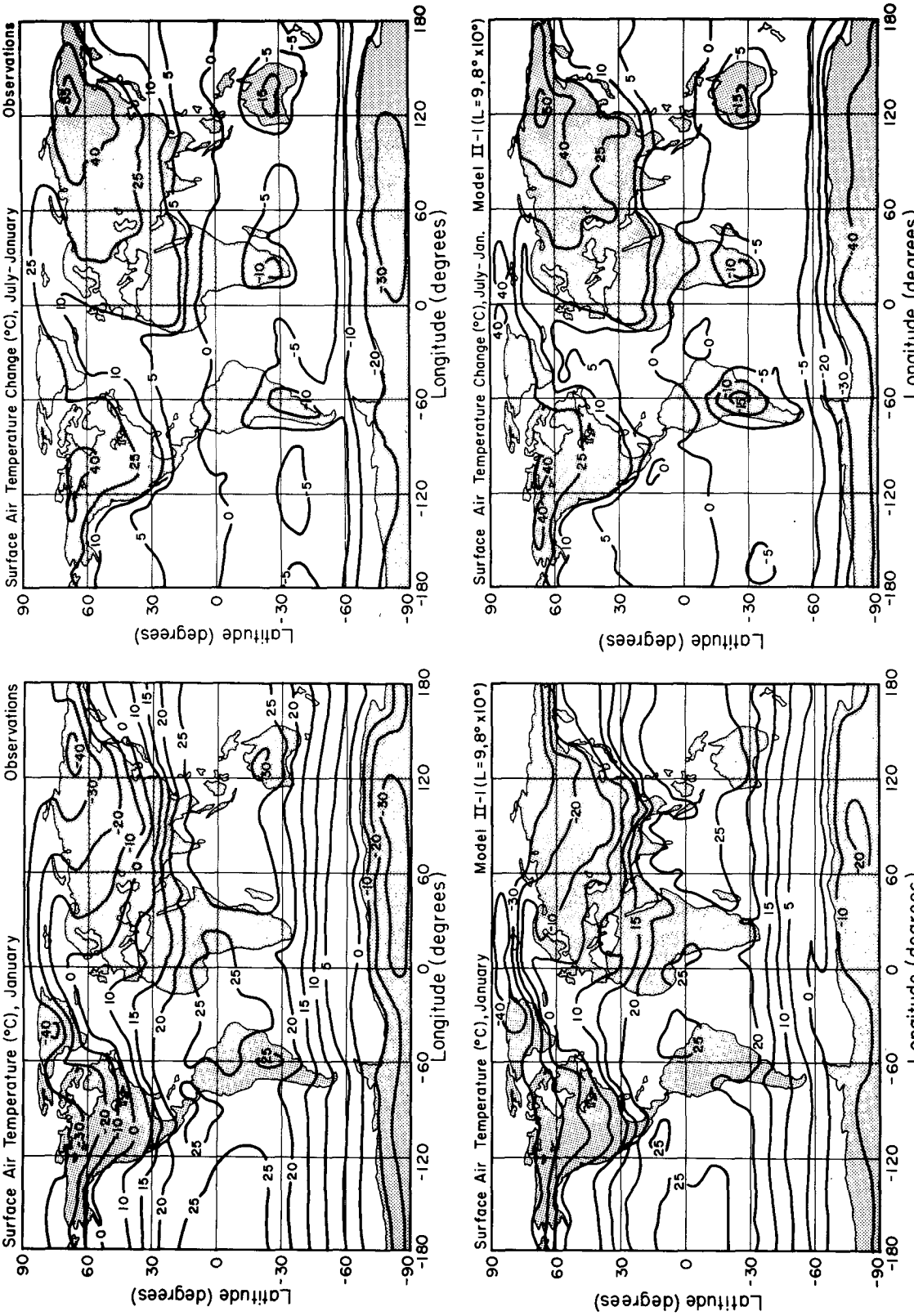

FIG. 21. Global distribution of surface air temperature for January (left) and July minus January (right). Observations are from Crutcher and Meserve (1970) and Taljaard *et al.* (1969).

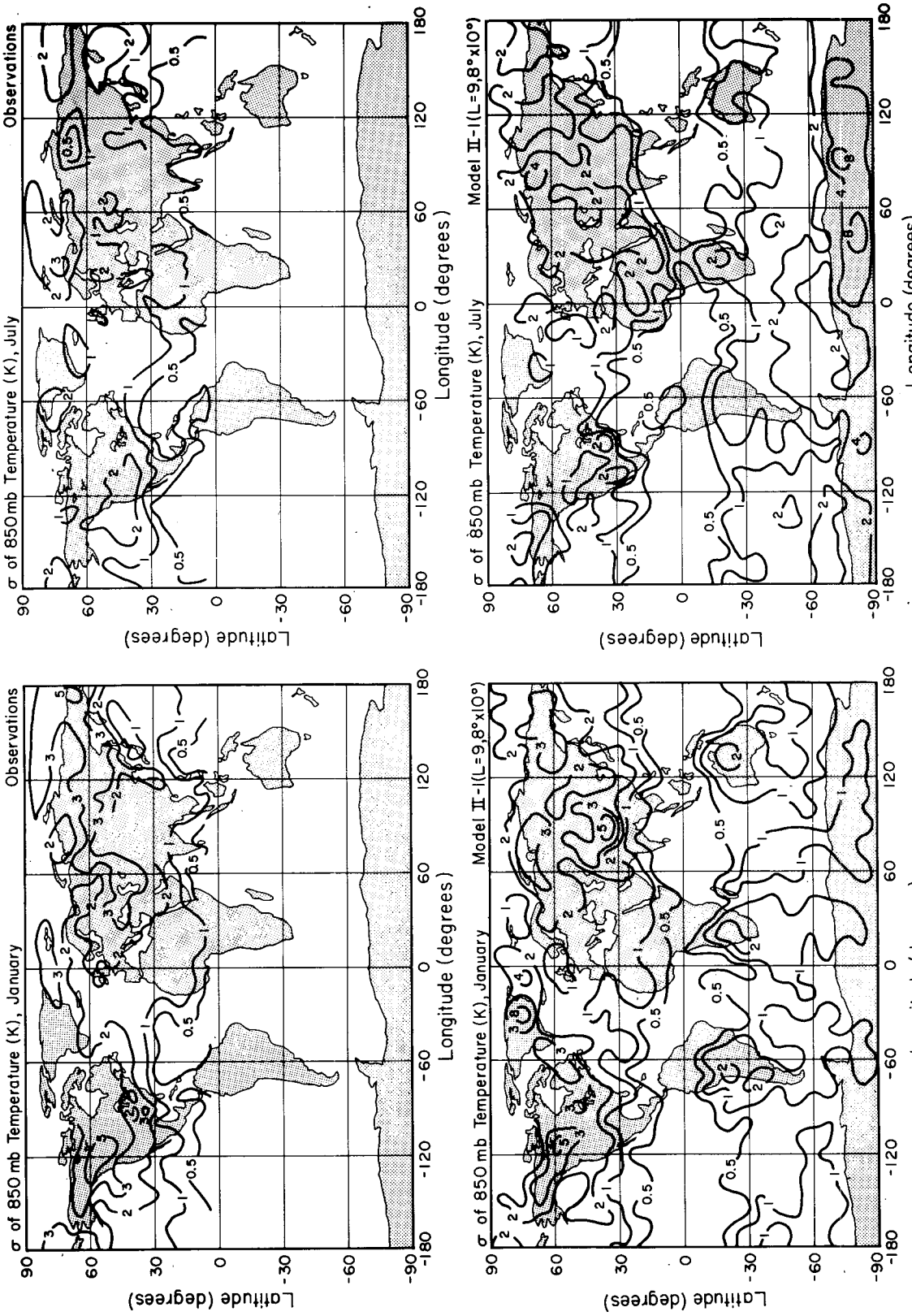

FIG. 22. Standard deviation of 850 mb temperature for January (left) and July (right). Observations are from Crutcher and Meserve (1970).

to be identical each of the 5 years. Indeed, when the fixed ocean temperature is replaced by a 65 m ocean with temperature computed from energy balance, the atmospheric temperature variability over oceans increases substantially. The interannual variability in Model II can be associated with varying synoptic situations and the amount of transient eddy kinetic energy (Section 3e).

b. Radiation and clouds

1) PLANETARY ALBEDO

The global distribution of albedo is shown in Fig. 23, and the latitude-season distribution in Fig. 24. The albedo in Model I is 5–10% too small at low latitudes, and 10–15% too large in parts of Canada and Siberia in January. The 5-year mean global albedo is 27.6% for Model I and 30.5% for Model II. The increase in Model II was caused mainly by the change from a 1 h to a 5 h time step for calculation of large-scale precipitation (I–36), which increased global cloud cover from 40 to 52%. Also, specification of ground albedo on the basis of local vegetation (I–51) increased albedos of subtropical land areas. Use of masking depths based on local vegetation (I–50) reduced the albedo of snow-covered regions to more realistic values. The albedo of Model II in tropical latitudes remains a few percent smaller than observed values.

2) NET RADIATION

The net radiation is shown in Fig. 24 as a function of latitude and season, and the global distribution in Fig. 25. Model I is deficient in net radiation from high latitudes in winter and has a surplus from the subtropics in summer, the discrepancies being of order 25 W m^{-2}. The high-latitude deficit is due to the low atmospheric temperatures. The subtropical surplus is associated with deficient cloud cover there. Both the temperature distribution and cloud cover are much improved in Model II. As a result, Model II is in generally good agreement with observed net radiation.

3) CLOUDS

Despite large uncertainties in observed cloud cover and the simplicity of the cloud generation scheme in the model, there is general agreement between observed and computed cloud patterns (Fig. 26). The increased cloud cover in Model II is in better quantitative agreement with observations.

In January, Model II produced 70% cloud cover over the North Pacific and North Atlantic storm track regions and realistic cloud cover over Europe. Large deserts are appropriately cloud-free and relative maxima of cloud cover appear in the vicinity of the ITCZ. The model fails to produce the cloud minimum in eastern Asia, though it generates realistic high pressure systems there. When the subgrid-scale temperature variance was omitted from the cloud generation scheme (I–35) a cloud cover minimum appeared in this region, but excessive clouds were produced over the ocean. Model II also yields regions of anomalously high cloud cover in the Bay of Bengal and off the west coast of Central America, which appeared when the Ekman surface wind formulation was introduced (I–58). Although the Ekman formulation generally reduced surface winds, in these particular regions the winds increased leading to greater evaporation and cloud cover.

In July, Model II cloud cover is similar to observations over the Americas, Africa and most of Asia. Large cloud cover does not extend far enough north over India, and there are too many clouds in northeast Australia. Large cloud cover over the Sahara in Model I is corrected in Model II. The Ekman wind formulation in Model II sharpened the ITCZ and reduced the monsoon-associated northward movement of clouds over India and Africa to a more realistic extent.

c. Precipitation and humidity

1) PRECIPITATION

Annual mean precipitation is given in Fig. 27. A chief problem in Model I was the movement of monsoon rainfall into the Sahara and central Asia in summer. Model II simulates the dry areas in the Sahara desert, off the west coasts of North and South America and southwest Africa, and in the lee of mountain chains such as the Andes and Himalayas; it is almost as dry as observed in the Australian and Gobi deserts. Regions of high rainfall are successfully reproduced along the equator and in the Amazon and African rainforests. Rainfall is excessive in the Bay of Bengal and in some mid-latitude regions. The greatest changes between Models I and II were due to incorporation of the Ekman wind formulation (I–58 and I–61). Also the ground hydrology changes (I–46, I–47, I–49) increased summer rainfall in the United States and Central Asia, while elimination of subgrid-scale temperature variance for moist convection (I–29) permitted more extreme longitudinal precipitation gradients (e.g., off the west coast of South America).

Interannual relative variability of precipitation is given in Fig. 27. Model I had excessive variability with unrealistic patterns. The magnitude of variability in Model II is more realistic, with maxima located appropriately in deserts and dry regions along Southern Hemisphere west coasts. The major deficiency in Model II is the lack of variability in the equatorial Pacific Ocean. The specified ocean temperature in the model is identical every year; thus it does not exhibit temperature changes such as those associated with El Niño.

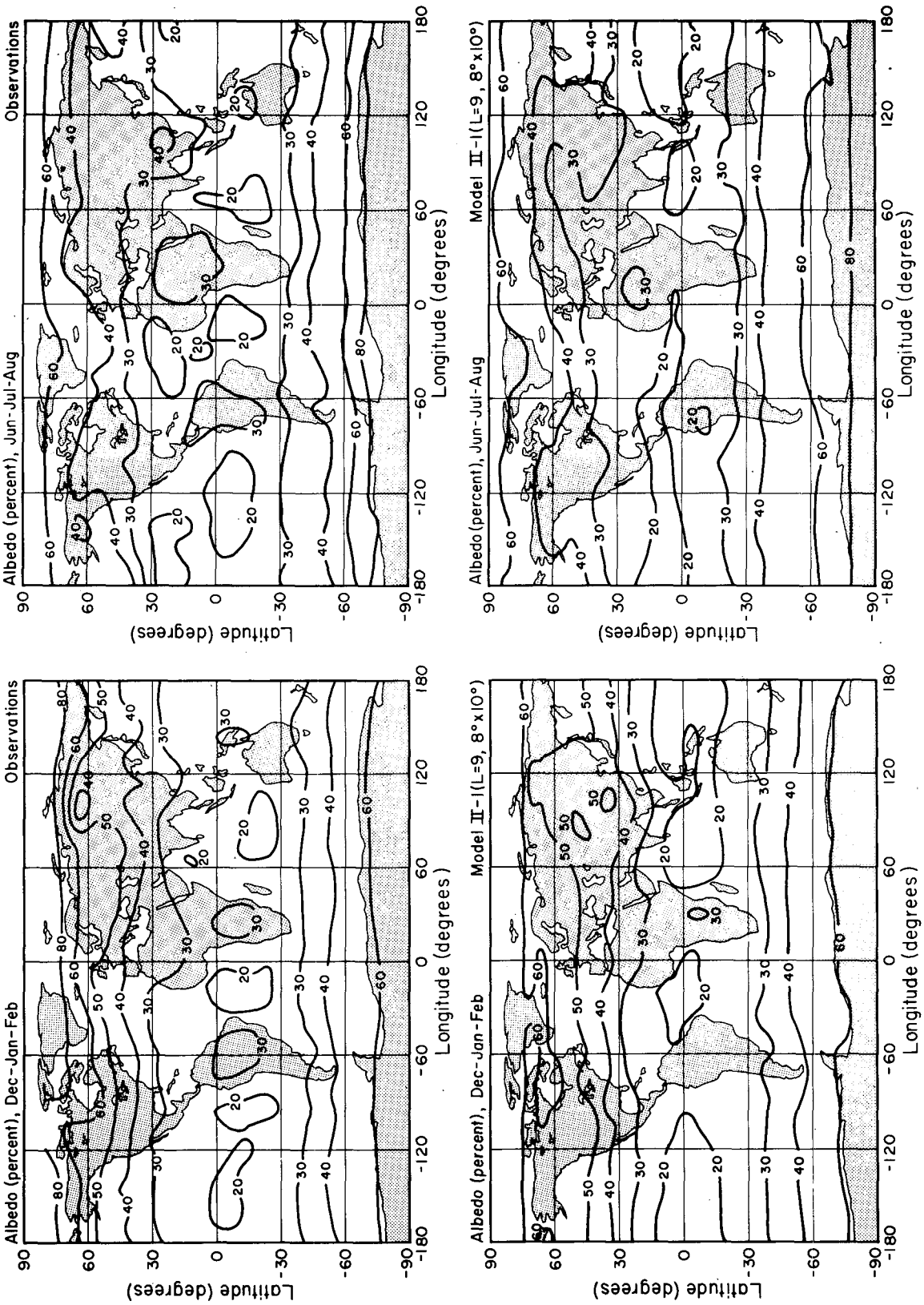

FIG. 23. Planetary albedo for December–February (left) and June–August (right). Observations are from Campbell and Vonder Haar (1980).

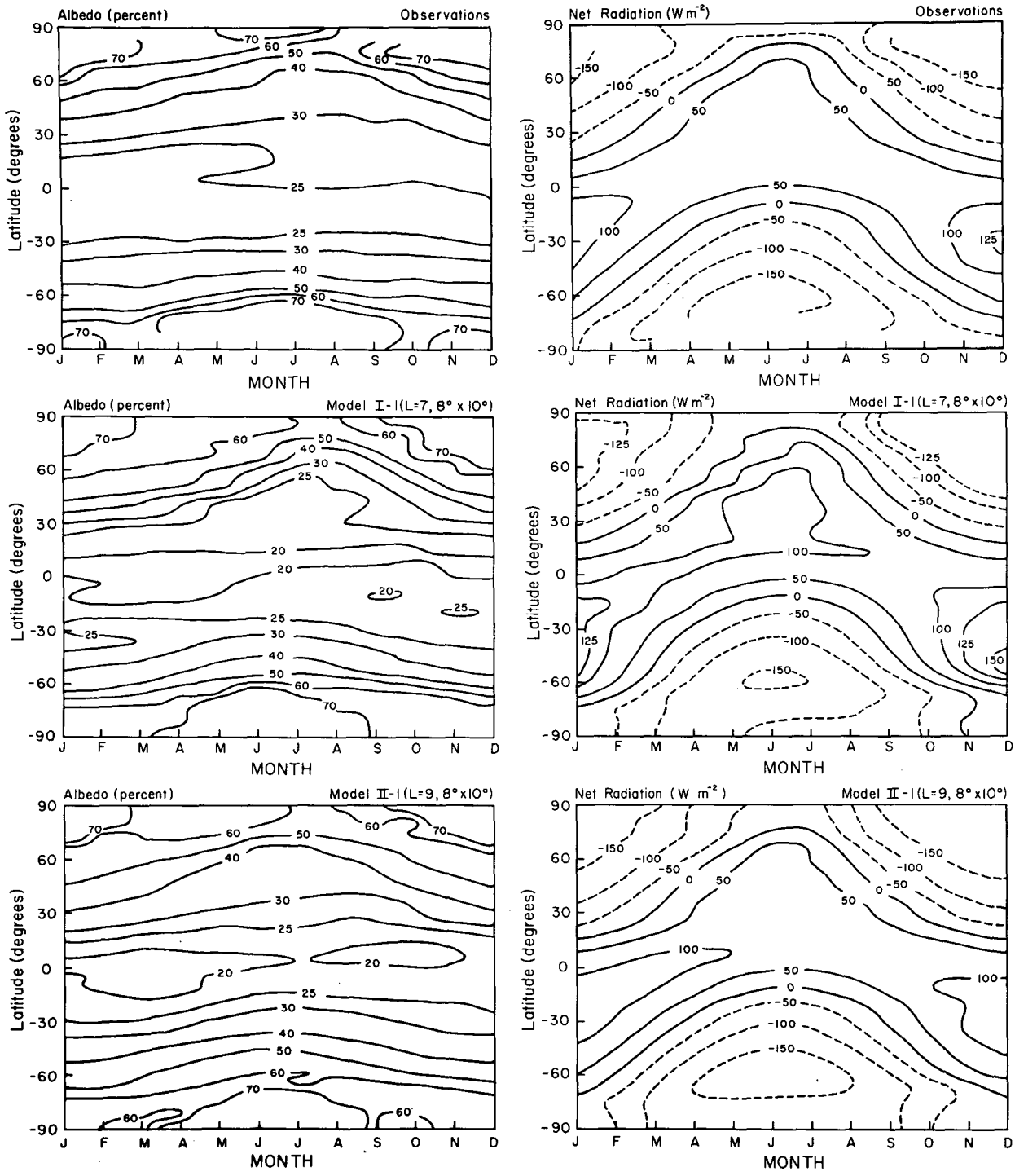

FIG. 24. Zonal-mean planetary albedo (left) and net radiation of planet (right). Observations are from Stephens *et al.* (1981). Contours are based on the monthly means assigned at the 12 indicated tick marks; thus the contours at the right and left edges of the graph are not identical.

Seasonal precipitation patterns (Fig. 28) are consistent with the discussion above. The poleward movement of precipitation in summer was too great in Model I. In Model II the Indian monsoon does not move far enough north into the Himalayas. Model II is somewhat too wet over the United States in summer; this result is sensitive to the ground hydrology formulation (Section 2g).

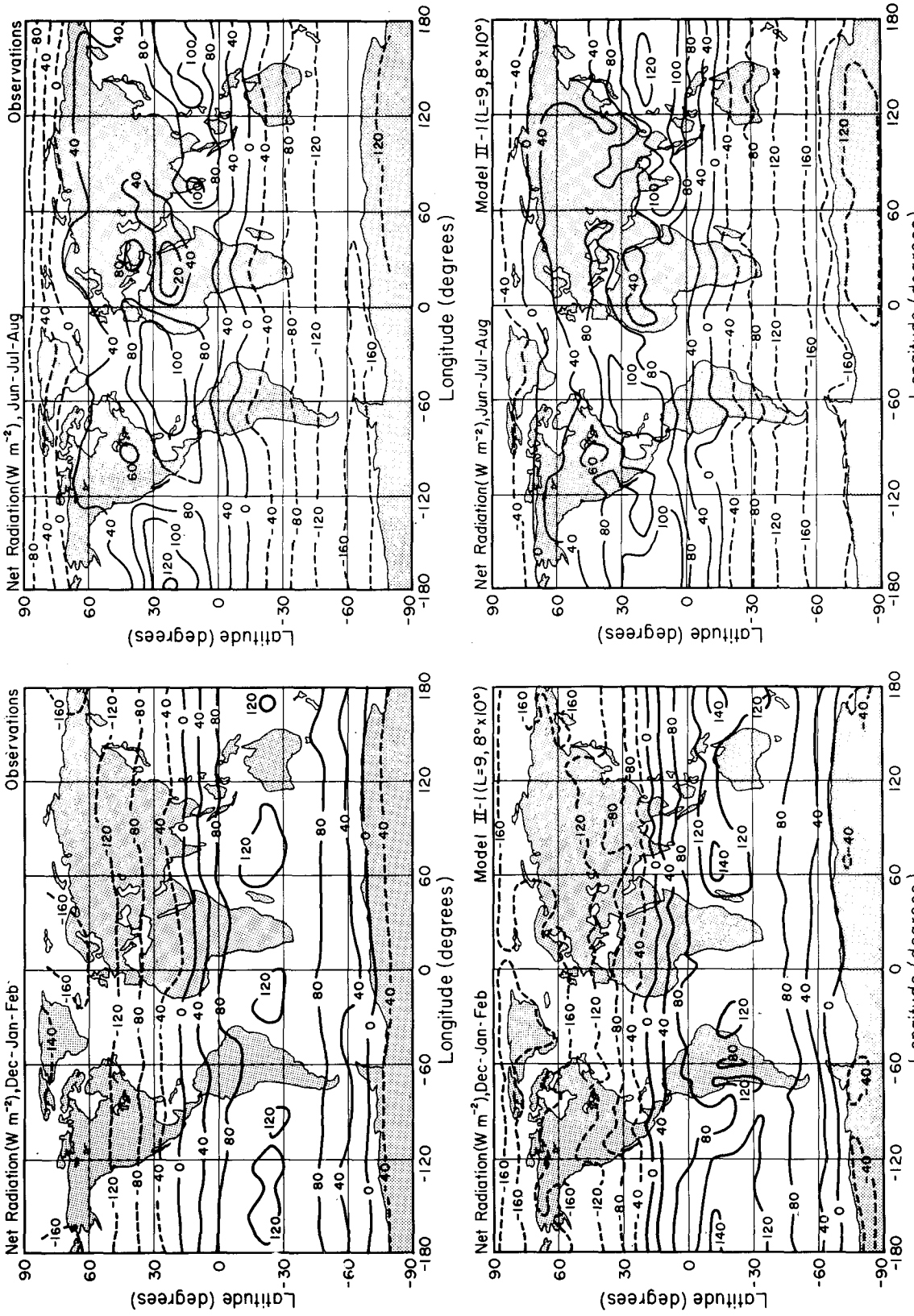

FIG. 25. Net radiation of planet for December–February (left) and June–August (right). Observations are from Campbell and Vonder Haar (1980).

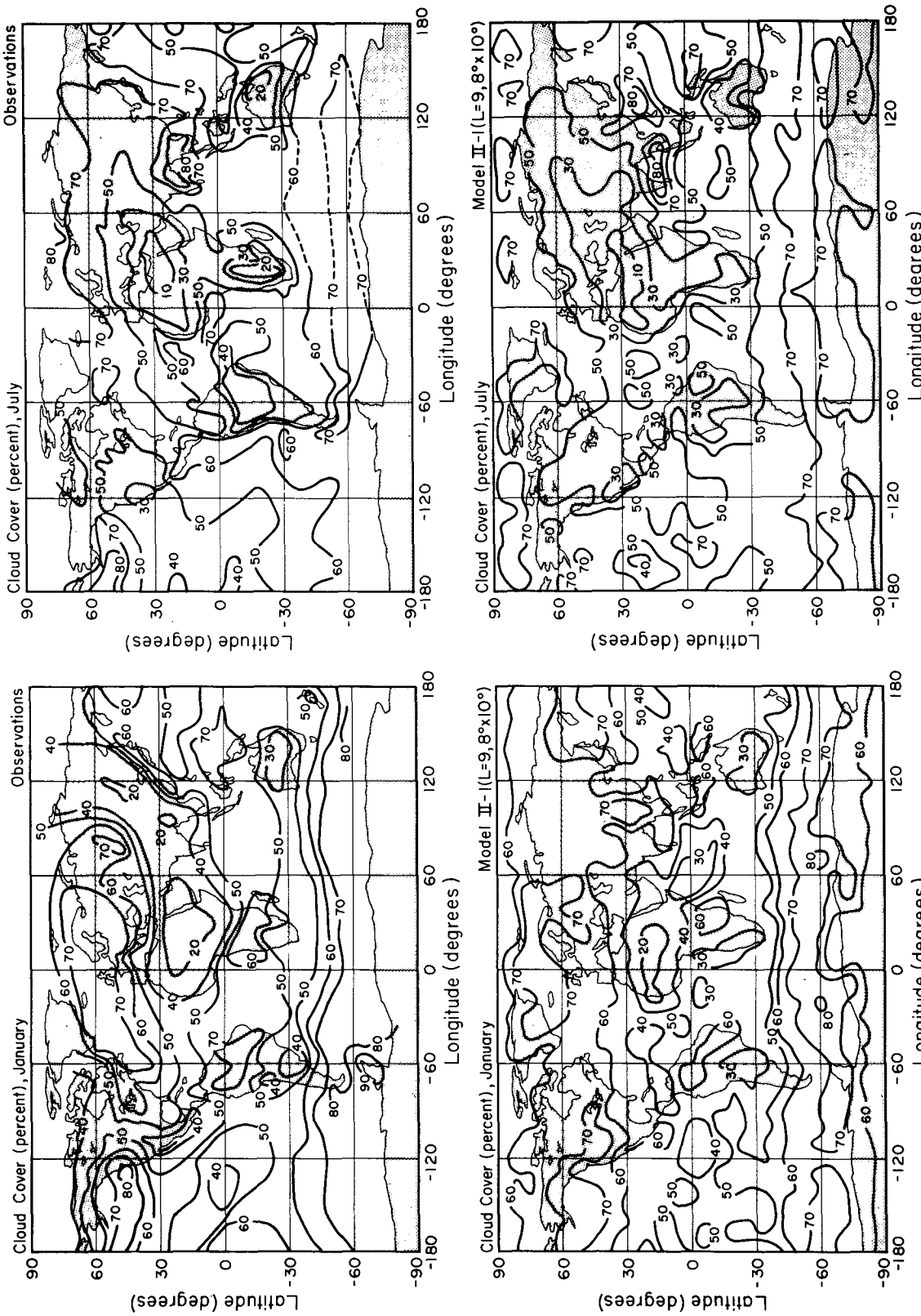

FIG. 26. Global cloud cover distribution for January (left) and July (right). Observations are from Berry *et al.* (1973).

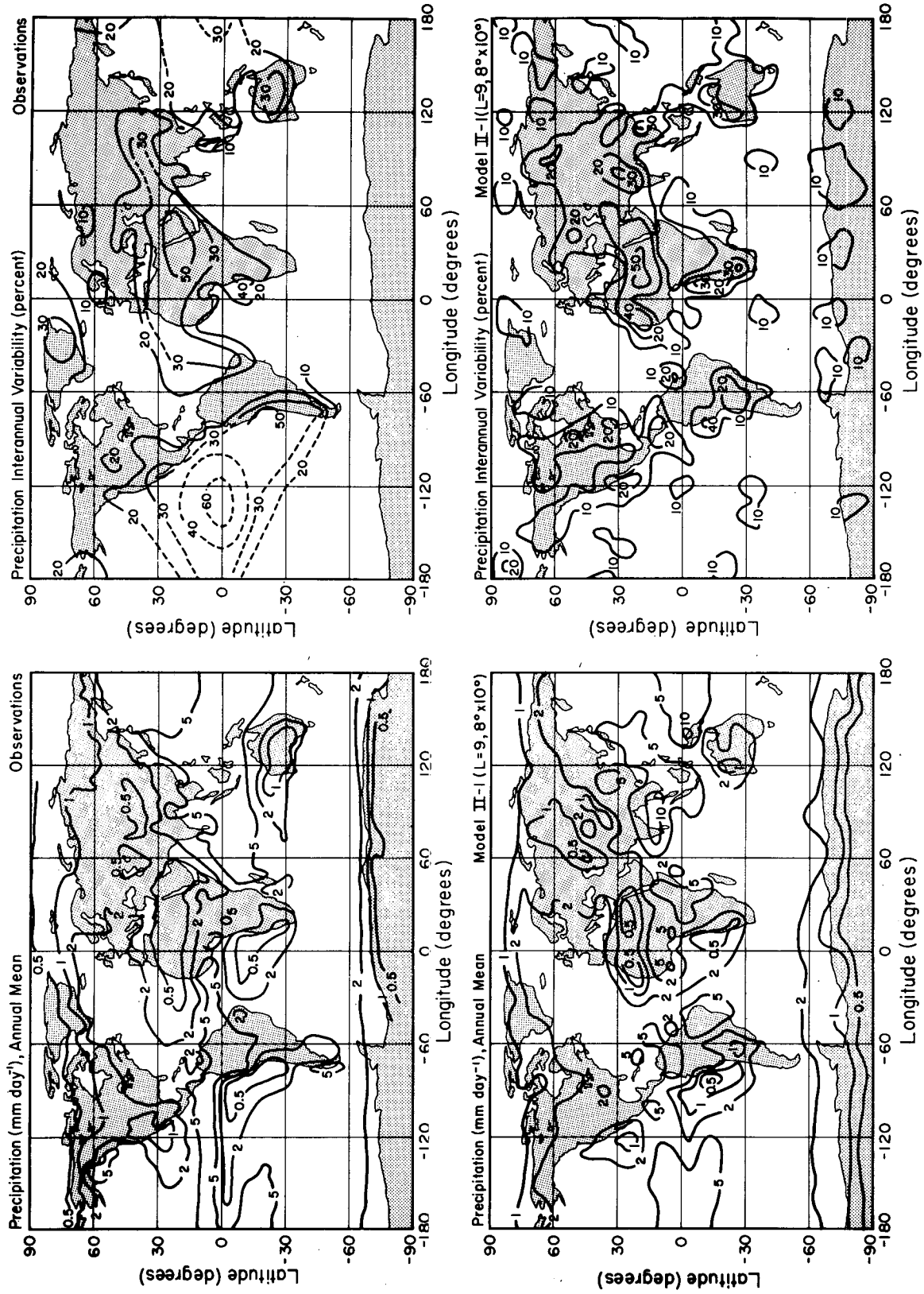

FIG. 27. Global distribution of annual-mean precipitation (left) and its interannual relative variability (right). Observed annual-mean precipitation is from Schutz and Gates (1971) and interannual variability from Berry *et al.* (1973).

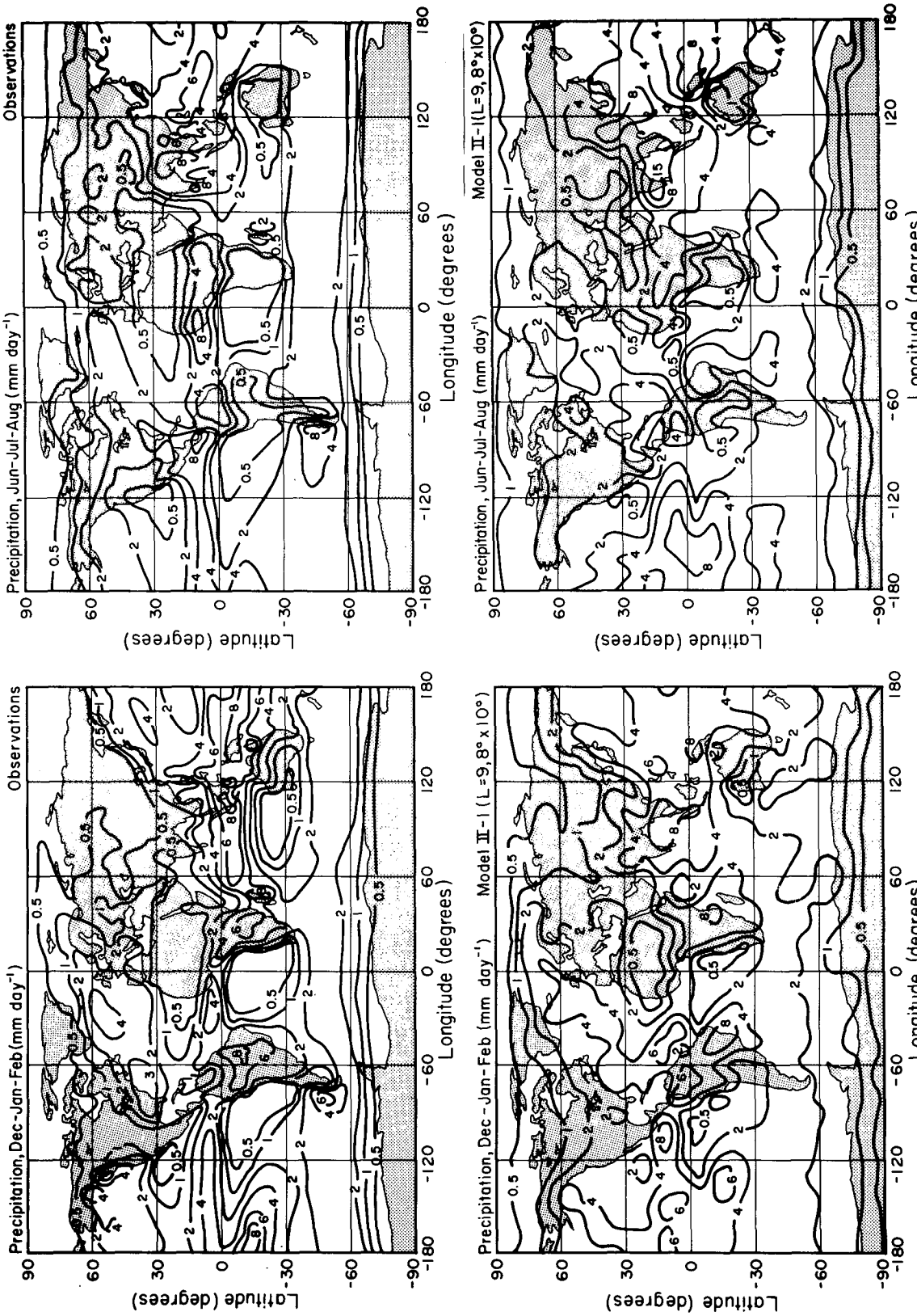

FIG. 28. Global distribution of precipitation for December–February (left) and June–August (right). Observations are from Schutz and Gates (1971).

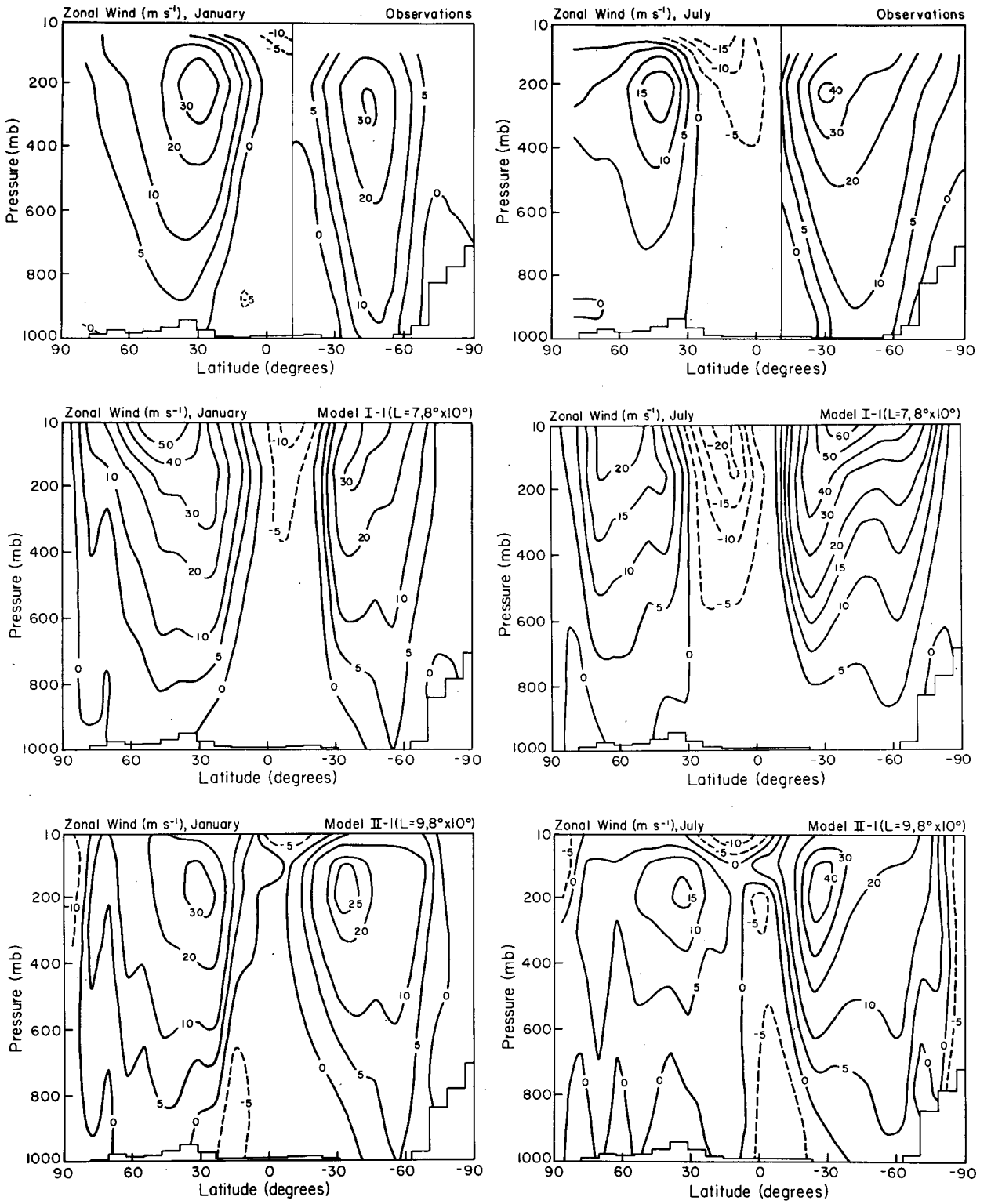

FIG. 29. Latitude-height profile of zonal-mean zonal wind for January (left) and July (right). Northern Hemisphere observations are from Oort (1982) and Southern Hemisphere from Trenberth (private communication, 1982) and Swanson and Trenberth (1981). Discontinuity at 10°S interface illustrates the uncertainty of analyses in data-sparse regions. We use the Swanson and Trenberth analysis because it employs basic dynamical constraints which should improve overall accuracy.

2) HUMIDITY

The humidity (not illustrated) appears to be realistic in both Models I and II, which is partly a reflection of the strong temperature dependence of saturation specific humidity. In both Models I and II the humidity decreases with height in the lower troposphere somewhat more rapidly than observed; this affects the dynamical transports of latent heat and energy (Section 3g).

d. Wind

1) ZONAL WIND

The zonal wind field (Fig. 29) has easterlies at low latitudes and jet streams of proper location and magnitude. The jet streams in Model I are not closed, and attain excessive velocities near the model top. This unrealistic aspect was corrected by incorporation of drag in the top model layer (I–10). It was also corrected when the model top was raised out of the stratosphere (I–12), indicating that the artificial rigid lid boundary condition (5) was the cause of the problem. The chief deficiencies in the zonal wind field of Model II occur in summer, the subtropical jet and tropical easterlies being weaker than observed.

2) SURFACE WIND

The surface wind field produced by the model is realistic in its broad features, as illustrated in Fig. 30 for January and July of Model II–1. The January and July simulations both feature easterly trade winds at low latitudes, westerly flow at middle latitudes and light easterlies at high latitudes. In July the southeast trades sweep north of the equator (the "hooked

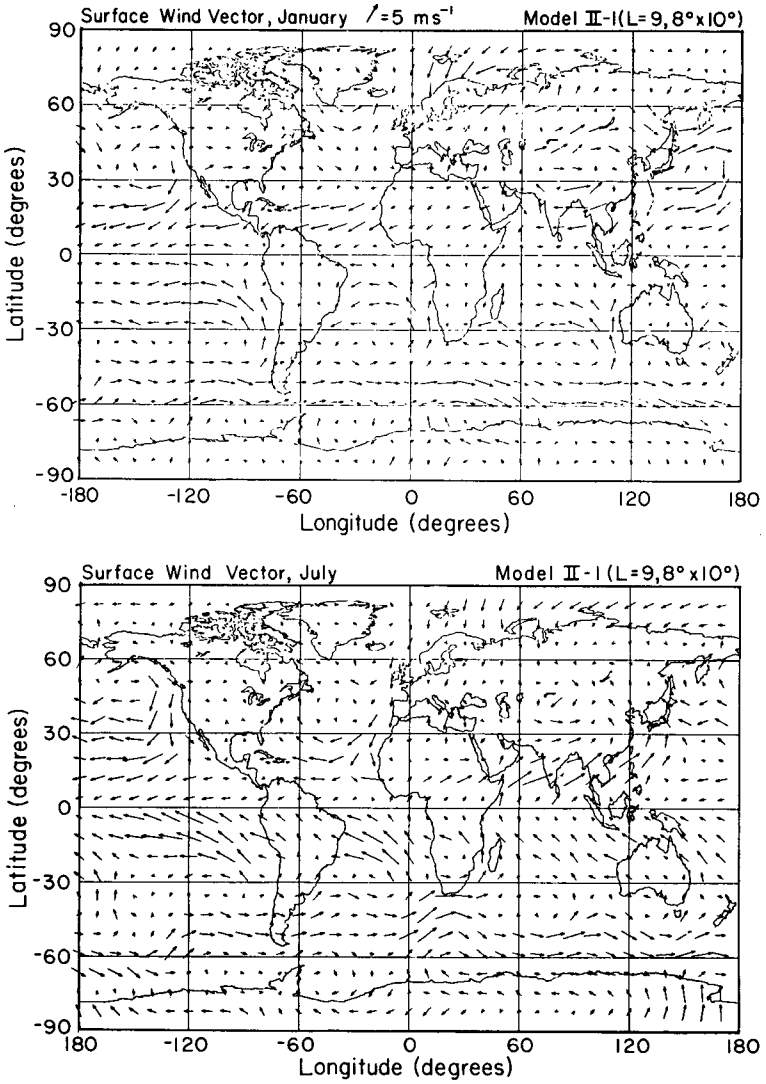

FIG. 30. Surface wind field for January (top) and July (bottom) from Model II.

trades") such that the ITCZ is displaced far northward over Africa and Asia. Prevailing anticyclonic flow occurs over the subtropical oceans, with more cyclonic curvature further poleward in winter. The flow over Asia changes from anticyclonic in winter to cyclonic in summer.

3) STREAMFUNCTION

The mass streamfunction (Fig. 31) provides a convenient representation of the zonally averaged meridional and vertical wind fields, but the actual streamfunction is very uncertain; for example, different analyses of even the same observations yield differences of as much as 50% in the peak values of the Hadley and Ferrel cells and 10° in the location of their maxima (Starr *et al.*, 1970). Nevertheless, it is clear that in Model I the Hadley cell is much too broad, the Ferrel cell peaks too far north, and no polar cell exists. Model II is more realistic in winter. The Hadley cell remains perhaps 10–20% too weak with peak intensity about one gridbox (8°) too far north; the Ferrel cell is less than half of its observed strength, but its position is improved.

The reduction in the width of the Hadley cell in Model II was caused by the cross-isobar angle correction at low latitudes (I–61) which sharpened the ITCZ, and by elimination of the subgrid-scale variance for moist convection (I–29) which reduced the height of penetrating convection. The polar cell developed when the Coriolis and metric terms were included in the numerical calculations at the poles (I–6). The combination of these changes positioned the Ferrel cell further south in winter. The strength of the Ferrel cell depends on the vertical gradient of the horizontal eddy momentum flux convergence and the meridional gradient of the eddy heat flux convergence (Holton, 1979). Thus it is sensitive to first and second derivatives of eddy transports and is highly variable. We conclude that the Ferrel cell transports are weak, despite the magnitude of the eddy transports being realistic, as a result of the spatial structure of the eddy fluxes not being adequately resolved by 8° × 10° resolution.

e. Eddy kinetic energy

Eddy kinetic energy (Fig. 32) is deficient through most of the troposphere in Model I, and excessive in the stratosphere. The stratospheric excess was eliminated by incorporation of stratospheric drag (I–10), which directly removed energy and modified the zonal wind profile such that the refractive index for vertically propagating waves increased reflection back to the troposphere. The large increase in total eddy kinetic energy between Models I and II resulted from two changes which reduced loss mechanisms for eddy energy by about equal amounts: the altered prescription for calculating surface wind (I–58, I–59, I–60, I–61) and the elimination of subgrid-scale temperature variance in moist convection (I–29). The energy increase occurred especially in synoptic scales (Fig. 17).

Despite a modest excess of total eddy kinetic energy in Model II, compared to the observational analysis of Oort (1982), the energy in wavenumbers 6–10 is similar to observations reviewed by Saltzman (1970). Waves 1–5 are somewhat weaker than in the observations reviewed by Saltzman, and the strength of synoptic-scale waves relative to long waves is clearly larger in Model II than in observations.

Transient eddy kinetic energy (Fig. 33) is deficient in the troposphere of Model I by at least a factor of 2. However, it increases substantially in Model II, and is even somewhat excessive in the lower troposphere at mid-latitudes in January. In July the transient eddy kinetic energy in the region of the Northern Hemisphere jet stream is still somewhat smaller in Model II than in observations. The prime causes of the increased transient eddy energy in Model II are the two reasons discussed above for the increase of total eddy kinetic energy.

f. Sea level pressure

Sea level pressure patterns and their interannual variability are strongly dependent on the atmospheric eddy kinetic energy. We show the 5-year mean sea level pressure for Model II in Fig. 34 and an example of interannual variability in Fig. 35. The model produces low pressure regions over the ocean and high pressure over the continents in Northern Hemisphere winter as in observations, but the low pressure regions are too localized. There are significant shortcomings in the Southern Hemisphere sea level pressure simulation, especially the absence of deep subpolar lows. Low pressures over the ocean are more realistic with higher resolution (Section 4). Sea level pressure is several millibars too small in the model at low latitudes, and too large at polar latitudes.

The sea level pressure has substantial variability in the model, comparable in magnitude to that which is observed. For example, the Icelandic low is weak in year 3 but deep in year 5 while the Aleutian low has the opposite pattern; this is similar to an observed teleconnection pattern (Wallace and Gutzler, 1981). Also, in North America a high pressure system is centered in southeast Canada in year 3, while ridging occurs along the west coast in year 5.

g. Energy cycle

Generation and destruction of energy in January by Model II–1 is shown in Fig. 36, as well as the energy cycle between total potential energy, and zonal and eddy kinetic energy. We use total potential energy, as opposed to available potential energy, since it requires no assumption of a steady, arbitrary ref-

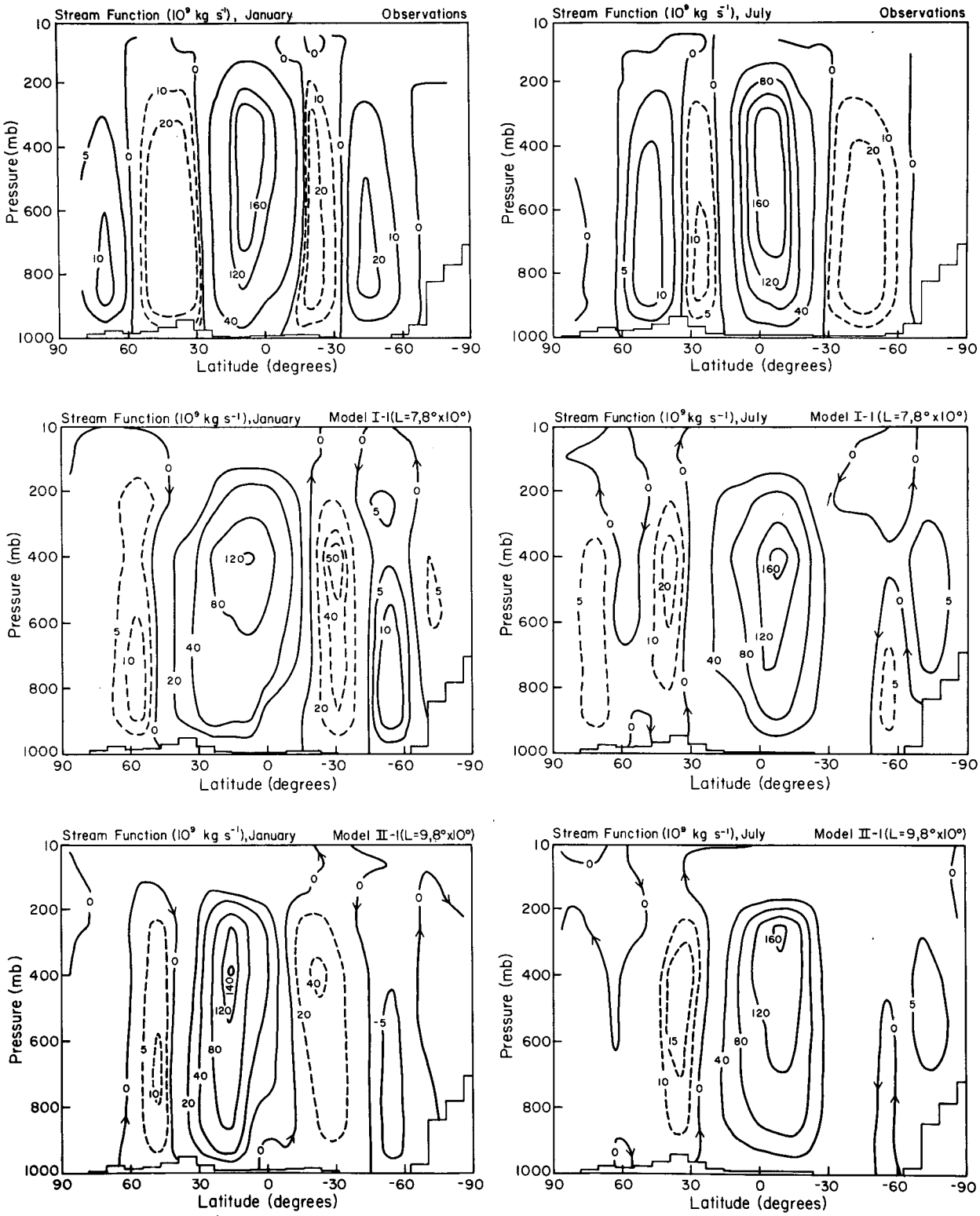

FIG. 31. Zonal-mean mass streamfunction for January (left) and July (right). Observations are from Oort (1982). Sign convention, given by arrows on the zero contours, is opposite in January and July.

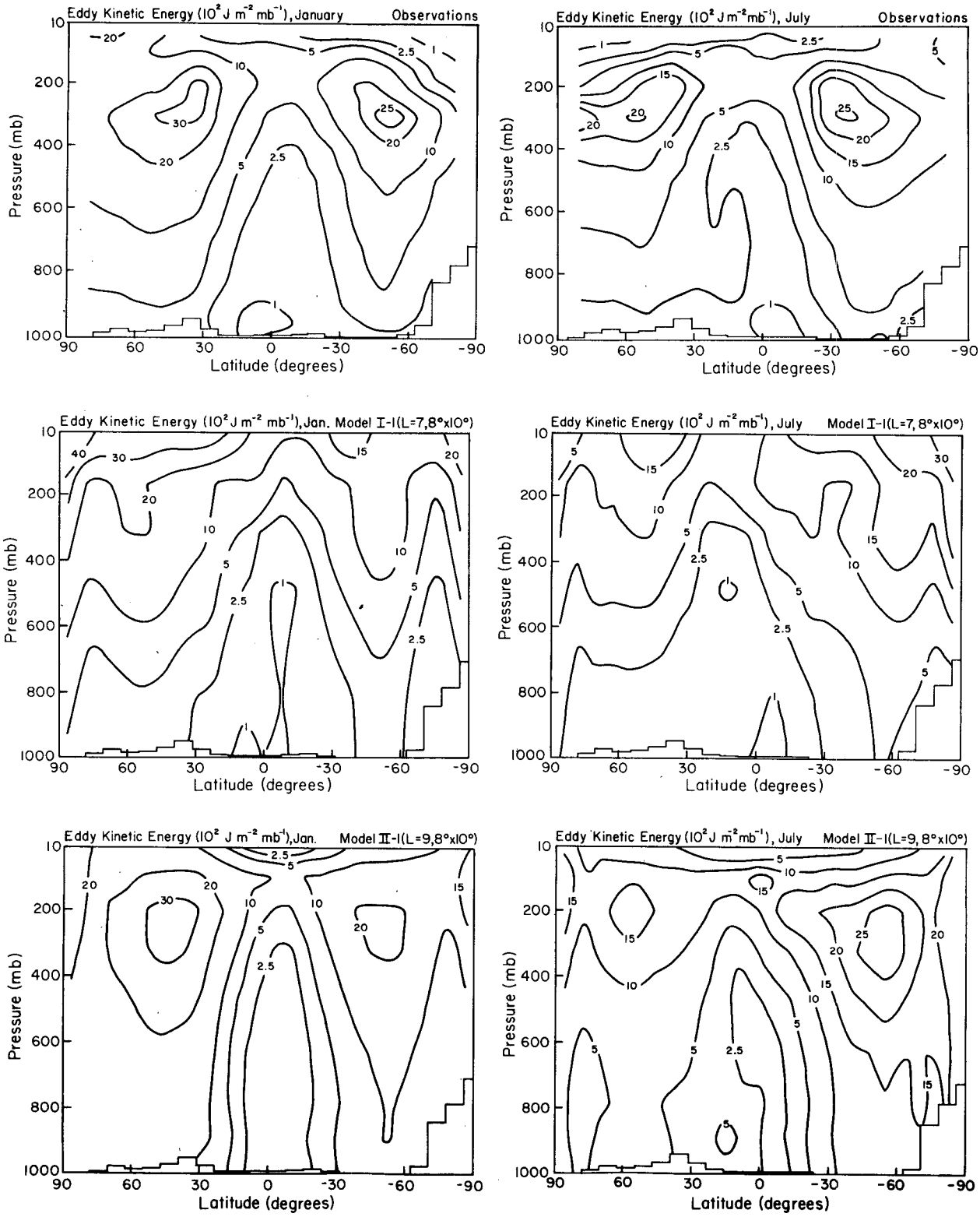

FIG. 32. Zonal-mean eddy kinetic energy for January (left) and July (right). Observations are from Oort (1982).

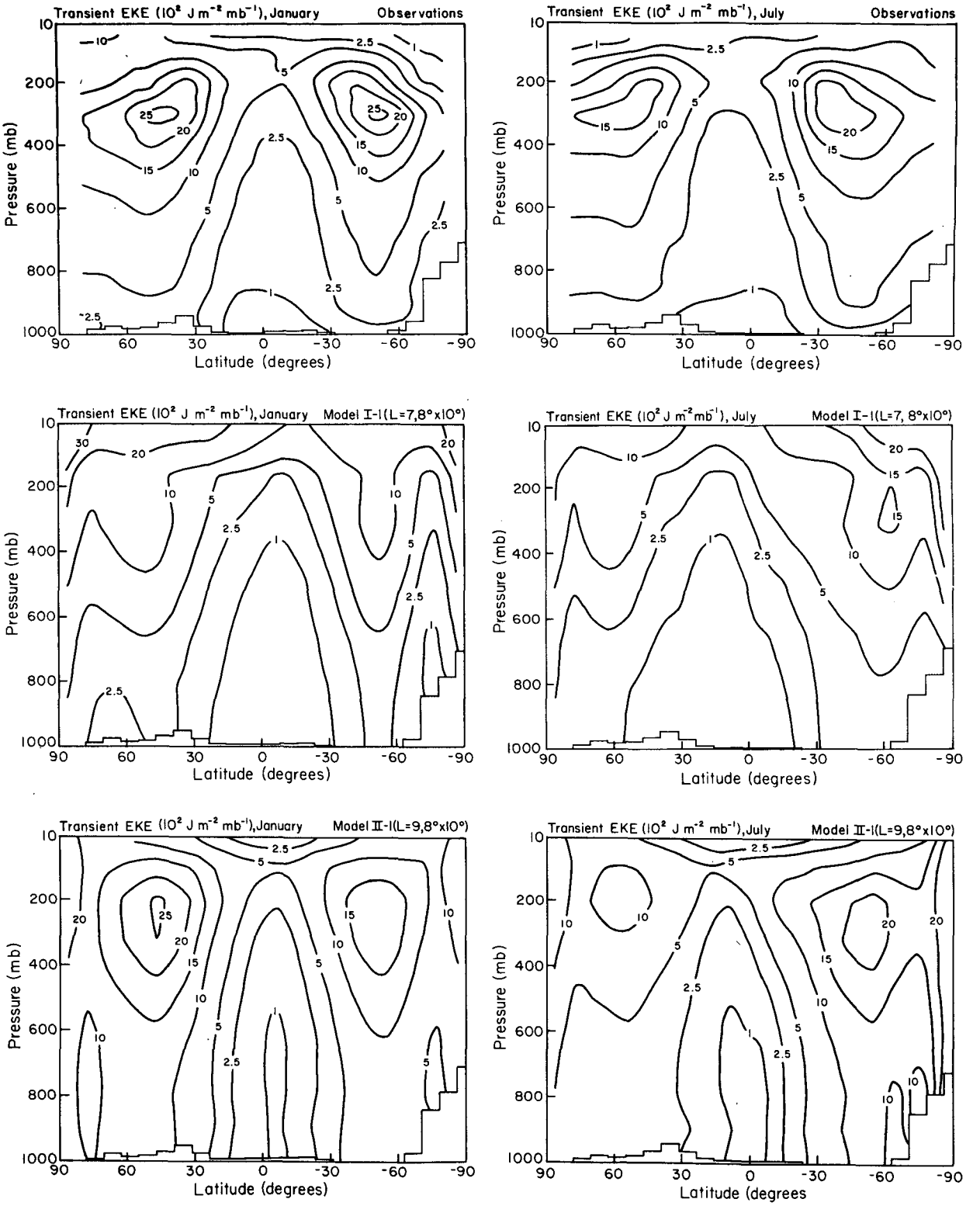

FIG. 33. Zonal-mean transient eddy kinetic energy for January (left) and July (right). Observations from Oort (1982).

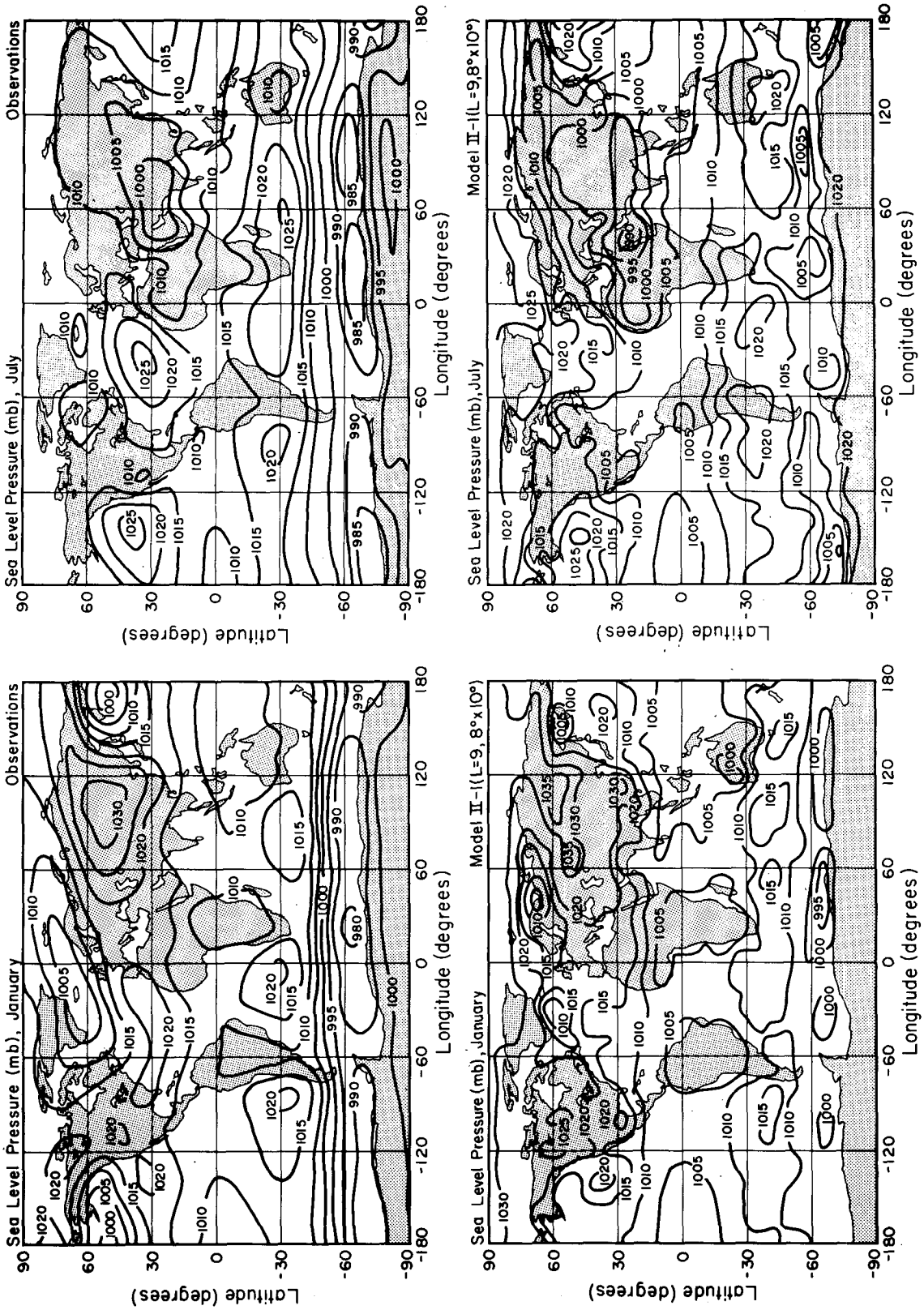

FIG. 34. Sea level pressure for January (left) and July (right). Observations are from Crutcher and Meserve (1970) and Taljaard *et al.* (1969). At gridpoints of high topography sea level pressure is obtained by interpolation from neighboring gridpoints.

erence state and can be calculated precisely in σ coordinates. Potential energy in the model is generated primarily by condensation and atmospheric absorption of solar radiation; computer truncation and the sea level pressure filter have negligible effects. Major loss mechanisms are mixing of momentum by convection and surface friction, although the stratospheric drag contributes 10% to the energy loss. The transfers from potential energy to kinetic energy, and from eddy to zonal kinetic energy agree well with observations (Oort, 1964), as does the total rate of energy destruction. Also the global efficiency for conversion of sunlight incident at the top of the atmosphere to kinetic energy (0.0065) is in good agreement with observational analyses (Oort, 1964).

h. Transports

Vertically integrated northward transports of sensible heat, total energy and angular momentum are shown in Figs. 33–39. In each figure the transports by eddies are on the left and the total atmospheric transports on the right.

Eddy transports of all three quantities in Model II have the observed shape for the seasonal variation including an appropriate midlatitude winter peak. This is in accord with the realistic temperature, wind and moisture fields. The improved distributions in Model II, compared to Model I, are primarily a result of the greater transient eddy activity in Model II.

Total transports (eddy plus mean circulation) are also generally realistic in Model II. The apparent discrepancy in energy transport in Northern Hemisphere midlatitudes is due in part to a difference in analyses of the model and observations: the model results are the total transport up to 10 mb, while the observations (Oort, 1982) include transports only up to 50 mb. The transports below 50 mb are closer to the observations. The model does underestimate energy transport by the mean circulation at 30–60°N, just as it underestimates the Ferrel cell. At low latitudes the model underestimates the peak latent heat transports (not illustrated), partly due to the moisture distribution which falls off more quickly with height than observed in the equatorial lower troposphere.

The influence of eddies on the zonal mean circulation depends on the degree of wave transience, diabaticity and dissipation (e.g., Andrews and McIntyre, 1976). Eddy transports in the model are realistic (Figs. 37–39) as are the zonal mean temperature and wind fields (Figs. 20 and 29), implying that the eddies are forcing the mean circulation in a manner consistent with the real atmosphere, with realistic magnitudes of transience, diabaticity and dissipation. The Eliassen-Palm flux (Eliassen and Palm, 1961) provides another method of examining these effects: regions of divergence and convergence of this flux show where the eddy sensible heat and momentum fluxes

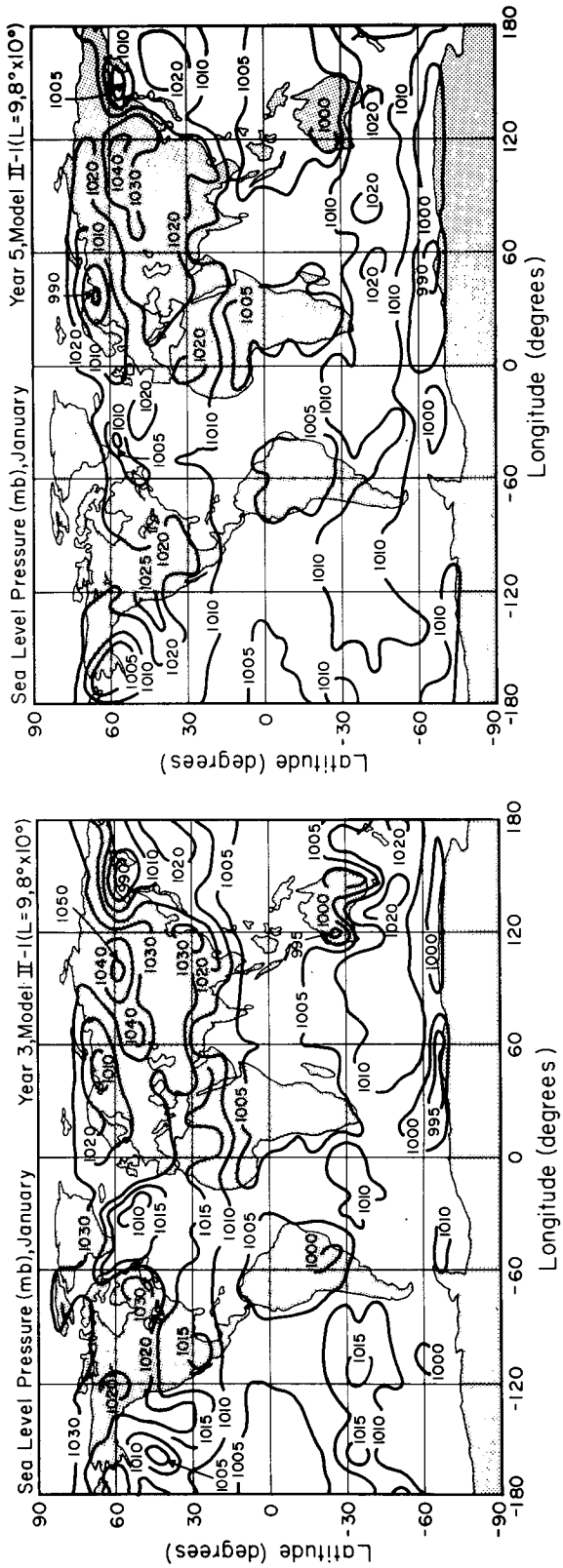

FIG. 35. Sea level pressure in January for years 3 and 5 of Model II.

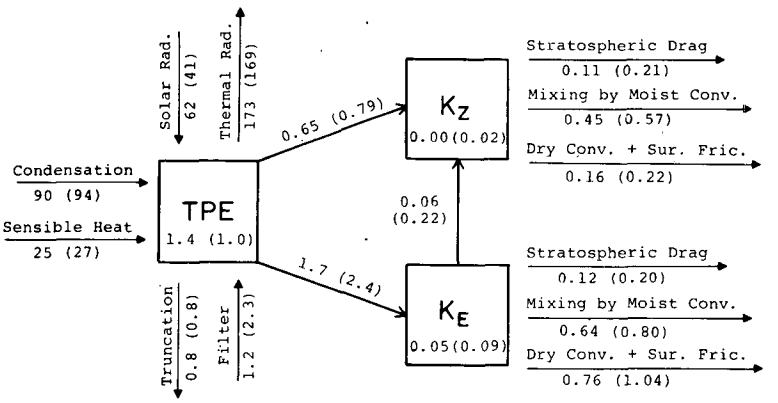

FIG. 36. Global generation and destruction of energy (W m^{-2}) in January by Model II-1 (Northern Hemisphere in parentheses). Numbers in the boxes are the increase during the month. In the calculations for this diagram kinetic energy was divided into zonal and eddy components on the σ coordinate surfaces; all other figures in this paper employ model quantities which have been interpolated to constant pressure surfaces, to provide appropriate comparison to observational data.

supply a net forcing of the zonal flow. The Eliassen-Palm flux and divergence produced by the model are shown in Fig. 40 for January and July. Wave "activity" propagates vertically from regions of generation in the lower troposphere to an area of convergence at the zero wind line between tropical east winds and mid-latitude west winds in the subtropical upper troposphere, especially in the winter hemisphere, where it acts to decelerate the zonal winds. This is in good agreement with observations for both winter and summer (Fig. 5 of Edmon *et al.*, 1980).

4. Resolution experiments

The effect of horizontal resolution was tested by making runs with 4° × 5° and 12° × 15° resolutions, for comparison to the 8° × 10° results. These runs were started on 1 November and integrated four months. Comparisons are made for January or December–February, in accord with available observations.

Atmospheric temperature is illustrated in Fig. 41 (zonal mean vertical cross-section), Fig. 42 (global map of surface air temperature) and Fig. 43 (zonal mean surface air temperature). The same maps are given in Figs. 21, 28 and 34 for 8° × 10° resolution. All three resolutions are in good agreement with observations. In part, this is attributable to the specified climatological sea surface temperature, but the realistic strength of the eddies and eddy transports (see below) is also a necessary condition. The temperature is several degrees too cold at high latitudes in winter for 12° × 15° resolution, consistent with the poleward transport of heat being slightly too weak.

The zonal wind (Figs. 41 and 29) is clearly more realistic at 8° × 10° than at 12° × 15° resolution; the main further change in going to 4° × 5° resolution is a strengthening of the mid-latitude westerlies, which can be attributed to increased eddy momentum flux into mid-latitudes (discussed below). The tropical easterlies are poorly represented at 12° × 15° but they extend vertically throughout the atmosphere at 8° × 10° (and 4° × 5°). The large change in the Southern Hemisphere jet stream also occurs in going from 12° × 15° to 8° × 10°. The Northern Hemisphere jet stream is slightly weaker for 8° × 10° resolution (peak value 34 m s^{-1}) than for either 12° × 15° (37 m s^{-1}) or 4° × 5° (41 m s^{-1}). The standard deviation of the jet stream speed is 2–3 m s^{-1} in the 5-year 8° × 10° run, with speed 36 m s^{-1} in the first year, so the differences are not significant.

The zonal mean streamfunction (Figs. 41 and 31) shows the core strength of the Hadley cell to increase only slightly as the resolution increases, 4° × 5° resolution yielding results marginally closest to observations. However, the width of the Hadley cell is most realistic for 8° × 10° resolution. The Hadley cell is too far north and too narrow for 4° × 5° resolution, which is consistent with the very sharp ITCZ for that resolution (see below). The Ferrel cell improves greatly as the resolution improves: there is no significant Ferrel cell at 12° × 15° resolution, it is too far poleward and much too weak for 8° × 10° but it has accurate strength and location for 4° × 5°. The Ferrel cell is sensitive to the eddy momentum flux (see below) and the surface dissipation which is higher because of stronger surface winds (see above); this probably accounts for the changes with resolution. The changes in the Hadley and Ferrel cells with resolution are similar in the two hemispheres.

The global precipitation distribution is shown in Figs. 42 and 28 and the zonal mean precipitation in Fig. 43. There are major improvements in the precipitation distribution in going from 12° × 15° to 8° × 10° resolution, and perhaps some further net improvement for 4° × 5°. Dry regions such as the Sahara and the area southwest of California are not well

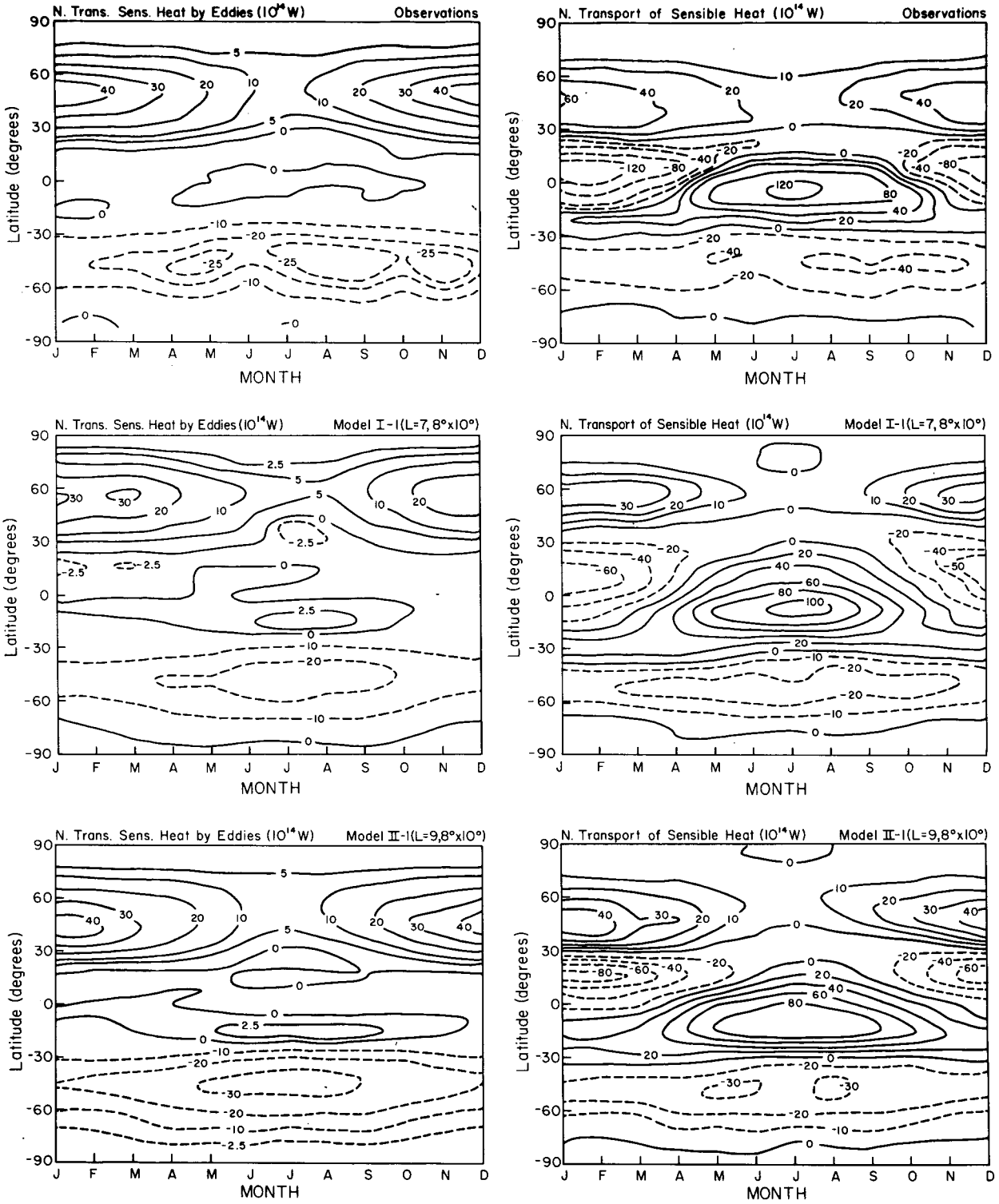

FIG. 37. Northward transport of sensible heat by eddies (left) and by eddies plus mean circulation (right). Observations are from Oort (1982).

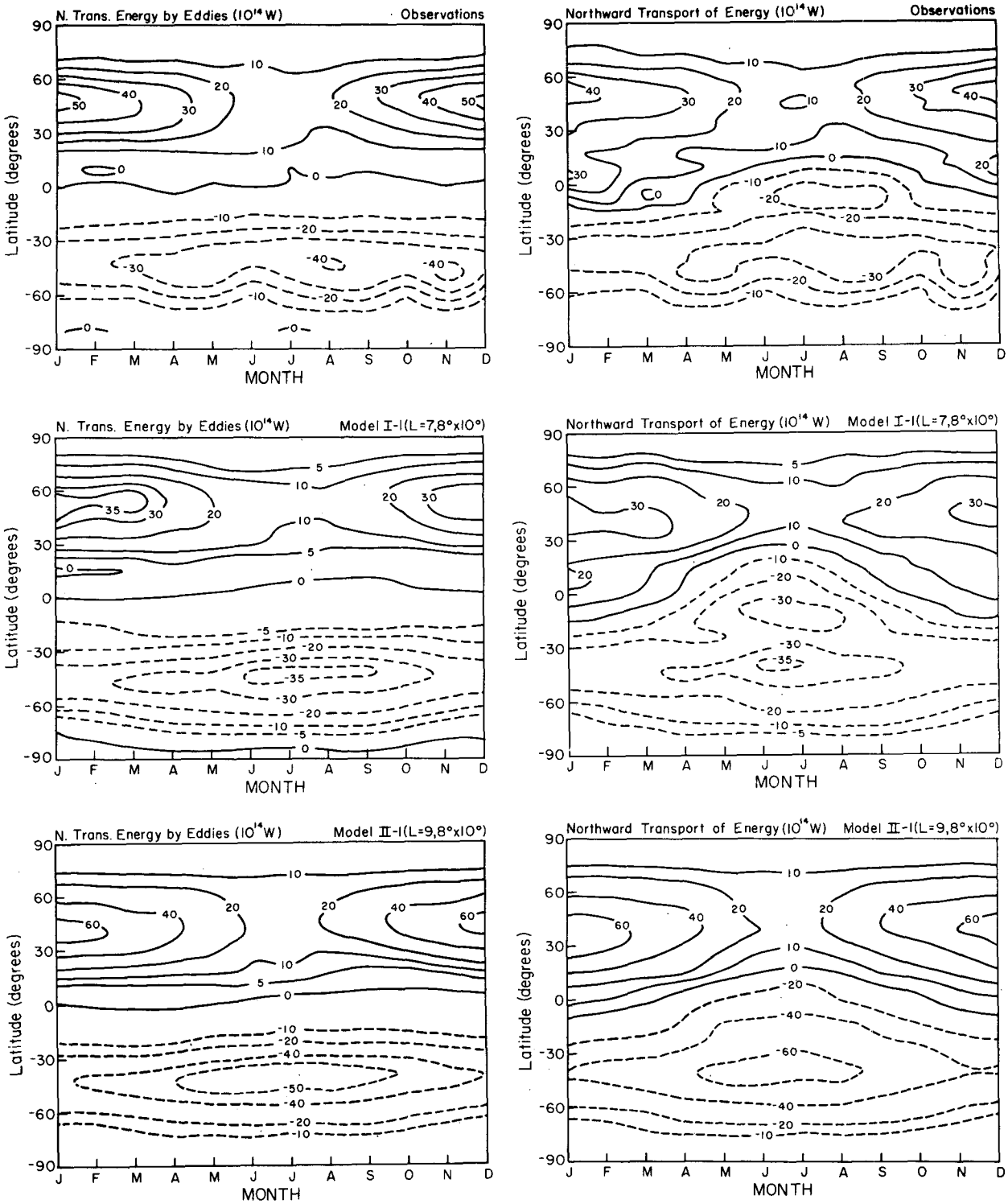

FIG. 38. Northward transport of energy by eddies (left) and by eddies plus mean circulation (right). Observations are from Oort (1982).

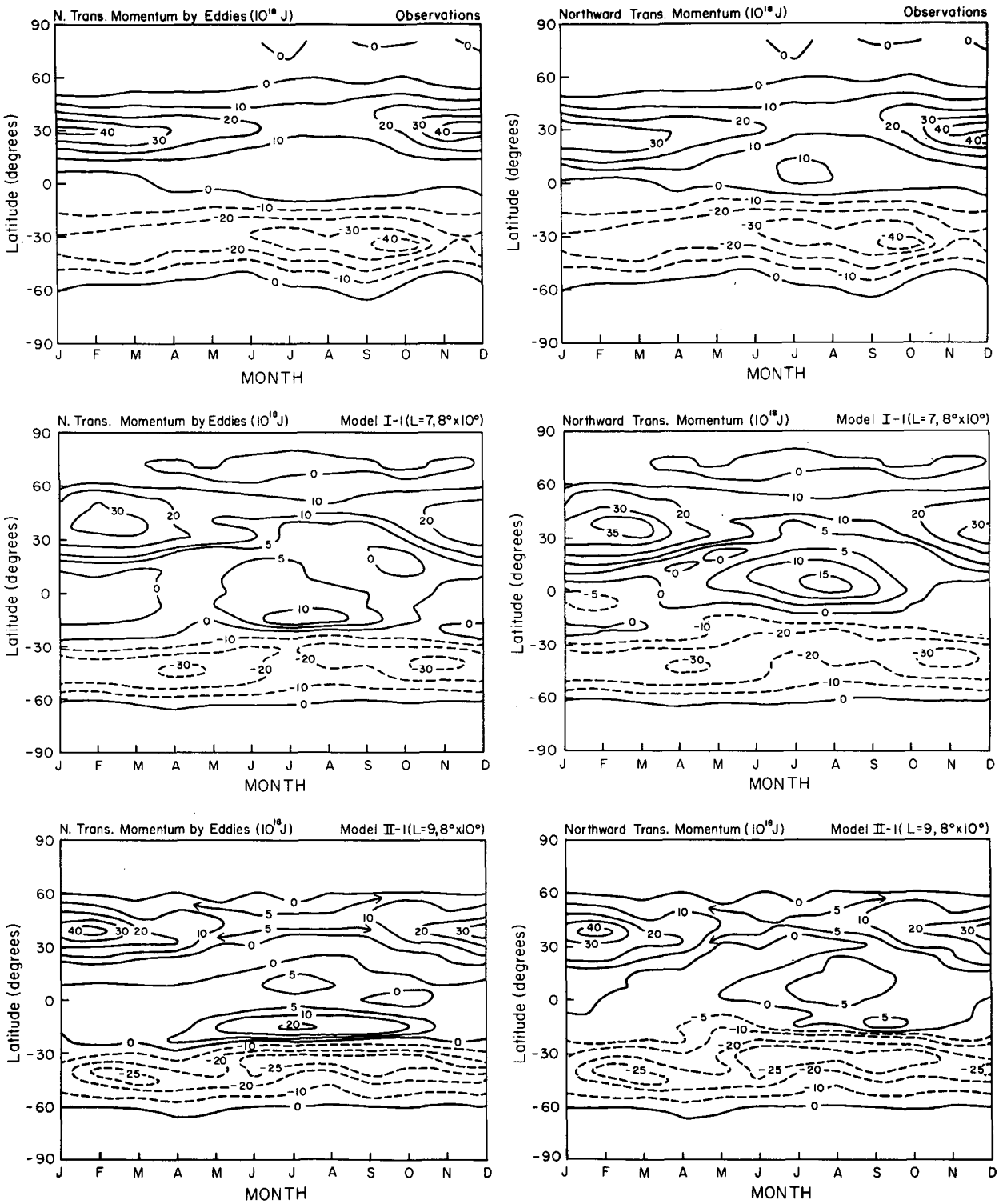

FIG. 39. Northward transport of angular momentum by eddies (left) and eddies plus mean circulation (right). Observations are from Oort (1982).

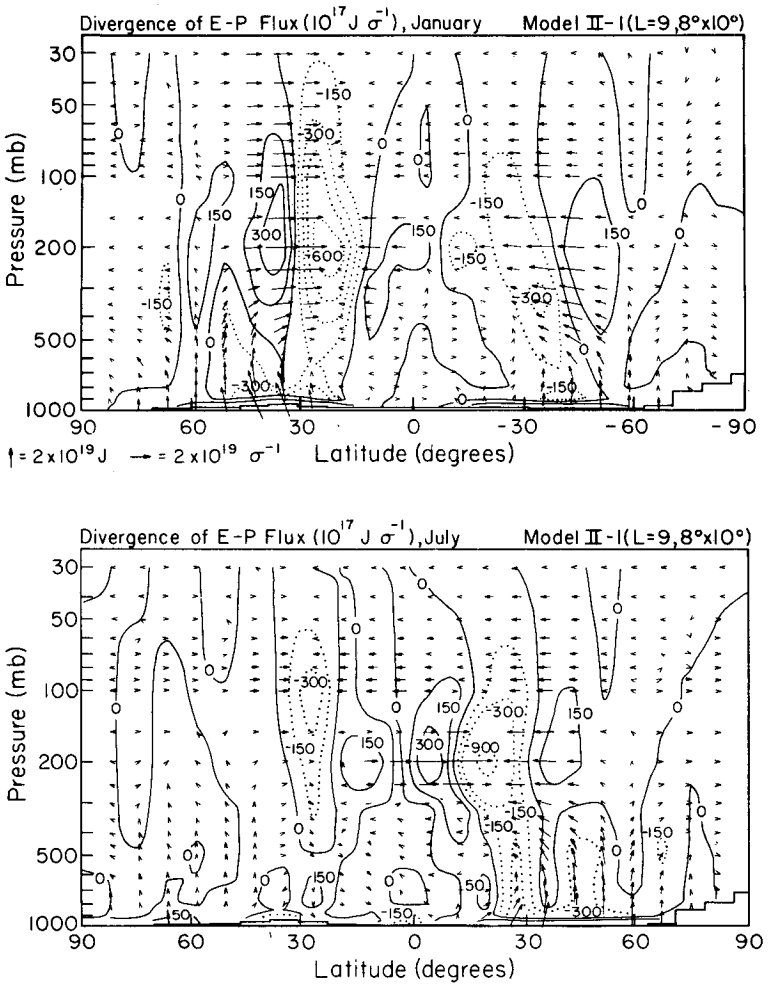

FIG. 40. Eliassen-Palm flux (arrows) and divergence (contours) for January (top) and July (bottom) from Model II-1.

simulated at 12° × 15°, but the results improve markedly for the higher resolutions. Precipitation over the United States is somewhat too large, even with the higher resolutions. The ITCZ becomes increasingly apparent as the resolution increases, and it is perhaps even too sharp at 4° × 5° resolution, consistent with the narrow Hadley cell. These differences appear to be significant, since they exceed the standard deviation of precipitation (Fig. 27).

Sea level pressure patterns (Figs. 42 and 34) show substantial improvements in going from 12° × 15° to 8° × 10° and in going from 8° × 10° to 4° × 5°. There are major changes in the locations and widths of the Icelandic, Aleutian and subAntarctic lows, although, as can be seen in Fig. 35, interannual variability may contribute to these differences. Sea level pressure and precipitation exhibit an unrealistic strong wavenumber 6 behavior at high latitudes for 12° × 15° resolution.

Zonal mean cloud cover (Fig. 43b) is deficient in the ITCZ and greater than observations at high winter latitudes, the latter excess primarily due to the lack of a cloud minimum in the Siberian high pressure region (Fig. 26). The results are qualitatively similar at all three resolutions.

Northward transport of sensible heat, total energy and momentum is shown in Fig. 44. Transports of sensible heat and energy are similar for all resolutions. The excess northward transport of energy by the model at latitudes 20–50°N is primarily in the upper layer, which is not included in the observational analyses. The transports of momentum are much more sensitive to model resolution than the transports of energy. The large increase in eddy momentum flux in going to the fine grid is consistent with having a much stronger and better positioned Ferrel cell.

5. Discussion

We have shown that the major features of global climate can be simulated reasonably well with a horizontal resolution as coarse as 1000 km. Such a resolution allows the possibility of long-range climate

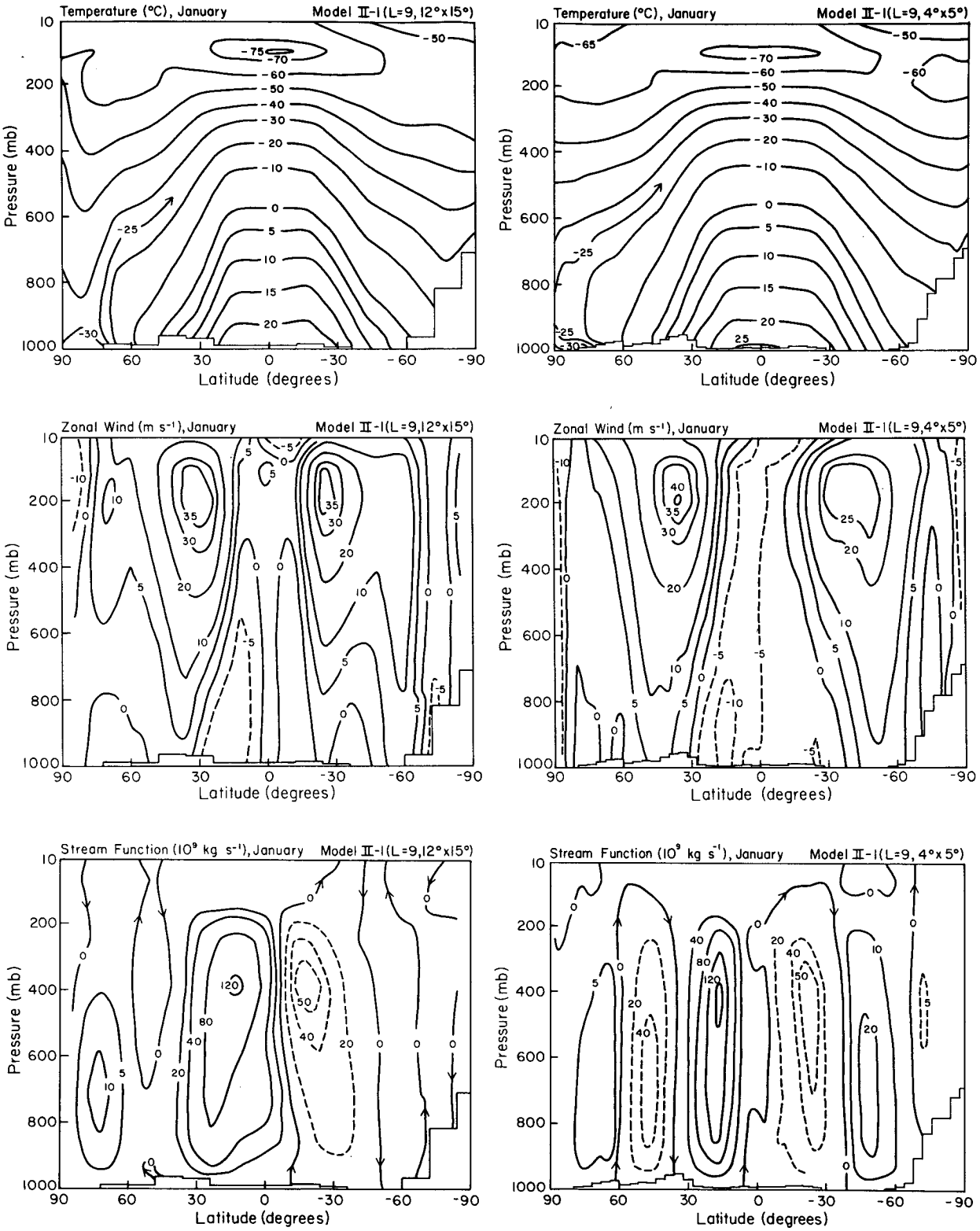

FIG. 41. Zonal-mean temperature, zonal wind and streamfunction for 12° × 15° (left) and 4° × 5° (right) horizontal resolution of Model II. Model results for 8° × 10° resolution and observations are given in Figs. 20, 29 and 31.

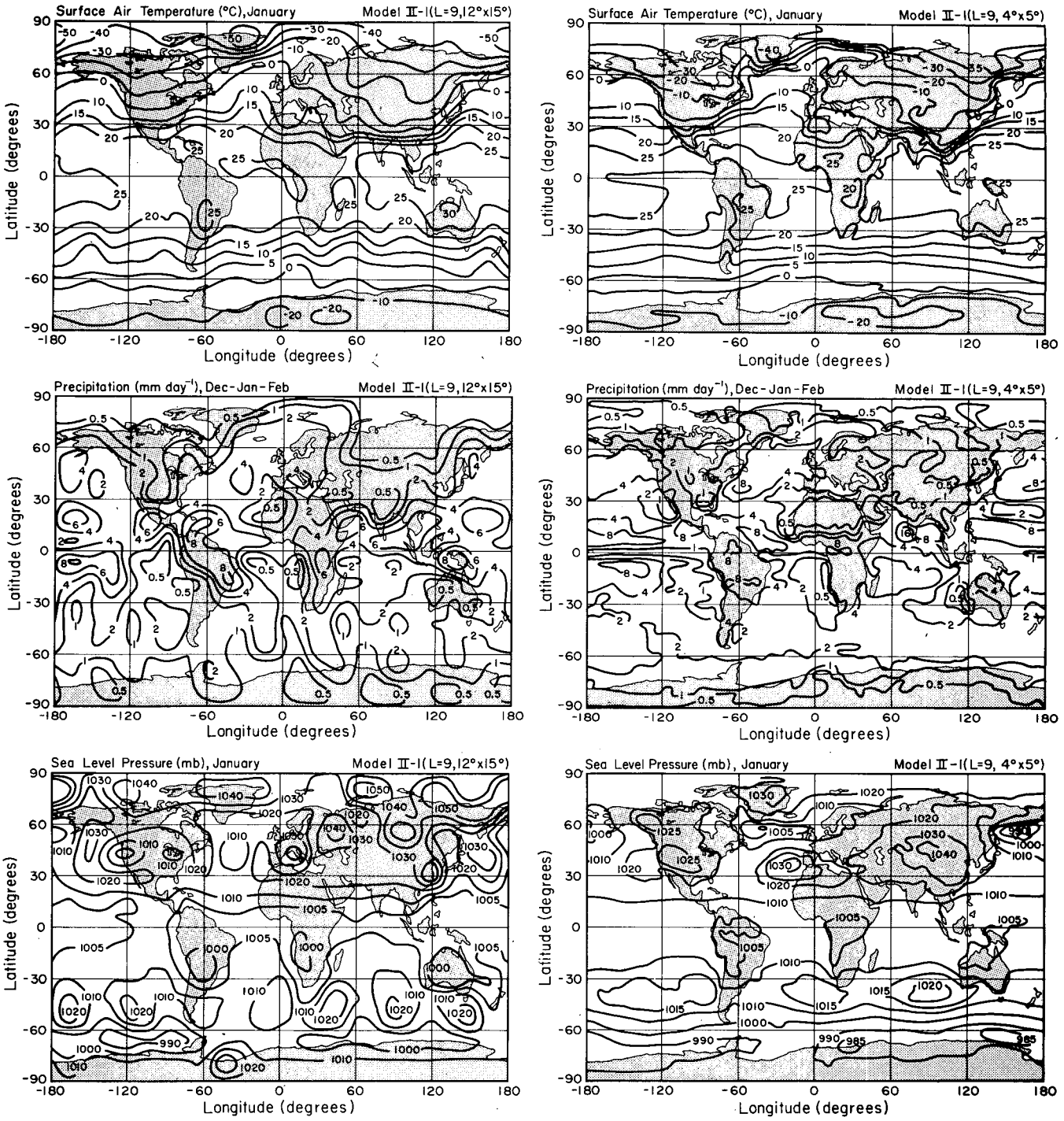

FIG. 42. Global distribution of surface air temperature, precipitation and sea level pressure for 12° × 15° (left) and 4° × 5° (right) horizontal resolution of Model II. Precipitation is for a single December–February period and the other two quantities are for a single January. Model results for 8° × 10° resolution and observations are given in Figs. 21, 28 and 34.

studies, involving model runs of several years or decades, with moderate computer resources.

The sensitivity experiments of the present paper illustrate the need for improvements in modeling of several physical processes. For example, moist convection, clouds, boundary layer transports and ground hydrology each crucially affect the climate simulations, but are presently treated in very crude ways.

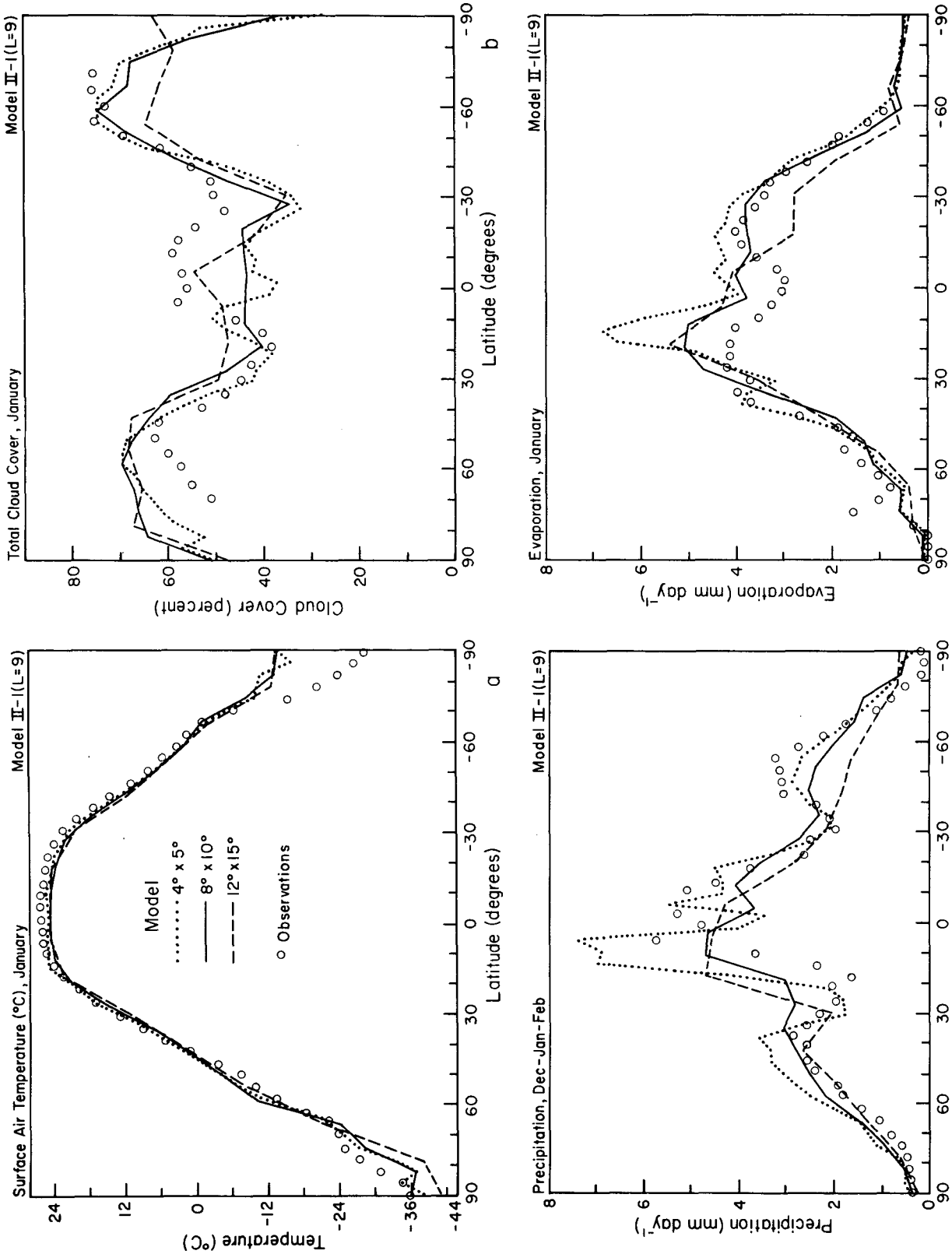

FIG. 43. Zonal mean surface air temperature (a), cloud cover (b), precipitation (c) and evaporation (d) for three horizontal resolutions of Model II. Model results are means from a 5-year run for 8° × 10° resolution, but from a single month or season for the other resolutions. Observations are from (a) Crutcher and Meserve (1970) and Taljaard *et al.* (1969), (b) Berry *et al.* (1973), and (c) and (d) Schutz and Gates (1971).

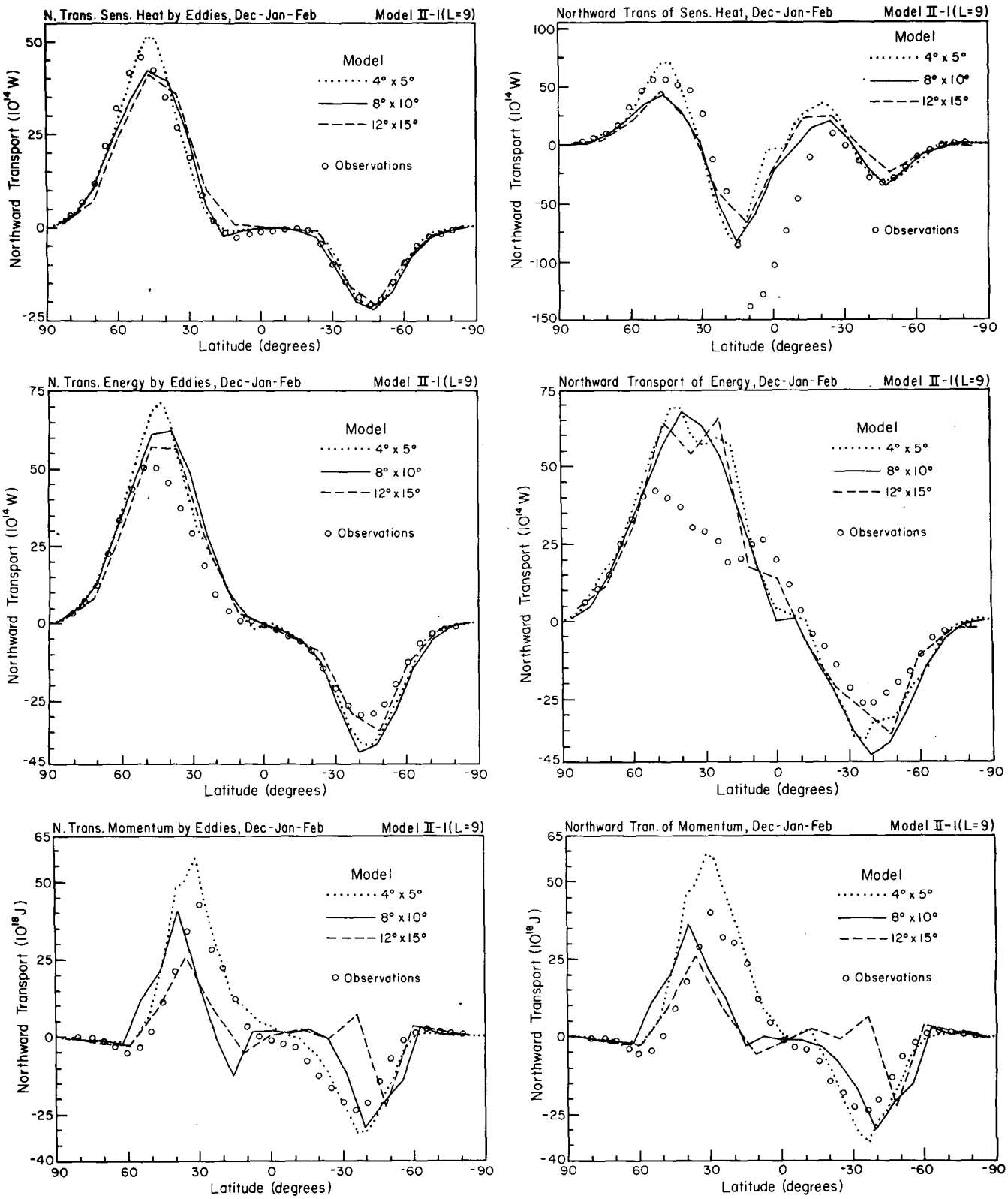

FIG. 44. Zonal mean northward transport of sensible heat, energy and angular momentum by atmosphere. Transport by eddies is on the left and total atmospheric transport (by eddies plus mean circulation) on the right. Model results are means from a 5-year run for 8° × 10° resolution, but from a single season for other resolutions. Observations are from Oort (1982).

Greater realism in modeling these processes may improve climate simulation capability at a relatively small expenditure of computer resources. It is also important to seek improved differencing formulations to minimize numerical errors, before resorting to costly increase in spatial resolution. We plan to use Model II as a base for systematic investigation of key physical processes and numerical techniques, and then attempt to assemble an improved model. In developing Model III we will pay special attention to features which are not well simulated in the 8° × 10° Model II. In particular it is desirable to improve the simulation of sea level pressure patterns, global cloud distribution and the Ferrel cell and its associated transports.

Acknowledgments. We thank Drs. A. Arakawa, E. Kalnay, W. Rossow, K. Trenberth, W. Washington and R. Wetherald for advice, A. Oort for observational data, K. Bhattacharya, J. Lerner, E. Moore and R. Suozzo for producing model and observational diagnostics, and L. DelValle and J. Mendoza for drafting the figures. This work was supported by the NASA Climate Program managed by Dr. R. Schiffer.

REFERENCES

Alexander, R. C., and R. L. Mobley, 1974: Monthly average sea-surface temperatures and ice-pack limits on a 1° global grid. Rep. 4-1310-ARPA, Rand Corp., Santa Monica, 30 pp.

Ambartsumian, V., 1936: The effect of absorption lines on the radiative equilibrium of the outer layers of stars. *Publ. Astron. Obser. Leningrad,* **6,** 7–18.

Andrews, D., and M. E. McIntyre, 1976: Planetary waves in horizontal and vertical shear: The generalized Eliassen-Palm relation and the zonal mean acceleration. *J. Atmos. Sci.,* **33,** 2031–2048.

Arakawa, A., 1972: Design of the UCLA General Circulation Model. Tech. Rep. No. 7, Dept. Meteor., University of California, Los Angeles, 116 pp.

——, and V. R. Lamb, 1977: Computational design of the basic dynamical processes of the UCLA general circulation model. *Meth. Comput. Phys.,* **17,** 173–265.

——, and ——, 1981: A potential enstrophy and energy conserving scheme for the shallow water equations. *Mon. Wea. Rev.,* **109,** 18–36.

Baier, W., D. Z. Chaput, D. A. Russello and W. R. Sharp, 1972: Soil moisture estimator program system. Tech. Bull. No. 78, Canada Dept. Agriculture, Sir John Carling Building, Ottawa, 55 pp.

Baumgartner, A., H. Mayer and W. Metz, 1977: Weltweite Verteilung des Rauhigkeits parameters z_0. *Meteor. Rundsch.,* **30,** 43–48.

Berry, F., E. Bollay and N. Beers, Eds., 1973: *Handbook of Meteorology.* McGraw-Hill, 1068 pp.

Bryden, H. L., 1979: Poleward heat flux and conversion of available potential energy in the Drake Passage. *J. Mar. Res.,* **37,** 1–22.

Businger, J. A., J. C. Wyngaard, Y. Izumi and E. F. Bradley, 1971: Flux-profile relationships in the atmospheric surface layer. *J. Atmos. Sci.,* **28,** 181–189.

Campbell, G., and T. Vonder Haar, 1980: Climatology of radiation budget measurements from satellites. Atmos. Sci. Pap. No. 323, Colorado State University, Ft. Collins, 74 pp.

Chang, J-H., 1958: *Ground Temperature,* Vol. I. Report, Blue Hill Observatory, Harvard University, 300 pp.

Charney, J., 1971: Geostrophic turbulence. *J. Atmos. Sci.,* **28,** 1087–1095.

Clarke, R., and G. Hess, 1975: On the relation between surface wind and pressure gradient, especially in lower latitudes. *Bound.-Layer Meteor.,* **9,** 325–339.

——, A. Dyer, R. Brook, D. Reid and A. Troup, 1971: The Wangara experiment boundary layer data. Tech. Pap. No. 19, CSIRO Div. Meteor. Phys., 340 pp.

Cox, C., and W. Munk, 1956: Slopes of the sea surface deduced from photographs of the sun glitter. *Bull. Scripps Inst. Oceanogr.,* **6,** 401–488.

Crutcher, H., and J. Meserve, 1970: *Selected Level Heights, Temperatures and Dew Points for the Northern Hemisphere.* NAVAIR 50-1C-52, 424 pp. [U.S. Govt. Printing Office].

Deardorff, J. W., 1967: Empirical dependence of the eddy coefficient for heat upon stability above the lowest 50 m. *J. Appl. Meteor.,* **6,** 631–643.

——, 1968: Dependence of air-sea transfer coefficients on bulk stability. *J. Geophys. Res.,* **73,** 2549–2557.

Doronin, Yu. P., 1969: *Thermal Interaction of the Atmosphere and the Hydrosphere in the Arctic.* Israel Program for Scientific Translations, Jerusalem, 1970, 244 pp. [NTIS N71-15668].

Edmon, H., B. Hoskins and M. McIntyre, 1980: Eliassen-Palm cross sections for the troposphere. *J. Atmos. Sci.,* **37,** 2600–2616.

Elsasser, W. M., 1942: *Heat Transfer by Infrared Radiation in the Atmosphere. Harvard Meteor. Stud.,* No. 6, 107 pp.

Eliassen, A., and E. Palm, 1961: On the transfer of energy in stationary mountain waves. *Geophys. Publ.,* **22,** 1–23.

Fiedler, F., and M. A. Panofsky, 1972: The geostrophic drag coefficient and the "effective" roughness length. *Quart. J. Roy. Meteor. Soc.,* **98,** 212–220.

Garratt, J. R., 1977: Review of drag coefficients over oceans and continents. *Mon. Wea. Rev.,* **105,** 915–928.

Gates, W. L., and A. B. Nelson, 1975: A new (revised) tabulation of the Scripps topography on a 1° global grid. Part I: Terrain heights. Rep. R-1276-1-ARPA, Rand Corp., Santa Monica, 132 pp.

Gordon, A., 1952: The relation between the mean vector surface wind and the mean vector pressure gradient over the oceans. *Geofis. Pura Appl.,* **21,** 49–51.

Hall, T. V., and F. E. Blacet, 1952: Separation of the absorption spectra of NO_2 and N_2O_4 in the range of 2400–5000. *J. Chem. Phys.,* **20,** 1745–1749.

Haltiner, G., and F. Martin, 1957: *Dynamical and Physical Meteorology.* McGraw-Hill, 470 pp.

Hansen, J. E., 1969: Absorption-line formation in a scattering planetary atmosphere. *Astrophys. J.,* **158,** 337–349.

——, and J. B. Pollack, 1970: Near-infrared light scattering by terrestrial clouds. *J. Atmos. Sci.,* **27,** 265–281.

——, and L. Travis, 1974: Light scattering in planetary atmospheres. *Space Sci. Rev.,* **16,** 527–610.

Harries, J., D. Moss, N. Swann, G. Neill and P. Gildwarg, 1976: Simultaneous measurements of H_2O, NO_2 and HNO_3 in the daytime stratosphere from 15 to 35 km. *Nature,* **259,** 300–302.

Hastenrath, S., 1980: Heat budget of tropical ocean and atmosphere. *J. Phys. Oceanogr.,* **10,** 159–170.

Haurwitz, B., 1948: Insolation in relation to cloud type. *J. Meteor.,* **5,** 110–113.

Held, I., and A. Hou, 1980: Nonlinear axially symmetric circulations in a nearly inviscid atmosphere. *J. Atmos. Sci.,* **37,** 515–533.

Hillel, D., 1971: *Soil and Water.* Academic Press, 288 pp.

Holton, J., 1979: *An Introduction to Dynamic Meteorology,* 2nd ed. Academic Press, 391 pp.

——, and W. Wehrbein, 1980: A numerical model of the zonal mean circulation of the middle atmosphere. *Pure Appl. Geophys.,* **118,** 284–306.

Hovis, W. A., and W. R. Callahan, 1966: Infrared reflectance spec-

tra of igneous rocks, tuffs, and red sandstone from 0.5 to 22 μm. *J. Opt. Soc. Amer.*, **56,** 639–643.

JOC, 1975: The physical basis of climate and climate modeling. *GARP Publ. Ser.*, No. 16, WMO, Geneva, 265 pp.

Kálnay de Rivas, E., 1972: On the use of nonuniform grids in finite-difference equations. *J. Comput. Phys.*, **10,** 202–210.

Kasahara, A., and W. M. Washinton, 1967: NCAR global circulation model of the atmosphere. *Mon. Wea. Rev.*, **95,** 389–402.

Lacis, A. A., and J. E. Hansen, 1974: A parameterization for the absorption of solar radiation in the earth's atmosphere. *J. Atmos. Sci.*, **31,** 118–133.

L'vovich, M., 1980: *World Water Resources and Their Future.* English translation, U.S. Dept. of Commerce, Washington, DC, 414 pp.

McClatchey, R. A., W. S. Benedict, S. A. Clough, D. E. Burch, R. F. Calfee, K. Fox, L. S. Rothman and J. S. Garing, 1973: AFCRL atmospheric absorption line parameters compilation. Env. Res. Pap. No. 434, Hanscom AFB, Bedford, MA, 78 pp.

Malkmus, W., 1967: Random Lorentz band model with exponential-tailed S^{-1} line intensity distribution function. *J. Opt. Soc. Amer.*, **57,** 323–329.

Manabe, S., J. Smagorinsky and R. F. Strickler, 1965: Simulated climatology of a general circulation model with a hydrologic cycle. *Mon. Wea. Rev.*, **93,** 769–798.

——, ——, J. L. Holloway and H. M. Stone, 1970: Simulated climatology of a general circulation model with a hydrologic cycle, III. Effects of increased horizontal computational resolution. *Mon. Wea. Rev.*, **98,** 175–212.

——, K. Bryan and M. J. Spelman, 1975: A global ocean-atmosphere climate model. Part I. The atmospheric circulation. *J. Phys. Oceanogr.*, **5,** 3–29.

Matsuno, T., 1966: Numerical integrations of the primitive equation by a simulated backward difference method. *J. Meteor. Soc. Japan,* Ser. 2, **44,** 76–84.

Matthews, E., 1983: Global vegetation and land use: New high resolution data bases for climate studies. *J. Climate Appl. Meteor.* (submitted).

Merilees, P. E., 1975: The effect of grid resolution on the instability of a simple baroclinic model. *Mon. Wea. Rev.*, **103,** 101–104.

Miller, D., 1977: *Water at the Surface of the Earth.* Academic Press, 557 pp.

Oort, A. H., 1964: On estimates of the atmospheric energy cycle. *Mon. Wea. Rev.*, **92,** 483–493.

——, 1982: *Global Atmospheric Circulation Statistics, 1958–1973.* NOAA Prof. Pap. No. 14 (in press).

——, and T. H. Vonder Haar, 1976: On the observed annual cycle in the ocean-atmosphere heat balance over the Northern Hemisphere. *J. Phys. Oceanogr.*, **6,** 781–800.

Orvig, S., 1970: *Climates of the Polar Regions.* Elsevier, 370 pp.

Phillips, N. A., 1957: A coordinate surface having some special advantage for numerical forecasting. *J. Meteor.*, **14,** 184–185.

Platt, C. M. R., 1975: Infrared emissivity of cirrus-simultaneous satellite, lidar and radiometric observations. *Quart. J. Roy. Meteor. Soc.*, **101,** 119–126.

Posey, J. W., and P. F. Clapp, 1964: Global distribution of normal surface albedo. *Geofis. Int.*, **4,** 33–48.

Roberts, R. E., J. E. A. Selby and L. M. Biberman, 1976: Infrared continuum absorption by atmospheric water vapor in the 8–12 μm window. *Appl. Opt.*, **15,** 2085–2090.

Robinson, G., 1958: Some observations from aircraft of surface albedo and the albedo and absorption of cloud. *Arch. Meteor. Geophys. Bioklim.*, **B9,** 28–41.

Robinson, M., and R. Bauer, 1981: *Oceanographic Monthly Summary,* **1,** No. 2, NOAA National Weather Service, W322, Washington, DC, pp. 2–3.

Rothman, L. S., 1981: AFGL atmospheric absorption line parameters compilation: 1980 version. *Appl. Opt.*, **20,** 791–794.

Saltzman, B., 1970: Large-scale atmospheric energetics in the wavenumber domain. *Rev. Geophys. Space Phys.*, **8,** 289–302.

Schutz, C., and W. Gates, 1971: Global climatic data for surface, 800 mb, 400 mb. Reps. R-915-ARPA, R-915/1-ARPA, R-1029-ARPA, Rand Corp., Santa Monica.

Sellers, W. D., 1965: *Physical Climatology,* University of Chicago Press, 272 pp.

Shapiro, R., 1970: Smoothing, filtering and boundary effects. *Rev. Geophys. Space Phys.*, **8,** 359–387.

Shukla, J., and Y. Sud, 1981: Effect of cloud-radiation feedback on the climate of a general circulation model. *J. Atmos. Sci.*, **38,** 2237–2253.

Somerville, R. C. J., P. H. Stone, M. Halem, J. E. Hansen, J. S. Hogan, L. M. Druyan, G. Russell, A. A. Lacis, W. J. Quirk and J. Tenenbaum, 1974: The GISS model of the global atmosphere. *J. Atmos. Sci.*, **31,** 84–117.

Squires, P., 1958: The microstructure and colloidal stability of warm clouds. Part I: The relation between structure and stability. *Tellus,* **10,** 256–261.

Starr, V. P., J. P. Peixoto and N. E. Gaut, 1970: Momentum and zonal kinetic energy balance of the atmosphere from five years of hemispheric data. *Tellus,* **22,** 251–274.

Stephens, G. L., and P. Webster, 1977: Sensitivity of radiance forcing to variable cloud and moisture. *J. Atmos. Sci.*, **36,** 1542–1556.

——, G. G. Campbell and T. H. Vonder Haar, 1981: Earth radiation budgets. *J. Geophys. Res.*, **86,** 9739–9760.

Stone, P., and H. Carlson, 1979: Atmospheric lapse rate regimes and their parameterization. *J. Atmos. Sci.*, **36,** 415–423.

Strahler, A. N., 1969: *Physical Geography,* 3rd ed. Wiley, 733 pp.

Swanson, G., and K. Trenberth, 1981: Trends in the Southern Hemisphere tropospheric circulation. *Mon. Wea. Rev.*, **109,** 1879–1889.

Taljaard, J., H. van Loon, H. Crutcher and R. Jenne, 1969: *Climate of the Upper Air,* Vol. 1. NAVAIR 50-1C-55 [U.S. Govt. Printing Office].

Taylor, G., 1916: Skin friction of the wind on the earth's surface. *Proc. Roy. Soc. London,* **A92,** 196–199.

Taylor, K., 1976: The influence of subsurface energy storage on seasonal temperature variations. *J. Appl. Meteor.*, **15,** 1129–1138.

Toon, O. B., and J. B. Pollack, 1976: A global average model of atmospheric aerosols for radiative transfer calculations. *J. Appl. Meteor.*, **15,** 225–246.

Trenberth, K. E., 1979: Mean annual poleward energy transports by the oceans in the Southern Hemisphere. *Dyn. Atmos. Oceans,* **4,** 57–64.

U.S. Army Corps of Engineers, 1956: Snow hydrology. Report of Snow Investigations, North Pacific Division, Portland, OR, 437 pp.

Wallace, J., and D. Gutzler, 1981: Teleconnections in the geopotential height field during the Northern Hemisphere winter. *Mon. Wea. Rev.*, **109,** 784–812.

——, and P. Hobbs, 1977: *Atmospheric Science.* Academic Press, 467 pp.

Walsh, J., and C. Johnson, 1979: An analysis of Arctic sea ice fluctuations. *J. Phys. Oceanogr.*, **9,** 580–591.

Wang, W. C., Y. L. Yung, A. A. Lacis, T. Mo and J. E. Hansen, 1976: Greenhouse effects due to man-made perturbations of trace gases. *Science,* **194,** 685–690.

Washington, W. M., and D. L. Williamson, 1977: A description of the NCAR global circulation models. *Meth. Comput. Phys.*, **17,** 111–172.

Wellck, R. E., A. Kasahara, W. M. Washington and G. Santo, 1971: Effect of horizontal resolution in a finite-difference model of the general circulation. *Mon. Wea. Rev.*, **99,** 673–683.

Willson, R. C., 1978: Accurate solar "constant" determination by cavity pyrheliometers. *J. Geophys. Res.*, **83,** 4003–4007.

Wiscombe, W. J., and S. G. Warren, 1980: A model for the spectral albedo of snow. I: Pure snow. *J. Atmos. Sci.*, **37,** 2712–2733.